AN ABSTRACT OF THE THESIS OF

ANTHONY MICHAEL SUTEY for the Doctor of Philosophy
(Name of student) (Degree)

in Chemical Engineering presented on March 8, 1967
(Major) (Date)

Title: MASS TRANSFER AT THE SOLID-LIQUID INTERFACE FOR CLIMBING FILM FLOW IN AN ANNULAR DUCT

Abstract approved: Redacted for Privacy
Dr. James G. Knudsen

A method utilizing a diffusion controlled electrochemical reaction was used to measure average and instantaneous mass transfer coefficients at the solid-liquid film interface in upward gas-liquid climbing film flow in a vertical annular duct. Experimental average mass transfer coefficients are estimated to be accurate within ± 5%. These measurements give some indication of the mechanics of flow of the film, the extent of turbulence at the inner wall, and the effect of film thickness and wave motion on the mass transfer process at the inner wall. Predictions of incipient downflow of the film, shear stress at the inner wall, and interfacial shear stress were obtained from these measurements. Fluctuations in the velocity gradient at the inner wall were also studied. Results of this study were compared with previous work and with theoretical predictions based on laminar film concepts.

The results of this study are as follows:

(1) At constant liquid flow rate the mass transfer coefficient decreases rapidly as air flow rate decreases and at very low gas flow rates exhibits a minimum value which corresponds to incipient downflow within the climbing film.

(2) At constant gas flow rate the mass transfer coefficient decreases slightly as liquid flow rate is decreased and at very low liquid flow rates increases sharply just prior to the minimum wetting rate.

(3) Based on the fluctuations in the rate of mass transfer to the inner core wall, the climbing film flow is considered turbulent for the gas and liquid flows studied. The climbing film is relatively stable at high gas flow rates but becomes increasingly turbulent as downflow is approached.

(4) The shear stress at the inner wall was calculated from the Leveque Theory for climbing film flow using experimental mass transfer data of a short electrode. Results compare well with independent values calculated from previous work.

(5) At constant liquid flow rate the pressure gradient decreases rapidly as the air flow rate decreases and at very low air flow rates reaches a minimum value which closely corresponds in terms of air and liquid flow rates to incipient downflow as indicated by the mass transfer coefficient data.

(6) Interfacial shear stresses were calculated from two separate relationships each using independent experimental data and the results compare well with each other.

(7) The laminar-film model predicts shear stresses at the inner wall and flow conditions at downflow which compare well with values obtained using mass transfer coefficient data.

(8) At very low gas rates the shear stress ratio τ_i/τ_l approaches infinity as downflow is approached. At high gas rates this ratio becomes independent of liquid flow rate and approaches unity. The similar behavior of τ_i/τ_l and film thickness as affected by flow conditions demonstrates the dependence of the velocity profile on film thickness.

Mass Transfer at the Solid-Liquid Interface for Climbing Film Flow in an Annular Duct

by

Anthony Michael Sutey

A THESIS

submitted to

Oregon State University

in partial fulfillment of
the requirements for the
degree of

Doctor of Philosophy

June 1967

TO MY LOVING

WIFE AND CHILDREN

APPROVED:

Redacted for Privacy

Professor of Chemical Engineering
in charge of major

Redacted for Privacy

Head of Department of Chemical Engineering

Redacted for Privacy

Dean of Graduate School

Date thesis is presented March 8, 1967

Typed by Donna Olson for Anthony Michael Sutey

ACKNOWLEDGEMENTS

I wish to extend my grateful appreciation to the following:

To Dr. James G. Knudsen, Assistant Dean of Engineering, for his professional assistance and kind support during the past four years.

To the National Science Foundation for its fincancial support of this study.

To Professor Jesse S. Walton, Head of the Department of Chemical Engineering.

To the members of my doctoral committee, Robert V. Mrazek, Giles W. Maloof, and Allen B. Scott.

To William B. Johnson and Robert C. Mang for their aid in construction of the experimental equipment.

To my colleague, Duk H. Kim for his thoughtful suggestions and aid in construction of the two-phase system.

To my parents for their continuous encouragement and support.

TABLE OF CONTENTS

LIST OF FIGURES

LIST OF TABLES

MASS TRANSFER AT THE SOLID-LIQUID INTERFACE FOR CLIMBING FILM FLOW IN AN ANNULAR DUCT

INTRODUCTION

Climbing film flow is but one of the various regimes of upward two-phase (gas-liquid) flow. In climbing film flow the liquid moves upward as a film on the surface of the duct as the faster moving gas stream flows upward adjacent to the liquid film. Due to the momentum transfer at the gas-liquid interface, the liquid film is transported upward at the expense of the pressure energy of the gas stream. As a result, the liquid film is characterized by complex wave and entrainment phenomena. This type of flow is of particular interest since it exists over a rather wide range of gas and liquid flow rates and is commonly encountered in petroleum refining processes, steam generators, evaporators, and in coolant channels of nuclear reactors. A knowledge of the mechanics of flow of the film is therefore essential to predict and understand the momentum, heat, and mass transfer processes which occur in climbing film flow.

Climbing film flow has been studied in a variety of channels including circular tubes, rectangular ducts and annuli. In the present study the liquid flows as a film up the concentric inner core of an annulus while air flows upward in the annular space, the outer wall of the annulus remaining dry. Such an arrangement permits direct

observation of the climbing film through a transparent outer tube and simplifies the measurement of pressure gradients, air velocity profiles, and film structure.

This study was concerned with the mass transfer phenomena which occur at the solid-liquid interface. An electrochemical method utilizing a ferro-ferricyanide redox couple was used to measure average and instantaneous mass transfer coefficients. Since this method had previously been restricted to oxygen free systems, a preliminary study was performed in a pipe flow system to measure the actual effect of dissolved oxygen on the measured mass transfer coefficient. It was found that the electrochemical technique can be applied in the presence of air if certain precautions are taken.

Average and instantaneous mass transfer coefficients were obtained at the solid-liquid interface. These measurements were desired to give some indication of the mechanics of flow of the film, the extent of turbulence at the inner wall, and the effect of film thickness and wave motion on the mass transfer process at the inner wall. Predictions of incipient downflow of the film, shear stress at the inner wall, and interfacial shear stress were obtained from these measurements.

Since this study is part of an overall investigation of climbing film flow in an annular duct, it not only presents new information but also utilizes and extends the previous work of Kim (45). Results of

this study were compared with the data of Kim and with theoretical predictions based on laminar film concepts. This study demonstrates the advantage of local instantaneous measurements in describing climbing film phenomena. Further studies of this type will lead to a more basic understanding of the processes of heat, mass, and momentum transfer which occur in two-phase gas-liquid film flow.

PREVIOUS WORK AND THEORY

Characterization of Upward Two-Phase Gas-Liquid Flow Regimes

In the past, two-phase flow regimes have been classified in a subjective visual manner. The various flow patterns can be observed sequentially as the gas flow rate increases at constant liquid flow rate (7). Similar regimes are observed in ascending sequence of generated steam content under constant heat flux in heated channels (11). The regimes are commonly defined as bubble, slug, semi-annular, annular (climbing film), and mist. Recently, Dukler and Hubbard (17) described these regimes in a quantitative nonvisual manner. Their method of flow regime detection and characterization requires only a single measurement at the channel wall with a pressure transducer which does not disturb the flow field. They found that the power spectrum density distribution of wall pressure fluctuations uniquely characterized the wide range of previously reported flow regimes into only three groups: dispersed flows, intermittent flows, and separated flows. Climbing film flow is included in the latter.

General Description of Climbing Film Flow in Annuli

Climbing film flow is but one of the various regimes of upward

two-phase gas-liquid flow. In this study the liquid flows as a film up the concentric inner core of an annulus while air flows upward in the annular space, the outer wall of the annulus remaining dry. This design, Figure 5, permits direct observation of the climbing film through a transparent outer tube. Such an arrangement simplifies the measurement of pressure gradients, air velocity profiles, and film structure.

The climbing film phenomena can be observed as the gas flow rate is varied at constant liquid flow rate. At high gas flows, the liquid moves rapidly up the inner core of the annulus as a very thin climbing film. As the gas flow rate decreases, the film velocity decreases and the film thickness increases. At very low gas flow rates downflow occurs where the liquid near the inner wall may flow downward even though the net film flow may be upward. The point of incipient downflow, which corresponds to zero shear stress at the solid-liquid film interface, has been predicted by Kim (45), Willis (72), and Hewitt, Lacey, and Nicholls (39).

At very low gas rates one can visually observe the downflow phenomenon when the climbing film is first formed. The liquid climbs upward a short distance along the inner rod then falls downward slightly only to recover and flow upward again. In this pulse-like manner the liquid eventually climbs the inner core of the annulus. The upward motion of the film is generated within high amplitude

waves at the air-liquid interface while liquid near the inner wall flows downward. At slightly lower gas rates insufficient momentum is transferred from the gas stream to sustain the film and flooding occurs.

For the case of very low liquid flow rates (less than 0.2 lb/min) a stable liquid film does not form completely around the entire circumference of the inner core of the annulus. At such low liquid rates dry patches occur causing the liquid to flow in several narrow rivulets dispersed around the circumference of the inner core. The liquid flow rate at which the permanent patches first appear is referred to as the "minimum wetting rate". The breakdown of the liquid film has been previously studied by Hewitt and Lacey (38) and Norman and McIntyre (57).

At high liquid flow rates (greater than 1.5 lb/min), liquid also flows as a film on the outer wall of the annulus due to an accumulation of entrained liquid from the film on the inner core. In this study flow rates were chosen so that the climbing film flowed only on the inner core of the annulus.

Wave Motion, Entrainment, and Film Instabilities in Climbing Film Flow

The climbing film is characterized by complex wave and entrainment phenomena. At high liquid flow rates (greater than

1.0 lb/min) the film is characterized by small amplitude waves which are periodically overtaken by large amplitude "disturbance" (or roll) waves which form a complete ring around the inner core of the annulus. As reported by other investigators (29, 67) the disturbance waves travel rapidly along the surface of the liquid film and have a "milky" appearance as a result of light scattering by their extremely ruffled surface. These waves are considered responsible at high gas flow rates for initiation of entrainment into the gas core. As the liquid flow rate decreases the disturbance waves become less frequent and "ripple" waves (29, 67) become dominant. These are relatively slow moving, small amplitude waves which are relatively stable. Entrainment decreases and reaches a minimum value in the presence of this type of wave motion. At very low gas flow rates, downflow occurs, and the film is characterized by very slow moving, high amplitude waves. Under this condition the film is highly unstable, and much splashing and entrainment occurs at the gas-liquid interface. At slightly lower gas rates, flooding occurs.

Failure to successfully describe momentum, heat, and mass transfer in climbing films has been attributed in part to a lack of understanding of the wave motion, entrainment and film instabilities previously described. Chand and Rosson (8) demonstrated the importance of wave motion on the heat transfer process within the film. Local instantaneous heat fluxes to a downward flowing water film

were studied for various flow rates and were found to oscillate with the same frequency as the ripples on the surface of the film. A qualitative explanation was presented to describe the heat transfer mechanism within the film. These results indicate the effects of wave motion and turbulence on the film and demonstrate the advantage of local instantaneous measurements in describing the film phenomena.

An attempt to explain the effects of wave motion on heat and mass transfer at the gas-liquid film interface was made by Ruckenstein and Berbente (64). Rates of mass transfer were predicted using the film velocity distribution suggested by Kapitza (44). Although Kapitza's velocity distribution satisfactorily explains phenomena of a hydrodynamical nature, it must be refined to predict satisfactory mass transfer results.

Although considerable work has been performed to explain entrainment (2, 12, 24, 33, 53), wave structure (29, 34, 35, 37, 40, 41, 45), and film instabilities (58, 71), a suitable theoretical explanation of these phenomena is lacking in climbing film flow.

Previous Studies

Vertically upward climbing film flow has been studied in a variety of channels including circular tubes, rectangular ducts and annuli. However, flow in circular tubes has received the most

attention with considerable work being done by Hewitt and co-workers for the United Kingdom Atomic Energy Authority. The work of Quandt (61) is representative of the studies in rectangular ducts. Except for a few studies by Kim (45) and Hewitt and co-workers (36), investigation of climbing film flow in annuli is limited. Nevertheless, the climbing film phenomena are similar regardless of duct geometry.

Recent experimental and theoretical studies of climbing film flow have been concerned with film thickness, pressure losses, entrainment, and shear stresses. There has been reasonably good success in obtaining agreement between theory and experiment as far as average film thickness and pressure losses are concerned; however, most theoretical models require an assumption of the velocity profile in the liquid film. More basic studies are required to determine momentum, heat, and mass transfer at the various interfaces in the system. The effects of wave motion, entrainment, and film instabilities on the climbing film phenomena must be further studied.

Simplified Models for Climbing Film Flow

Various procedures have been developed to analyze the fluid dynamics of two-phase climbing film flow. Earlier studies made little or no attempt to analyze the individual phases. A common

approach has been to correlate pressure drop in terms of the flow rates of the two phases and the channel dimensions alone. The correlation of Govier and co-workers (26, 27) as used by Bennett and Thornton (5) is such an example. Further analyses in this class are the Lockhart and Martinelli (55), Chenoweth and Martin (10), and Dukler, Wicks, and Cleveland (18, 19) correlations. Although the physical and theoretical basis for these relations is often quite vague, they attempt to predict pressure loss and holdup under new conditions by analysis of similarity on existing data. These correlations are limited since they generally show no discontinuities at regime boundaries (67).

The oldest and most widely used correlation is that of Lockhart and Martinelli and has been tested with a fair degree of success (12, 18, 23, 24, 37, 43, 45). It relates the pressure gradient for two phase flow to that of the gas and liquid flowing separately at the same mass flow rate. A unique relationship is postulated between the dimensionless parameters X and Φ, where X is a function of the pressure gradient for the separate phases and Φ relates the pressure gradient for the single phases to that for the two phase flow.

Recently, attempts have been made to analyze two-phase flows in light of the fluid dynamics of the individual phases, in particular, that of the liquid film. The most common approach has been to

divide the liquid film into various flow regimes each having the proper generated or assumed velocity profile. The velocity profiles of the various flow regions are integrated over their particular domains and subsequently added to give the total liquid film flow rate which is then compared with the experimental value. Although two phase flow data can be correlated in this manner, one doubts whether it can explain the fluid dynamics of liquid film flows. The process of integration of various velocity regions and subsequent addition of flow terms tends to mask the contributions of the individual regions. Since the liquid film is generally very thin, application of almost any combination of velocity profiles may give fairly reasonable results. Accurate film thickness data are difficult to obtain and generally one is forced to use average values. Finally, it is difficult to compensate for entrainment effects which hinder accurate local liquid film flow rate measurements.

This method has nevertheless been used with varying degrees of success by Dukler and Bergelin (16), Dukler (15), and Lee (51) in vertical downward film flow and by Calvert and Williams (7), Anderson and Mantzouranis (1), Hewitt (32), and Levy (53) in vertical upward annular flow in tubes. All of these theoretical treatments apply the classical von Karmen-Prandtl turbulent velocity profile as developed for single-phase pipe flow to the liquid film.

In their model Anderson and Mantzouranis assumed a velocity profile with complete disregard of the shear stress distribution within the film. Calvert and Williams generated a velocity profile in the film from the shear stress distribution, however, inconsistencies in

their analysis have been shown to exist by Shearer and Nedderman (67). Data of Collier and Hewitt (12) showed that at very low values of shear at the solid-liquid film interface the Anderson theory predicted film flow rates as much as 1/3 lower than the actual values, whereas, the Calvert theory predicted rates quite close to the measured rates. For high values of wall shear both theories predicted much higher (in the worst case by 400%) film flow rates than those observed. Hewitt and Collier corrected both theories for shear stress variation in the film. The corrected Anderson analysis predicted the film flow rate better than the corrected Calvert analysis although neither was completely satisfactory over the entire flow range studied.

Hewitt (32) applied the Dukler (15) theory to vertical upward flow in a tube. In this analysis, the flowing film was divided into two regions, and the Deissler and the von Karmen eddy viscosity equations were applied to the proper regions in the film to generate a velocity profile from the shear stress distribution within the film. The shear stress distribution within the film was obtained by a force balance on the two-phase system. The resultant theory has correlated the data of Hewitt and co-workers (23, 37) reasonably well ($\pm 30\%$) for high to moderate film thicknesses; however, deviations increase up to $\pm 70\%$ for low film thicknesses--probably as a result of entrainment.

To account for liquid entrainment in annular two-phase flow, Levy (53) considered the momentum and mass transfer components of the interfacial shear stress. The momentum term was shown to be dominant in the liquid film, while the mass transfer term was most important within the gas core. An expression was derived for the interfacial shear in terms of liquid film thickness which was used to successfully correlate available CISE data, and to predict liquid film thickness, liquid film flow rate, and liquid entrainment in the gas core. The model was also applied to reported experimental data of annular flow in the upwards, downwards and horizontal directions. This model which is valid only in the turbulent liquid core ($y^+ > 30$) compares satisfactorily with most of the available experimental data in annular film flow.

Analytical expressions for climbing film flow based on laminar-film concepts have also been developed. In these analyses the steady state equation of motion is solved for the case of laminar film flow. Among the proposed models are those of Laird (49), Willis (72), Shearer and Nedderman (67), and Kim (45).

Assuming laminar flow in the two phases, Laird derived a relation between pressure gradient, liquid hold-up, flow rate and tube dimensions. However, its usefulness is limited since neither the pressure gradient nor the liquid holdup can be predicted from a knowledge of the flow rate and tube dimensions alone.

With his proposed model Willis accurately predicted the experimental points at which downflow of the film occurred. For the small ripple regime and no entrainment, Shearer predicted film thicknesses which are in good agreement with experimental data of Gill and Hewitt (23), and also reported to a 1% accuracy that the interfacial shear stress is equal to the shear stress at the solid-liquid film interface. These analyses describe the liquid film motion with a reasonable degree of accuracy. As expected, experimental data generally show better agreement with these theories in regions of low interfacial shear stress where the liquid flow is more nearly laminar. These models should not suggest that a velocity profile assumed simply from the shear stress distribution is the complete solution for the film motion which is characterized by a complex system of waves and entrainment, but, they do emphasize the importance of using the correct concepts of flow in deriving theoretical equations for film flow.

In an attempt to consider the wave motion in the film, Kim (45) extended the Kapitza (44) theory of wave formation to the climbing film and predicted film flow rates which were about one half of those measured. Predictions of wave lengths of surface waves were 1/4 to 1/5 of the measured values. The Kapitza model is applicable only if the wave amplitude $h_o \Phi$ is small in comparison to the average film thickness h_o i.e. h is essentially independent of time

and longitudinal distance. On the contrary, the experimental film structure data of Kim show that the wave amplitude is approximately equal to the average film thickness. This may explain the unsatisfactory predictions of wavelength and total liquid flow rate by the Kapitza model in climbing film flow. Furthermore, the velocity profile proposed by the Kapitza model is simply the result of a laminar film analysis and doesn't consider the variation of the film surface with time and longitudinal distance. The Kapitza model must be further refined to be applicable to climbing film flow.

The effect of the climbing film on the air velocity profile was also studied by Kim. The position of maximum velocity of the annular air stream moved toward the outer wall with increasing liquid flow rate suggesting the climbing film created a rough wall condition. The inner portion of the air velocity profile was correlated by Nikuradse's rough tube relation similar to that proposed by Shearer and Nedderman (67). The outer portion of the air velocity profile was unaffected by the presence of the liquid film and was correlated by a logarithmic equation previously reported for single phase flow.

Kim also reported local shear stresses at the various interfaces within the system. Shear stresses at the outer wall were measured directly by means of a Preston (60) tube and agreed very well with values calculated from pressure gradient and maximum gas velocity data. As pointed out before, the shear stress at the outer

wall was essentially independent of liquid flow rate.

The shear stress at the solid-liquid interface was calculated from film thickness, pressure gradient and maximum gas velocity data. At the lowest air flow rate, a negative value of the shear stress was predicted indicating possible downflow within the climbing film at low gas flow rates. Also, the shear stress at the solid-liquid interface was estimated to be less than that at the air-water interface.

Analysis of Electrochemical Measurement of Mass Transfer Coefficients in Climbing Film Flow

The difficulties involved in determining the fluid dynamics of the climbing film are considerable, primarily, since it is nearly impossible to probe the very thin film without disturbing it. It is thought that theoretical descriptions of the climbing film can best be tested by means of accurate local measurements rather than by the total liquid flow approach. In the following sections are presented the theoretical expressions required to determine the mass and momentum transfer at the solid-liquid film interface by means of an electrochemical mass transfer method.

Electrochemical Reaction

The electrolytic reaction at the cathode was the reduction of ferricyanide ion to ferrocyanide ion

$$Fe(CN)_6^{-3} + e^- \rightarrow Fe(CN)_6^{-4} .$$

The reverse reaction occurs at the anode. This redox couple was suitable in the present study since in alkaline solutions it was relatively stable, its reaction rapid, and the critical flow rate (54) was not reached in these experiments. The system has been studied extensively in oxygen-free systems by other investigators (3, 4, 20, 28, 54, 59, 62, 63, 65, 66).

Analysis of Mass Transfer-Controlled Electrochemical Reaction in a Cell

In electrode reactions two processes are involved: reaction kinetics at the electrode, and mass transfer to the electrode, commonly referred to as chemical (activation) polarization and concentration polarization, respectively. In the study of rates of mass transfer at electrodes, conditions are usually arranged so that chemical polarization is negligible. Theoretically, the electrode reaction need not proceed with negligible chemical polarization in the study of mass transfer; however, since it is extremely difficult to obtain experimentally accurate values of the concentration, c_w at the solid-liquid interface, mass transfer coefficients are most easily obtained when the over-all transfer process is concentration polarization controlled.

In a working electrolytic cell the rate of reaction is given by

the current in the cell. In general, the greater the applied potential the faster the reaction proceeds. The relation between current and voltage is given as

$$E_{total} = (E_c + E_a) + \bar{\eta}_c + \bar{\eta}_a + \eta_c + \eta_a + iR_{cell} \qquad (1)$$

where $\bar{\eta}$ and η are the chemical polarization and concentration polarization, respectively. E_c and E_a are given by the well known Nernst equation

$$E = E^o - \frac{RT}{nF} \ell n \, (a_{products}/a_{reactants}) \qquad (2)$$

where E^o is the standard electrode potential. Consider the following electrochemical reactions: At the cathode ferricyanide ion is reduced to ferrocyanide ion

$$Fe(CN)_6^{-3} + e \rightarrow Fe(CN)_6^{-4}$$

and Equation 2 is written

$$E_c = E_c^o + 0.058 \log(Fe(CN)_6^{-3}/Fe(CN)_6^{-4})$$

where $E^o = 0.46$ volts. At the anode ferrocyanide ion is oxidized to ferricyanide ion

$$Fe(CN)_6^{-4} \rightarrow Fe(CN)_6^{-3} + e$$

and Equation 2 is written

$$E_a = E_a^o + 0.058 \log (Fe(CN)_6^{-4}/Fe(CN)_6^{-3})$$

where $E_a^o = -0.46$ volts. If equimolar concentrations of $Fe(CN)_6^{-3}$ and $Fe(CN)_6^{-4}$ are present, the over-all cell reaction is zero, and $(E_c + E_a)$ vanishes from Equation 1.

As previously stated chemical polarization is due to the kinetics at the electrode surface. However, the ferri-ferrocyanide redox couple reacts very rapidly with a minimum of chemical polarization on "clean" nickel electrodes (20). Therefore, the total voltage due to reaction in the cell may be written as

$$E_t = \eta_c + \eta_a + iR_{cell} \tag{3}$$

Concentration polarization is due to the rate of transfer of ions from the bulk solution to the electrode surface. Ions may be transferred by migration, diffusion and convection. Since the bulk motion contribution vanishes for the case at hand, the total rate of mass transfer to the electrode may be written as

$$\vec{N} = \frac{i}{AnF} = \bar{k}_c (c_b - c_w) + \frac{i(t_i)}{AnF} \tag{4}$$

A simplification is achieved by adding a large excess of an indifferent electrolyte to the solution. The term t_i becomes very

small, the migration current becomes negligible and nearly all the electrolysis current arises from the oxidation-reduction of ions which arrive at the electrode by diffusion. An estimate of the migration current given in Appendix E shows it to be of the order of 1% of the total current. Thus, Equation 4 simplifies to

$$\frac{i}{AnF} = \bar{k}_c (c_b - c_w) \tag{5}$$

At the limiting current the interfacial concentration c_w becomes zero, and the rate of mass transfer is expressed as

$$\frac{i_L}{AnF} = \bar{k}_c c_b \tag{6}$$

where $\bar{k}_c$ is the mass transfer coefficient and is a function of Reynolds number, Schmidt number and geometry.

The concentration polarization at the cathode as given by Glasstone (25) is

$$\eta_c = \frac{RT}{F} \ln \frac{\bar{k}_c F a_b}{\bar{k}_c F a_b - i/A_c} \tag{7}$$

If ferricyanide ion concentration is low, $a_b = c_b$, under ideal solution conditions ($\gamma = 1$); and

$$\eta_c = \frac{RT}{F} \ln \frac{\bar{k}_c F c_b}{\bar{k}_c F c_b - i/A_c} \tag{7a}$$

Similarly, at the anode

$$\eta_a = \frac{RT}{F} \ln \frac{\bar{k}_c F c_b + i/A_a}{\bar{k}_c F c_b} \tag{8}$$

If η_a is minimized all concentration polarization is due only to ionic transfer to the cathode. Anodic concentration polarization is small if the anode area is large enough to not limit the circuit current in any way. However, at limiting current polarization at the cathode is dominant; anodic polarization according to Equation 8 being relatively small, viz, $\frac{RT}{F} \ln 2$, whereas, at the cathode the polarization becomes very large. Therefore, Equation 3 becomes

$$E_t = \eta_c + iR_{cell} \tag{9}$$

This relation describes the typical polarization curves for the ferricyanide system as shown in Figure 47 in Appendix H. Limiting current is obtained at the flat portion of the curve. The occurrence of a limiting current confirms that the reaction is diffusion controlled.

In this manner experimental mass transfer coefficients can be determined from Equation 6. It should be noted that this development

doesn't require the existence of any special type of fluid dynamics near the electrode surface.

The Unsteady Character of Flow Near a Wall

The major resistance to mass transfer between a solid wall and a fluid in fully developed turbulent flow is a thin layer of fluid in laminar motion adjacent to the surface. For most flow systems the average velocity profile in a portion of the flow field ($y^+ < 5$) is described by the equation of rectilinear laminar motion even though the flow in this region may be highly unsteady. The unsteady character of flow near a wall has long been recognized by fluid dynamicists and has been amply demonstrated (21, 50, 63, 65, 69). Sternberg (69) has suggested that even though wall turbulence is of relatively high intensity, it does not significantly influence the transfer of momentum within the region $y^+ < 5$.

Except for a few investigations (8, 17), the study of the unsteady flow nature near the solid-liquid boundaries of two-phase (gas-liquid) flow systems has not been extensive. To better understand the flow character of thin films this work initiated a study of the fluctuation in the rate of electrochemical mass transfer to the solid wall in climbing film flow. The electrochemical technique as applied by Hanratty and co-workers (56, 62, 63, 65) provides a means of investigating the mechanics of turbulent exchange with a

wall. Under diffusion controlled conditions, the concentration at the electrolytic surface is constant and equal to zero. Therefore, any sudden transfer of material from the bulk stream greatly affects the instantaneous rate of transfer. The resulting fluctuations in the mass transfer coefficient can be related to the fluctuating velocity gradient at the electrode surface (56, 63).

In their studies of electrochemical mass transfer to a small electrode on a pipe wall, Reiss and Hanratty (62) noted that for low Reynolds numbers (laminar flow regime) there are no recorded fluctuations in the rate of mass transfer to the electrode. At a Reynolds number of 2,140 a slight wavy disturbance was noted. These disturbances increased in the transition region and were observed to greatly increase in frequency and intensity as the Reynolds number further increased to fully developed turbulent flow conditions. Therefore, the electrochemical technique for the measurement of mass transfer coefficients provides a possible means to study the character of flow of the liquid film in climbing film flow.

The Effect of Dissolved Oxygen on the Redox Method for the Measurement of Mass Transfer Coefficients

In the past the electrochemical technique utilizing a ferri-ferrocyanide redox couple has been restricted to oxygen-free systems in order to eliminate possible adverse effects. Since the effects of air in contamination of the redox test solution and of the test

electrodes are complex, much uncertainty exists concerning the real effect of air on the measurements. Since oxygen activation polarization on most electrodes is very high, it is improbable that actual electrochemical reaction involving oxygen occurs in the voltage range required in this experimentation.

Other factors, such as mixed potentials (9) and oxide films on the electrodes, are possible.

However, absorption of air by any solution and contamination of electrodes are time dependent. Therefore, suitable electrochemical measurements may be obtained before adverse effects become controlling. With these ideas in mind a preliminary study was carried out in a pipe flow system to explore more fully the limitations of the electrochemical technique with respect to the effects of dissolved oxygen in solution. Such results are important in situations where the presence of air is unavoidable as in climbing film flow. These results are presented in Appendix D.

In conjunction with Figures 44 and 45 in the preliminary study, the effect of dissolved oxygen on the mass transfer coefficient in climbing film flow may be estimated by referring to Table VI in Appendix G. This table presents the percent saturation of dissolved oxygen of the climbing film at the position of the test electrodes in the two-phase flow system.

Analysis of Climbing Film Flow

The Equations of Change for the Climbing Film

In this investigation the liquid film flows upward on the inner concentric core of an annulus. The simplified steady state equations of momentum, continuity, and continuity of mass for this flow system are: (see Figure 1)

$$\frac{\rho u}{g_c}\frac{\partial u}{\partial x} = -\frac{\partial P}{\partial x} + \frac{1}{r}\frac{\partial}{\partial r}(r\tau) - \frac{\rho g}{g_c} \tag{10}$$

$$0 = \frac{\partial P}{\partial r}$$

$$\frac{\partial u}{\partial x} + \frac{1}{r}\frac{\partial (rv)}{\partial r} = 0 \tag{11}$$

$$u\frac{\partial c}{\partial x} + v\frac{\partial c}{\partial r} = D_{AB}\left[\frac{\partial^2 c}{\partial x^2} + \frac{1}{r}\frac{\partial}{\partial r}\left(r\frac{\partial c}{\partial r}\right)\right] \tag{12}$$

Under certain conditions the film thickness is negligible compared to the diameter of the inner core and curvature may be neglected. For this case, the motion of the liquid film is quasi-two dimensional and the above equations may be written in rectangular co-ordinates.

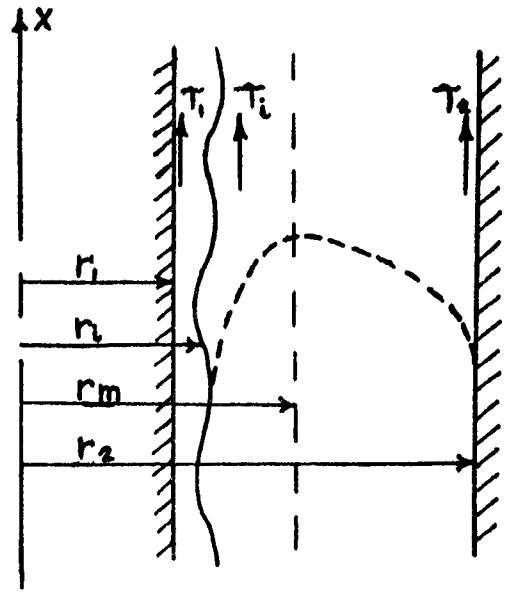

Figure (1) Section of Annular Duct Showing Climbing Film

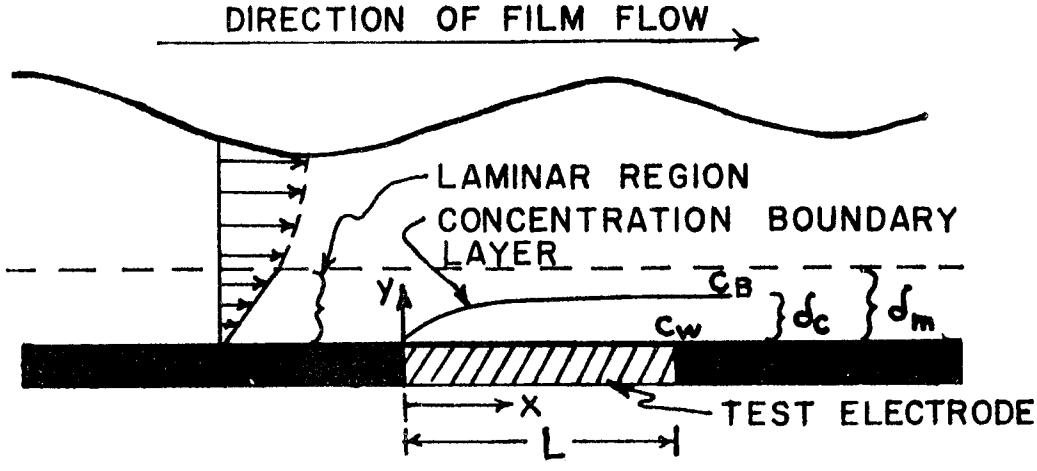

Figure (2) Mass Transfer at the Solid-Liquid Interface

Estimation of Momentum Transfer in Climbing Film Flow

The equation of motion for the climbing film flow system as shown in Figure 1 is

$$\frac{\rho u}{g_c}\frac{\partial u}{\partial x} = -\frac{\partial P}{\partial x} + \frac{1}{r}\frac{\partial}{\partial r}(r\tau) - \frac{\rho g}{g_c} \quad . \tag{10}$$

Assuming: (1) $\frac{\partial P}{\partial x}$ is constant; (2) no mass transfer between the gas and liquid either by diffusion or entrainment; and (3) no radial variation in total pressure, one may obtain the following relationships

$$\frac{dP}{dx}\int_1^2 r\,dr + \frac{\rho g}{g_c}\int_1^2 r dr + \frac{\rho}{g_c}\int_1^2 u\frac{du}{dx} r dr = [r\tau]_1^2$$

$$\frac{dP}{dx} + \frac{\rho g}{g_c} + \frac{(\rho/g_c)}{(r_2^2 - r_1^2)}\frac{d}{dx}\int_1^2 u^2 r dr = \frac{2[r\tau]_1^2}{(r_2^2 - r_1^2)} \tag{13}$$

Applying Equation (13) to various regions of the annulus, one may obtain the following momentum equations for each region:

For the liquid film $(r_1 < r < r_i)$

$$\frac{dP}{dx} + \frac{\rho_L g}{g_c} + \frac{(\rho_L/g_c)}{R_L(r_2^2 - r_1^2)}\frac{d}{dx}\int_{r_1}^{r_i} u^2 r dr = \frac{2(r_i\tau_i - r_1\tau_1)}{R_L(r_2^2 - r_1^2)} \tag{14}$$

where

$$R_L = \frac{(r_i^2 - r_1^2)}{(r_2^2 - r_1^2)}$$

For the inner portion of the gas phase $(r_i < r < r_m)$

$$\frac{dP}{dx} + \frac{\rho_G g}{g_c} + \frac{(\rho_G/g_c)}{R_1(r_2^2 - r_1^2)} \frac{d}{dx} \int_{r_i}^{r_m} u^2 r dr = - \frac{2 r_i \tau_i}{R_1(r_2^2 - r_1^2)} \qquad (15)$$

where

$$R_1 = \frac{(r_m^2 - r_i^2)}{(r_2^2 - r_1^2)}$$

For the outer portion of the gas phase $(r_m < r < r_2)$

$$\frac{dP}{dx} + \frac{\rho_G g}{g_c} + \frac{(\rho_G/g_c)}{R_2(r_2^2 - r_1^2)} \frac{d}{dx} \int_{r_m}^{r_2} u^2 r dr = - \frac{2 r_2 \tau_2}{R_2(r_2^2 - r_1^2)} \qquad (16)$$

where

$$R_2 = \frac{(r_2^2 - r_m^2)}{(r_2^2 - r_1^2)}$$

For the entire gas phase $(r_i < r < r_2)$

$$\frac{dP}{dx} + \frac{\rho_G g}{g_c} + \frac{(\rho_G/g_c)}{R_G(r_2^2 - r_1^2)} \frac{d}{dx} \int_{r_i}^{r_2} u^2 r dr = - \frac{2(r_2 \tau_2 + r_i \tau_i)}{R_G(r_2^2 - r_1^2)} \qquad (17)$$

where

$$R_G = \frac{(r_2^2 - r_i^2)}{(r_2^2 - r_1^2)}$$

For both streams $(r_1 < r < r_2)$

$$\frac{dP}{dx} + (\rho_L R_L + \rho_G R_G)\frac{g}{g_c} + \frac{\rho_L/g_c}{(r_2^2 - r_1^2)} \frac{d}{dx} \int_{r_1}^{r_i} u^2 r dr$$

$$+ \frac{(\rho_G/g_c)}{(r_2^2 - r_1^2)} \frac{d}{dx} \int_{r_i}^{r_2} u^2 r dr = - \frac{2(r_2\tau_2 + r_1\tau_1)}{(r_2^2 - r_1^2)} \tag{18}$$

where R_L and R_G have previously been defined.

The integral terms in Equations (14) through (18) are negligible compared to the other terms and may be neglected. Therefore, one may obtain the following shear stress relationships

$$\tau_1 = \frac{1}{r_1}\left[r_i\tau_i - \alpha\frac{(r_i^2 - r_1^2)}{2}\right] \tag{19}$$

$$\tau_i = \tau_2 \frac{r_2}{r_i} \frac{R_1}{R_2} \tag{20}$$

$$\tau_2 = \beta\frac{(r_m^2 - r_2^2)}{2r_2} \tag{21}$$

where $\alpha = \left(\frac{dP}{dx} + \frac{\rho_L g}{g_c}\right)$ and $\beta = \frac{dP}{dx} + \frac{\rho_G g}{g_c}$

Substitution of Equation (20) into Equation (19) gives

$$\tau_1 = \frac{2R_1 r_2 \tau_2 - \alpha R_2(r_i^2 - r_1^2)}{2r_1 R_2} \tag{22}$$

If the pressure gradient, point of maximum velocity, film thickness and shear stress at the outer wall are known, the shear stress at the solid-liquid interface (τ_1) may be calculated and compared with values obtained via independent measurements.

Generally, entrainment is present for most two phase gas-liquid film flows. Equations (14) through (18) may still be used to estimate two phase flow parameters if the density of the gas core is available from entrainment data. For such a case

$$\rho_G = \chi \rho_G + (1-\chi)\rho_L \tag{23}$$

where χ is the quality (weight fraction) of the gas phase. Since entrainment data is not available for the present system, no relation involving the density of the gas core was used for calculations in this work. Equation (23) shows that even a small amount of entrained liquid greatly affects the density of the gas core since liquid density is much larger than gas density. For further discussion of the effect of entrainment on the interfacial shear refer to Levy (53).

Mass Transfer at the Solid-Liquid Interface

Consider the liquid film flowing over a smooth test electrode under the following conditions: (1) the liquid properties are constant; (2) the surface concentration is uniform $(c_w = 0)$; (3) the undisturbed liquid bulk concentration is c_b; (4) mass transfer is due to diffusion

alone; (5) curvature is neglected; (6) the test electrode is short (for small values of $y \quad \partial^2 c/\partial x^2 <<< \partial^2 c/\partial y^2$); (7) the concentration boundary layer is within the laminar sublayer which is fully developed; and (8) the velocity of the liquid near the wall is $u=\bar{c}y$, $v=0$, $w=0$.

The resulting equation of continuity of mass for the liquid film as shown in Figure 2 is

$$\bar{c}\, y \frac{\partial c}{\partial x} = D_{AB} \frac{\partial^2 c}{\partial y^2} \tag{24}$$

and the boundary conditions are

$y > 0$	$x > 0$
$x = 0$	$y = 0$
$c = c_b$	$c = c_w = 0$.

This boundary value problem was solved by Leveque (as cited by Knudsen and Katz (46, p. 363)), and the local mass transfer coefficient is given by

$$k_{c_x} = \frac{D_{AB}}{0.893} \left(\frac{\bar{c}}{9 D_{AB} x} \right)^{1/3} \tag{25}$$

The average mass transfer coefficient is given as

$$\bar{k}_c = 1.68\, D_{AB} \left(\frac{\bar{c}}{9 D_{AB} L} \right)^{1/3} \tag{26}$$

Using this relation one can estimate the momentum transfer to the inner core wall by means of experimental mass transfer data.

Velocity Gradient and Shear Stress at the Solid-Liquid Film Interface

Rearrangement of Equation (26) gives the following expression for the velocity gradient in the region of the wall

$$\overline{c} = 1.898\, D_{AB} L \left(\frac{\overline{k}_c}{D_{AB}}\right)^3 \qquad (27)$$

If very short sections are considered, all mass transfer may occur within a relatively thin laminar layer of fluid near the wall. In such a case the concentration boundary layer would not extend beyond the so called laminar sublayer. Whether this actually happens may be tested by using Equation (27). Mass transfer coefficient measurements for short electrodes of different sizes are used to determine $\overline{c}$. If $\overline{c}$ values for the different electrodes remain essentially constant under the same gas-liquid flow conditions, then the concentration boundary layer is within the laminar sublayer. In this case shear stresses at the inner wall may be calculated as follows:

$$\tau_1 = \frac{\mu}{g_c} \left(\frac{du}{dy}\right)_{y=0} = \frac{\mu \overline{c}}{g_c} \qquad (28)$$

and

$$\tau_1 = \frac{1.898\mu\, D_{AB} L}{g_c} \left(\frac{\overline{k}_c}{D_{AB}}\right)^3 \qquad (29)$$

Therefore shear stresses at the inner wall may be determined

from electrode length, physical properties and experimental mass transfer coefficients calculated from Equation (6).

Estimation of Mean Interfacial Shear Stress

Equation (19) gives

$$\tau_i = \frac{1}{r_i}\left[r_1\tau_1 - a\frac{\left(r_i^2 - r_1^2\right)}{2}\right]$$

where τ_i is the mean interfacial shear stress which consists both of viscous drag and form drag on the air-liquid interface. Substitution of τ_1 from Equation (29) gives

$$\tau_i = \frac{1}{r_i}\left[\frac{1.898\mu DLr_1}{g_c}\left(\frac{\bar{k}_c}{D_{AB}}\right)^3 - a\left(\frac{r_i^2 - r_1^2}{2}\right)\right] \qquad (30)$$

If the pressure gradient, film thickness, and mass transfer coefficient are known, τ_i may be determined.

The mean interfacial shear stress may also be determined using Equation (20)

$$\tau_i = \tau_2 \frac{r_2}{r_i}\frac{R_1}{R_2} \quad .$$

The film thickness, point of maximum air velocity, and shear stress at the outer wall must be known to determine τ_i from this relationship.

Estimation of Incipient Downflow

At very low gas flow rates insufficient momentum is transferred from the gas phase to the liquid film to maintain climbing film flow. Near the inner core wall the liquid film may be flowing downward even though the net flow of the film may be upward. Downflow begins when the shear stress at the solid-liquid interface is zero. From Equation (19)

$$0 = r_i \tau_i - \alpha \frac{(r_i^2 - r_1^2)}{2} \tag{31}$$

or from Equation (22)

$$0 = 2R_1 r_2 \tau_2 - \alpha R_2 (r_i^2 - r_1^2) \tag{32}$$

If the pressure gradient, point of maximum velocity, film thickness, and shear stress at the outer wall are known, downflow conditions may be estimated and compared with downflow results determined from experimental mass transfer measurements. It should be noted that Equations (31) and (32) may also be obtained from the laminar climbing film model.

Laminar Climbing Film Model

The steady state two dimensional equation of motion for the climbing film is

$$\frac{\rho u}{g_c}\frac{\partial u}{\partial x} = -\frac{\partial P}{\partial x} + \frac{1}{r}\frac{\partial}{\partial r}(r\tau) - \frac{\rho g_x}{g_c} \tag{10}$$

The following assumptions are made: (1) there is no acceleration in the fluid; (2) radial variation in pressure is zero; (3) dP/dx is constant; (4) the liquid film is of uniform thickness, r_i ; (5) no mass transfer occurs between the gas and liquid; and (6) physical properties are constant. Therefore Equation (10) reduces to

$$\frac{1}{r}\frac{\partial}{\partial r}(r\tau) = \left(\frac{dP}{dx} + \frac{\rho_L g_x}{g_c}\right) = a \tag{33}$$

If the liquid film is in laminar motion

$$\tau_l = \frac{\mu}{g_c}\left(\frac{du}{dr}\right) \tag{34}$$

The boundary conditions are:

$$\text{at} \quad r = r_l, \quad u = 0$$

$$\text{at} \quad r = r_i, \quad \frac{du}{dr} = \frac{\tau_i g_c}{\mu}$$

where r_i is the mean film thickness and τ_i is the mean interfacial shear stress. Integration and subsequent application of the boundary conditions yields the velocity profile in the film

$$u = \frac{g_c}{\mu_L}\left[\frac{a}{4}(r^2 - r_l^2) + \left(r_i\tau_i - \frac{a r_i^2}{2}\right)\ln r/r_l\right]. \tag{35}$$

The shear stress at the solid-liquid interface is

$$\tau_1 = \frac{\mu}{g_c} \left(\frac{du}{dr}\right)_{r=r_1} \tag{36}$$

which gives Equations (19) and (20). Therefore, the laminar climbing film model does have merit in that it reduces to the proper limits. Shear stress values calculated by Equation (20) may be compared with values determined from electrochemical mass transfer measurements and Equation (29).

EXPERIMENTAL PROGRAM

The purpose of this study was to investigate the mass transfer phenomena at the solid-liquid film interface in order to better understand the nature of climbing film flow. An electrochemical technique utilizing a ferro-ferricyanide redox couple was used to measure average and instantaneous mass transfer coefficients. Such measurements were desired to give some indication of the flow mechanism of the film, the extent of turbulence at the inner wall and the effect of film thickness and wave motion on the mass transfer process at the inner wall.

The following experimental program was carried out to accomplish the aforesaid objectives.

(1) A preliminary study was performed in a pipe flow system to test the reliability of the electrochemical technique and to explore its possible application to two-phase (air-liquid) climbing film flow. Since the method had previously been restricted to oxygen free systems, this study was concerned with the actual effect of dissolved oxygen on the measured mass transfer coefficient. The results of the preliminary study are included in Appendix D.

(2) The percentage of dissolved oxygen in the climbing film was determined at the position of the test electrodes in the two-phase flow system and is presented in Table VI in Appendix G for various

gas and liquid flow rates. These results were compared with those of the preliminary study in Appendix D to determine the effect of dissolved oxygen on the mass transfer coefficients in climbing film flow.

(3) Short ring-type electrodes were used to measure average mass transfer coefficients at the inner wall in climbing film flow. Predictions of incipient downflow and shear stress at the inner wall were made from these measurements.

(4) A small wire-type electrode was used to measure local instantaneous values of the mass transfer coefficient at the inner wall. These measurements provided information on velocity gradient fluctuations at the inner wall.

(5) Pressure gradients for minimum and equilibrium entrainment conditions were obtained over a wide range of air and liquid flow rates.

In this investigation variables were studied over the following air and liquid flow conditions: air flow rates varied from 140-385 cfm at $68^{\circ}F$ and one atm, and liquid flow rates varied from 0.2-1.46 lb_m/min.

DESCRIPTION OF APPARATUS

Two Phase Flow System

The major parts of the two phase climbing film flow system are as follows: (1) the air source, including the heat exchanger and calming section; (2) the column, including the annular test section; (3) the liquid supply, including the liquid injection section; (4) the air-liquid separator. These parts are described in detail on the following pages. A sketch of the two phase system is shown in Figure 3. Photographs of the annular test section and of the climbing film are shown in Figure 4.

Air Source

The air supply was a Sutorbuilt 8HB blower driven by a 30 HP, 1760 RPM General Electric A-C induction motor. The blower was rated at 550 cfm (1 atm and 68^{o}F) at 9 psi outlet pressure.

The air from the blower passed through a water cooled finned tube heat exchanger. The cooled air subsequently passed through a special calming section consisting of seven, 15-inch long and 7/8-inch diameter tygon-coated copper tubes. To eliminate vibration from the blower, flexible hoses were installed between the blower and the heat exchanger, and between the heat exchanger and galvanized pipe entrance section.

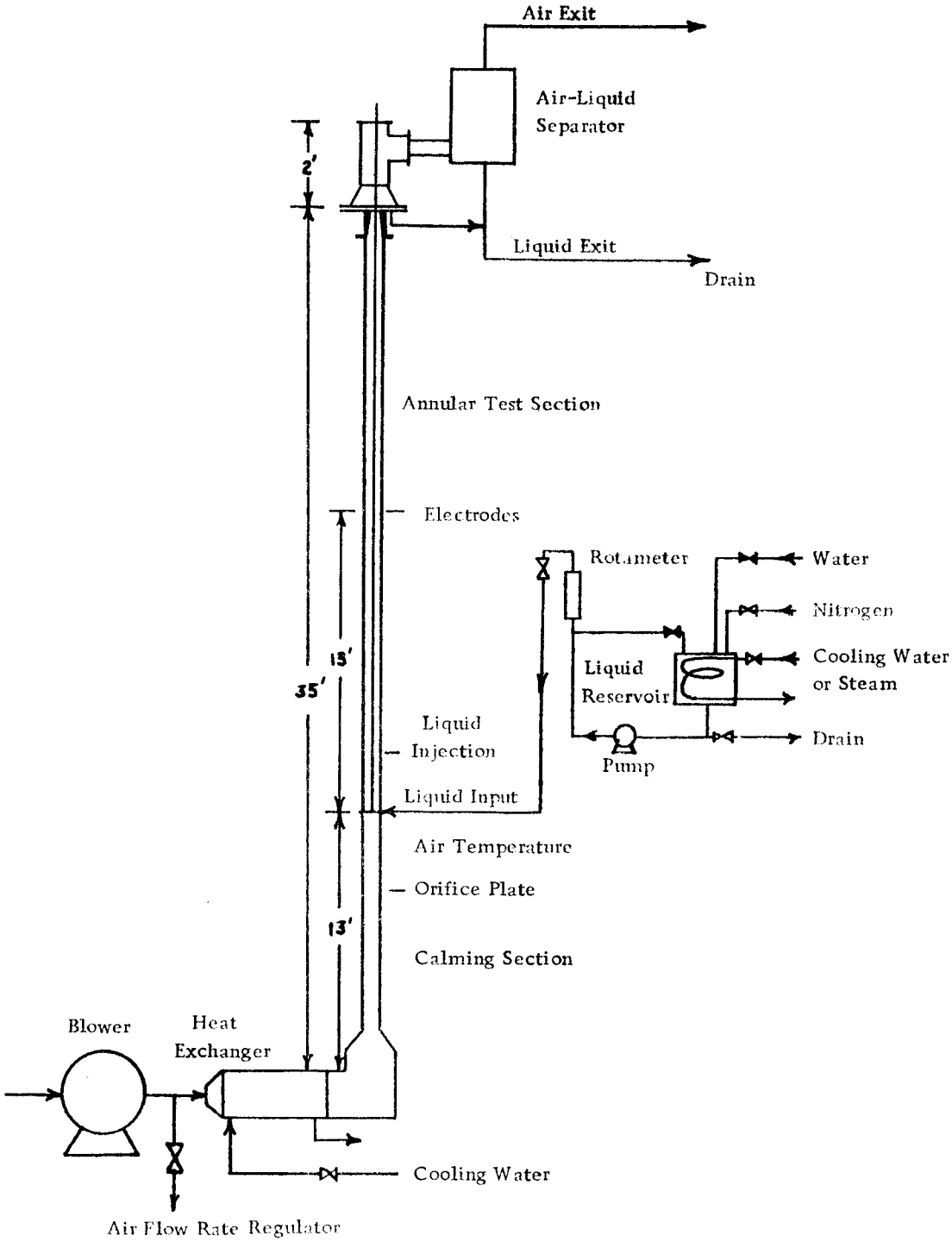

Figure (3) Schematic Flow Diagram

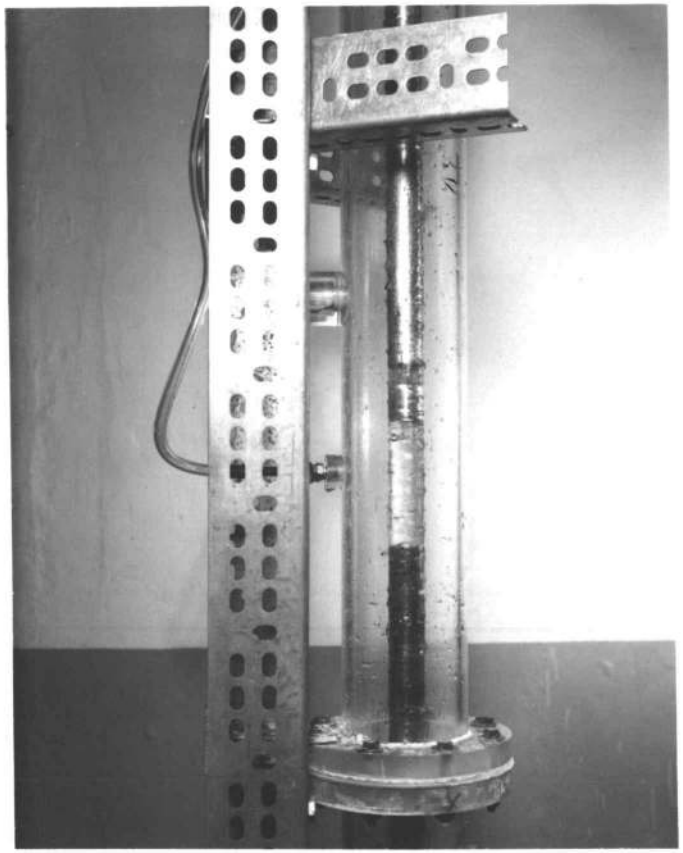

A Section of the Annular Column

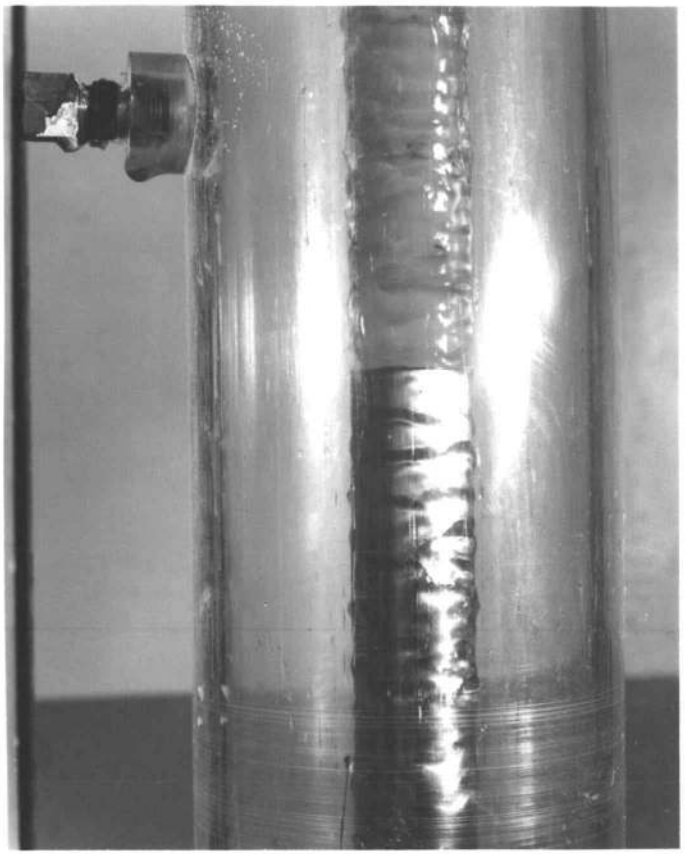

The Climbing Film

Figure (4) Photographs of the Annular Test Section and the Climbing Film

Vertical Annular Column

The over-all length of the column was about 35 feet including a 20-foot long test section. The first 13 feet consisted of a three-inch inside diameter galvanized pipe which served as support for the entire column and also as an entrance for the gas stream. The annular test section made up the remaining length of the column. It consisted of a three-inch inside diameter plexiglass tube with a one-inch outside diameter stainless-steel concentric inner core. For ease of assembly the test section was constructed in sections approximately four feet long. One of the main advantages of this test section design is that the phenomena which occur on the inner rod can be observed directly and clearly.

The entire column was well supported at various locations along its length. The inner tube was supported laterally by sets of streamlined stainless-steel centering screws. A minimum number of these screws were used to minimize artificial entrainment and disturbances.

The mass transfer measurement location was 11 feet above the liquid injector. This position was chosen by considering such factors as entrance effects, amount of entrainment present in the gas core, ease of visual observation, and ease of assembly. A sketch of the two-phase flow column is presented in Figure 5.

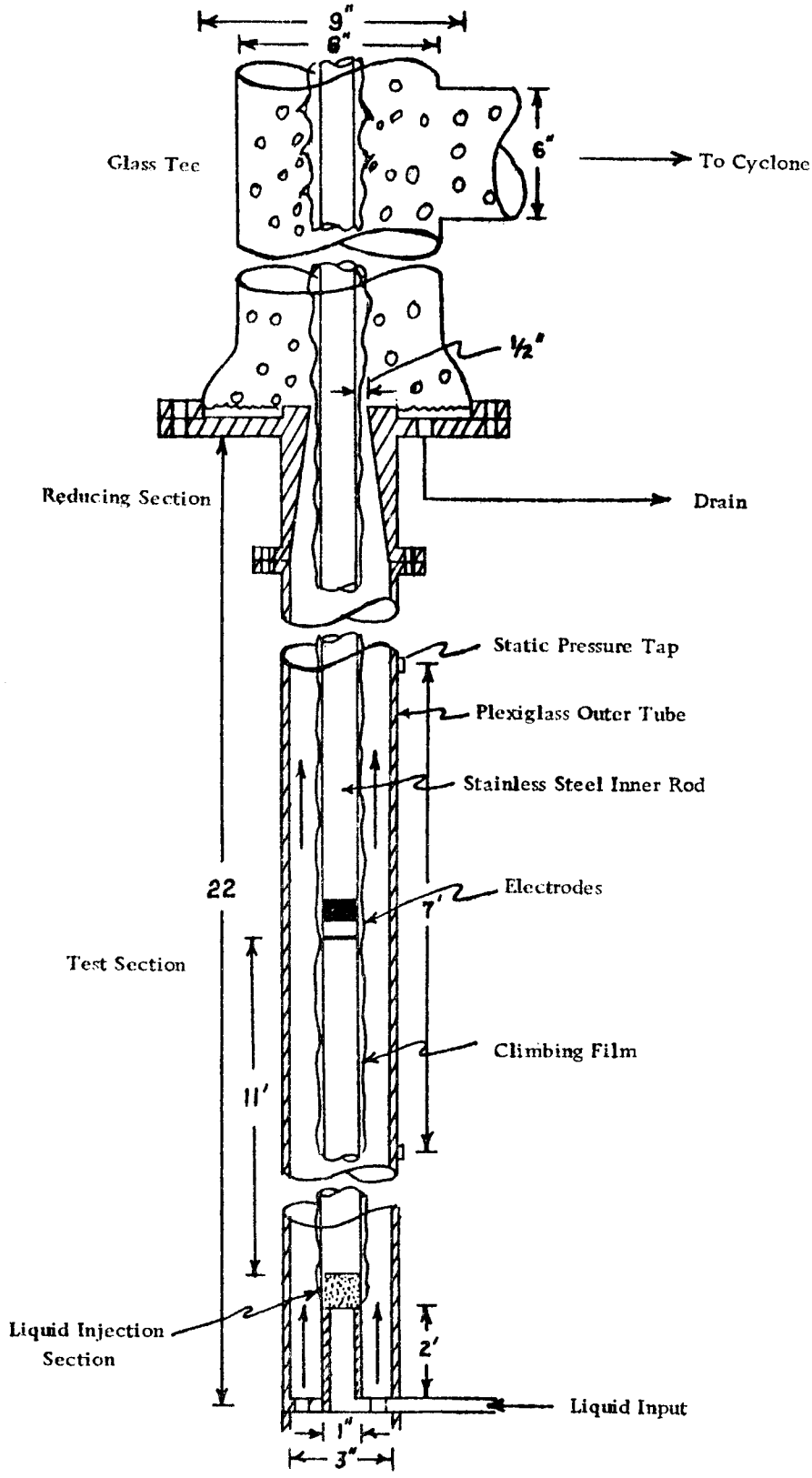

Figure (5) Two Phase Flow Column

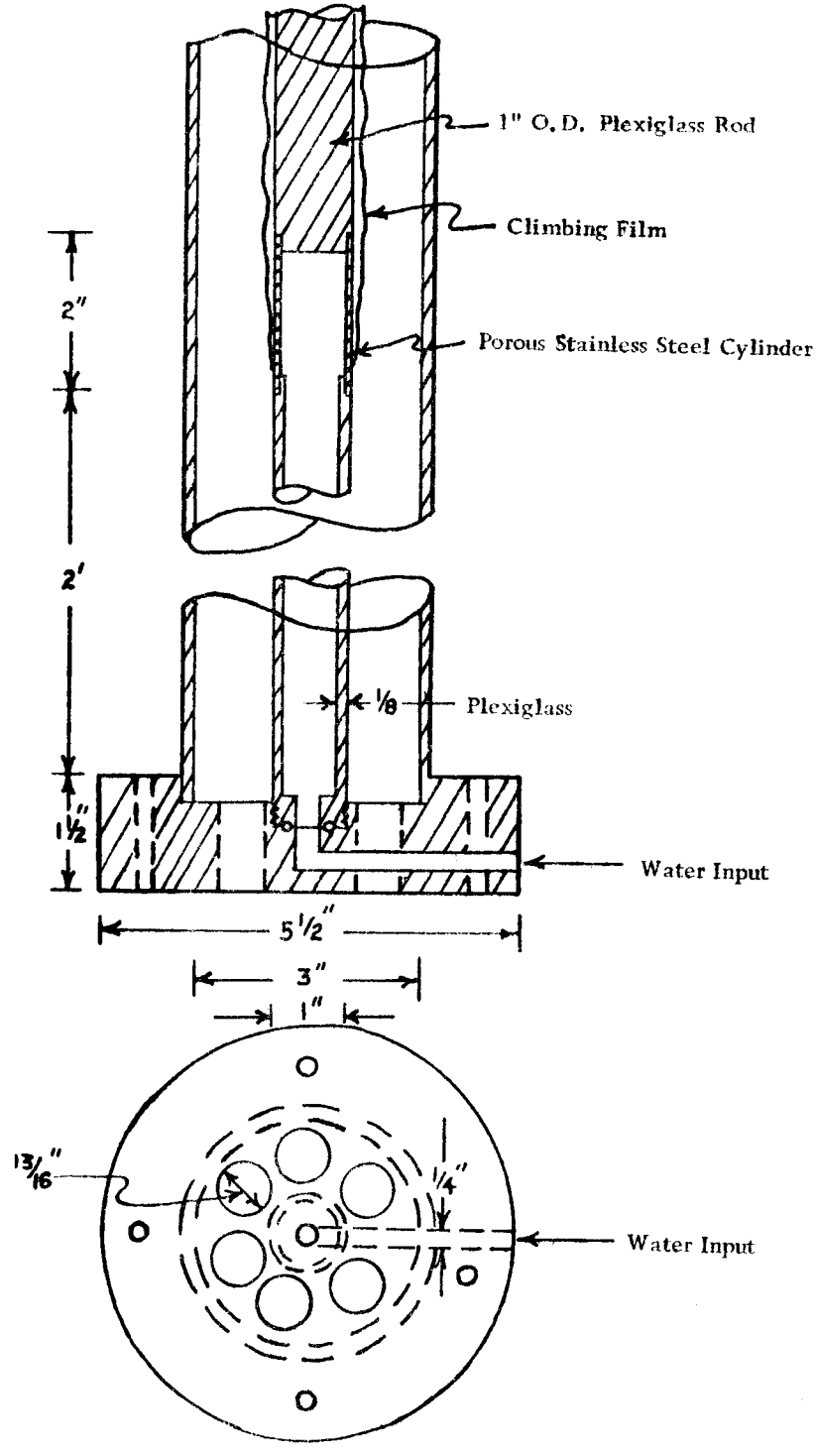

Figure (6) Liquid Injection System

Liquid Supply System

The liquid supply tank was a 15-gallon stainless-steel, steam jacketed vessel which was continuously maintained under a nitrogen atmosphere. A gear-type rotary pump mounted to a 1/4 HP, A-C motor pumped liquid from the tank through a rotameter and into the inner core as shown in Figure 3. The liquid subsequently passed through a porous stainless-steel section into the annulus. The liquid injection section, Figure 6, consisted of a one-inch outside diameter stainless-steel porous tube which was two-inches long and 3/64-inch thick.

Control of liquid flow rate was accomplished by regulation of the by-pass valve in the liquid supply line. Care was taken to ensure that liquid flow rates remained constant for each air flow condition. Liquid temperatures were controlled by regulation of the flow of cooling water or steam through the jacket of the liquid supply tank.

Air-Liquid Separator

At the end of the column the air and liquid were completely separated by means of a reducing section and a subsequent cyclone arrangement, Figure 3. Near the end of the annular test section the diameter of the outside tube decreased from three to two-inches over a length of 5 1/2-inches so that all of the liquid was completely

carried out of the test section with the air. The reducing section, Figure 5, was made from laminated plexiglass through which a conical hole was drilled. To this section a six-inch glass tee was attached. After this first expansion the air-liquid mixture flowed tangentially into a 55-gallon drum which acted as a cyclone separator. Air escaped to the atmosphere from the top of the drum through a three-inch hole. The liquid drained from the base of the drum and from the glass tee and was subsequently discarded into a sewer drain.

Electrochemical System

The major parts of the electrochemical system for measurement of mass transfer coefficients in climbing film flow are as follows: (1) the electrical circuit; (2) the test electrodes; (3) the instrumentation for measurement of fluctuations of the mass transfer coefficient; (4) the electrolyte; (5) the dissolved oxygen analyzer; (6) the climbing film temperature probe.

Electrical Circuit

A sketch of the electrical circuit employed is given in Figure 7. Lead storage batteries supplied the required emf for the electrochemical reaction within the cell. Current-voltage measurements were obtained using precision D-C ammeters and voltmeters. In order to obtain accurate electrical measurements, the meter having

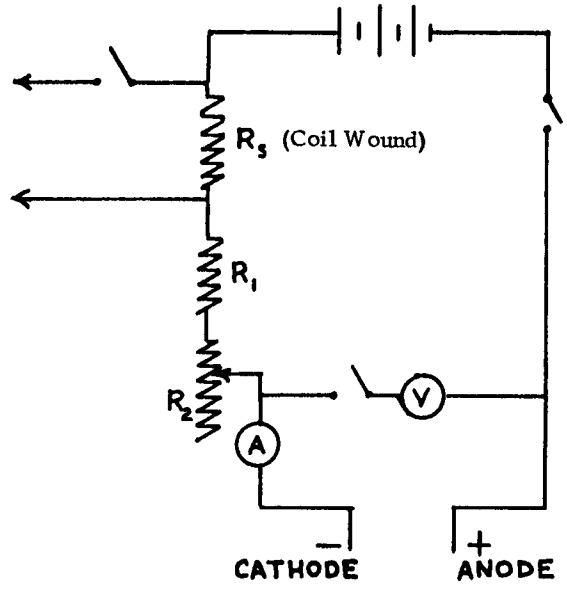

Figure (7) Electrical Circuit for Electrochemical Mass Transfer Measurements

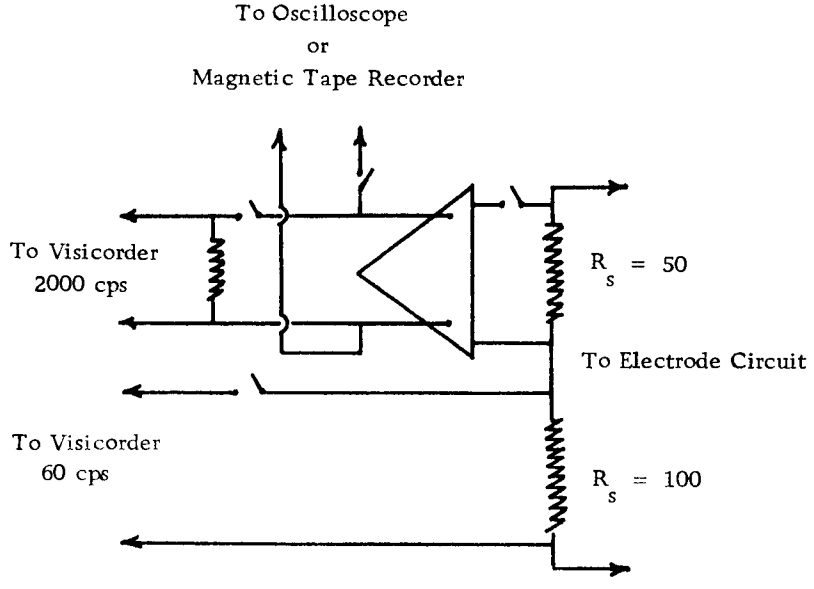

Figure (8) Measurement of Fluctuations of the Mass Transfer Coefficient

the most suitable range for a given measurement was substituted into the circuit. Simpson, Triplett, and Weston meters were used in the experiments. A summary of the pertinent current-voltage parameters used for mass transfer measurements in single phase (pipe) flow and for climbing film flow are presented in Table V in Appendix F.

Further instrumentation was accomplished by connecting appropriate devices across the standard resistors. The standard resistors were coil-wound to minimize electrical noise effects.

Test Electrodes

The test electrodes were of two types--ring electrodes and wire electrodes. Both types of electrode assemblies constituted a portion of the inner core of the annular test section.

Ring-Type Electrode Assembly

For the ring-type electrode, Figure 9-A, the electrochemical reaction was carried out between a large nickel ring (anode) and the small nickel ring (cathode) mounted flush to the inner core wall. The one-inch long anode was sufficiently large so that the current was not limited in any way. Thus, all concentration polarization effects were due only to the reaction at the cathode, although at limiting current this is usually true. The cathodes varied in length

from approximately 1/8 to 1/16-inch long.

The electrode rings were mounted concentrically onto an approximately one-inch outside diameter plexiglass rod which had been machined and threaded on each end to 5/8-inch outside diameter. A 1/2-inch long plexiglass spacer separated the electrodes. Epoxy cement was applied to the electrodes and spacer; immediately afterwards, a 1/2-inch long plexiglass spacer was screwed firmly against the anode to hold the electrodes in place. This spacer also insulated the anode from the upper section of the inner core.

Each electrode assembly was constructed so that a minimum of three inches of smooth plexiglass preceeded the test electrode (cathode) in order to eliminate disturbing the flow field near the core wall. The entire electrode assembly was machined in one operation to the dimensions of the inner core and polished smooth with rouge paper.

The test electrodes were installed in the annular test section by disassembling the top 11 feet of the column. The electrode assembly was screwed flush to the lower and upper sections of the stainless-steel inner core. Each end of the inner core had been fitted with a threaded plexiglass plug, Figure 9-C, which had been glued in place with epoxy cement. Care was taken to insure that no roughness or discontinuities existed between the stainless-steel inner rod and the electrode assembly. Each assembly remained in its

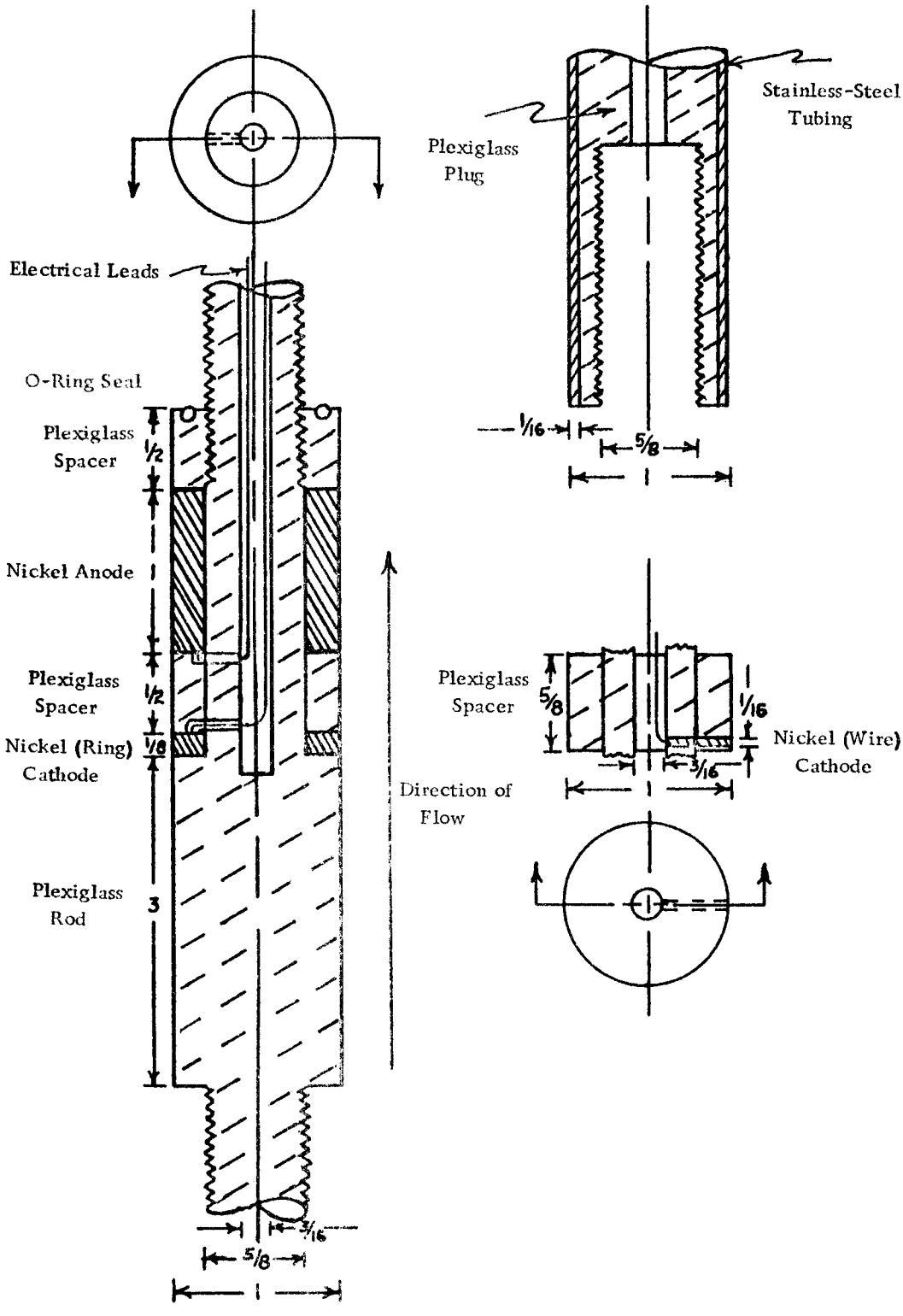

Figure (9) Electrodes

position for a series of runs.

The primary purpose of this ring-type electrode assembly was to measure mass transfer coefficients as a function of liquid and gas flow rates.

Wire-Type Electrode Assembly

The wire-type electrode assembly was essentially the same as the ring-type assembly except for the cathode design. Thus, only the cathode is shown for the wire-type electrode in Figure 9-B. The cathode was a 0.064-inch diameter (Gauge 14) nickel wire mounted flush to the inner core wall. The wire was inserted into the plexiglass spacer separating it from the anode and was held in place with epoxy cement. The entire electrode assembly was machined and polished to its proper dimensions after all components had been assembled. This type of electrode arrangement was utilized to obtain velocity gradient fluctuations at the solid-liquid film interface.

Instrumentation for Measurement of Fluctuations of the Mass Transfer Coefficient

Fluctuations in the electrochemical circuit current were recorded as voltage variations across standard resistors by a Honeywell model 1508 Visicorder. The circuit for these measurements is shown in Figure 8.

The Visicorder is a direct recording oscillograph for data with

frequencies ranging from DC to 5000 cycles per second. It utilizes highly sensitive Honeywell galvanometers which produce high amplitude trace deflections with extremely small current inputs. All Honeywell galvanometers when properly damped give a flat frequency response within ± 5% up to 60% of their undamped natural frequency. In the present work galvanometers having undamped natural frequencies of 100 cps and 3000 cps were used.

A Tektronix type 122 AC-coupled preamplifier with differential input was used in the circuit to amplify the voltage signal from the standard resistor. The common mode rejection ratio of this amplifier was used to eliminate the DC-component. The signal from the amplifier could be sent either to the visicorder (3000 cps galvanometer) or to a Tektronix type 545A oscilloscope. Adjustment of the low and high frequency response positions of the amplifier and subsequent observation of the oscilloscope trace allowed one to determine the approximate frequency range of the signal.

Electrolyte

For all climbing film flow experiments the electrolyte used was a 0.025-equimolar solution of potassium ferricyanide and potassium ferrocyanide in 2N NaOH. The sodium hydroxide acted as an indifferent electrolyte to eliminate any migration due to ionic transference effects. The solutions were prepared just prior to the runs

using specially treated distilled water. Nitrogen had been bubbled through the distilled water to eliminate dissolved oxygen. A positive nitrogen pressure was maintained on the flow system, Figure 3, during the course of the experiments. Precautions were taken to keep the test solution away from light. Potassium ferrocyanide slowly decomposes in light to form hydrogen cyanide which would poison the electrodes. However, decomposition of the ferrocyanide complex can be practically eliminated in alkaline solutions which are kept in darkness (47).

The redox solutions were prepared by accurately weighing reagent grade chemicals followed by dilution to the proper volume. Solution concentrations are estimated to be accurate to within ± 0.5%. The physical properties of the redox system are presented in Appendix B.

Dissolved Oxygen Analyzer

The dissolved oxygen content of the electrolyte was monitored by a Beckman Oxygen Analyzer model 777. This is a direct readout instrument based on the polarographic principle for the analysis of gaseous and dissolved oxygen. It is composed of two basic units--a sensor and an amplifier. The sensor consists of a gold cathode and silver anode surrounded by a Teflon permeable membrane. When oxygen diffuses through the membrane, it is electrically reduced at

the cathode by an applied voltage. This reaction causes a current to flow between the anode and cathode which is proportional to the partial pressure of oxygen in the test sample. The sensor signal is amplified and may then be read directly on the meter.

To obtain dissolved oxygen measurements the sensor is inserted into the sample gas or solution, and the value of oxygen is read on the meter scale in the units used in calibration. For accurate measurements in liquids, a minimum flow rate of the sample is required. The minimum flow rate is the lowest rate at which the maximum reading is obtained on the meter. In this experimentation a magnetic stirrer was used with a small sample bottle (100 ml) to ensure accurate dissolved oxygen measurements.

The analyzer is accurate to ± 5% full scale with temperature variations within 15 to 45°C. If the temperature is constant the accuracy of the instrument is within ± 1% full scale. In the present investigation the temperature of the electrolyte was kept at 75± 2°F while the sensor was kept near room temperatures (70°F-80°F).

Calibration

By exposing the sensor to air the device was calibrated at the sample temperature to read percent saturation of dissolved oxygen in solution, 100 percent oxygen saturation corresponding to 160 mm Hg partial pressure under atmospheric conditions. The sensor could

then be used with any solution and the percent saturation of dissolved oxygen determined directly from the meter. Since the Henry's law constant ($p = Hx$) for the redox solution used in this work was not available, and since no quantitative procedure for the determination of dissolved oxygen in the redox solution was available, it was impossible to relate percent saturation to actual oxygen content in ppm. However, this disadvantage was minimal since only relative values of dissolved oxygen were needed in this study--refer to Figure 44 in Appendix D.

Climbing Film Temperature Probe

A probe shown in Figure 10 was constructed to measure the temperature of the climbing film. The probe consisted of a copper ring concentrically embedded in a length of plexiglass rod. Two copper-constantan thermocouples were embedded in the copper ring. The temperature of the probe was determined by measuring the emf generated between the ring and a reference cold junction.

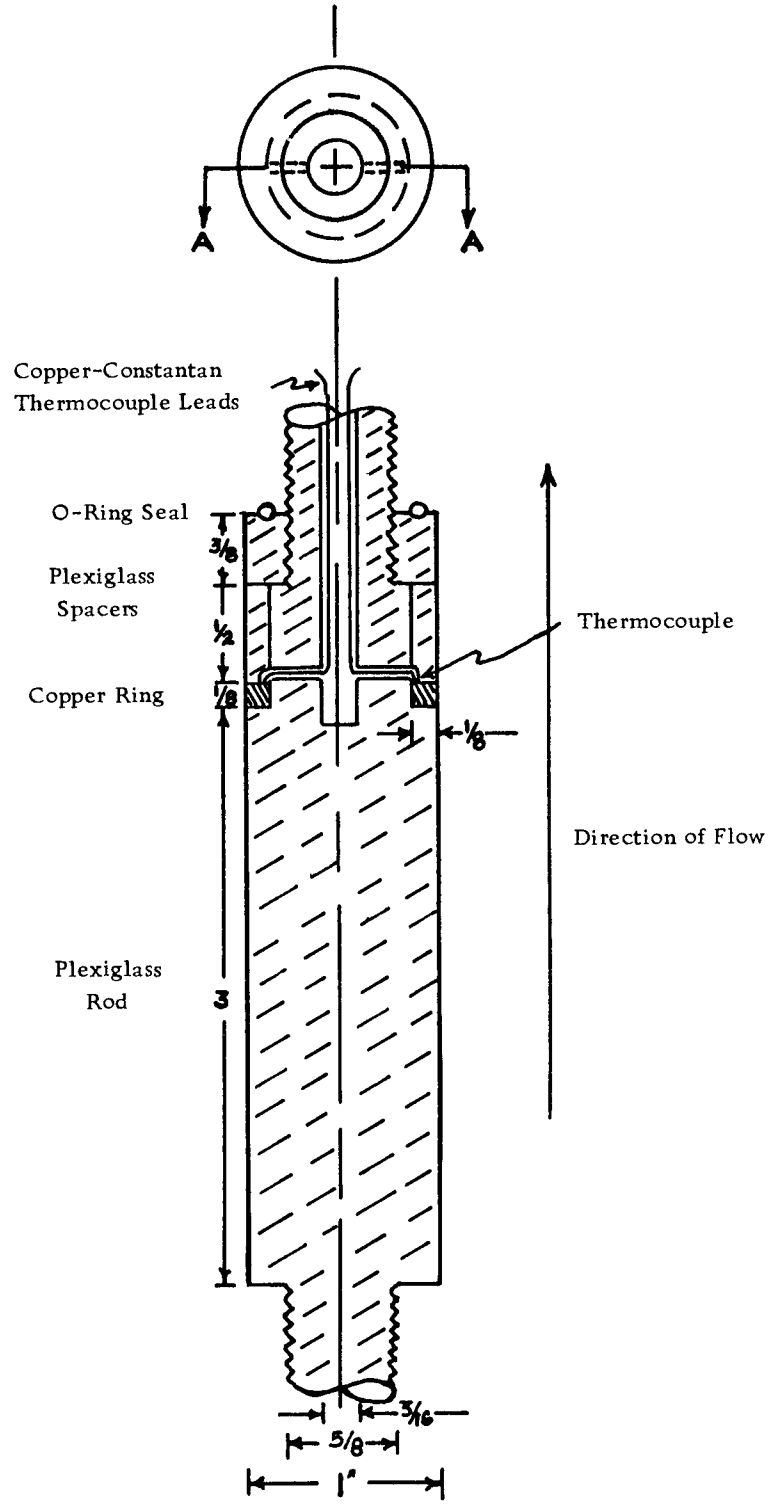

Figure (10) Climbing Film Temperature Probe

EXPERIMENTAL PROCEDURE

Liquid Flow Measurement

Liquid flow rates were measured by means of a Manostat Predictability Flowmeter no. FM1048B utilizing a glass float. The meter was directly calibrated for a 0.025 equimolar potassium ferri-ferrocyanide solution in 2N sodium hydroxide. The meter was guaranteed by the manufacturer to be accurate to within 2% of full scale.

Liquid flow rates varied between 0.2 lb/min to 1.47 lb/min. It was difficult to form stable films below flow rates of 0.2 lb/min since dry patches would form causing the liquid to flow in several narrow rivulets dispersed around the circumference of the inner core of the annulus. Since the present investigation is limited to the climbing film regime with liquid flowing only on the inner core of an annulus, liquid flow rates greater than 1.46 lb/min were not used. At higher liquid flow rates liquid also flows as a film on the outer tube wall of the annulus due to an accumulation of entrained liquid from the film on the inner core.

Air Flow Measurement

Air flow rates were measured by means of a calibrated two-inch, sharp-edged orifice made from 1/16-inch brass sheet. The orifice was calibrated with a critical flow prover, Meteric Orifice

Flow Prover Type CR, size 2 made by the American Meter Company. The calibration was checked by integration of velocity profiles obtained by Kim (45). The accuracy of the air flow measurements is estimated to be ±1%. The calibration curve and temperature correction information are presented in Appendix A.

Radius taps were installed on each side of the orifice plate, and were connected to a 36-inch differential manometer containing a fluid of specific gravity 2.962. The approximate location of the orifice plate in the column is shown in Figure 3. Care was taken to position the orifice at a point far upstream from any flow disturbance.

Measurement of Humidity of Inlet Air

In the climbing film flow system simultaneous heat and mass transfer occurs at the air-liquid interface. The humidity of the inlet air plays an important role in this process and affects the temperature of the liquid film. Thus, during each experiment wet bulb and dry bulb temperatures at 1 atm pressure were measured at the blower inlet. The percent relative humidity was determined by reference to a pyschometric chart. Since the total moisture content was not affected by the blower nor the cooler, the molal humidity prior to the liquid injection section was equal to that of the inlet air.

Measurement of Climbing Film Temperature

The temperature probe, Figure 10, was calibrated using an accurate thermometer in a constant temperature bath. Thermocouple emfs were measured by means of a Leeds and Northrup potentiometer. The temperature of the probe agreed very well with the Leeds and Northrup thermocouple calibration for copper-constantan thermocouples.

The calibrated temperature probe was located at the same position in the two-phase flow system as were the electrolytic cells. At steady state the probe measured the temperature of the film at the inner core wall where all mass transfer occurred. It was possible to obtain the film temperature as a function of inlet air and liquid temperatures, air and liquid flow rates, and inlet air humidity. Film temperatures were obtained over a working range of the above variables, and the results are shown in Figures 32-36 in Appendix C. The maximum error of the film temperature measurements as presented in these charts is estimated to be within $\pm 1.0^{\circ}F$.

Measurement of Pressure Gradient

Pressure gradients were measured by means of a 50-inch inclined (14.27° from the horizontal) differential manometer filled with fluid of 0.83 specific gravity. Since liquid droplets on the outer wall

create a rough wall condition, pressure measurements were obtained before and after equilibrium entrainment conditions were reached.

In climbing film flow the number of liquid droplets on the outer wall increase with length of column and accumulate with time until equilibrium entrainment conditions prevail. The amount of entrainment is dependent upon the gas and liquid flow rates. However, in the range of flows studied, 90-100% of the liquid in the column is estimated to flow as a film even under the most adverse conditions.

Pressure gradients without liquid droplets on the outer wall were obtained in the following manner. The liquid rate was set to zero, and the system was blown clean of liquid by a high rate of gas flow. The climbing film was then formed under the desired liquid and gas flow conditions. When the film was completely formed in the column, the pressure drop was measured.

All pressure taps were connected to a purging system supplied with dry air. The purpose of the purging system was to insure that the pressure lines were free of entrained liquid while pressure gradients were measured. Pressure lines were purged prior to each measurement. A simplified schematic diagram of the pressure measurement system is presented in Figure 11.

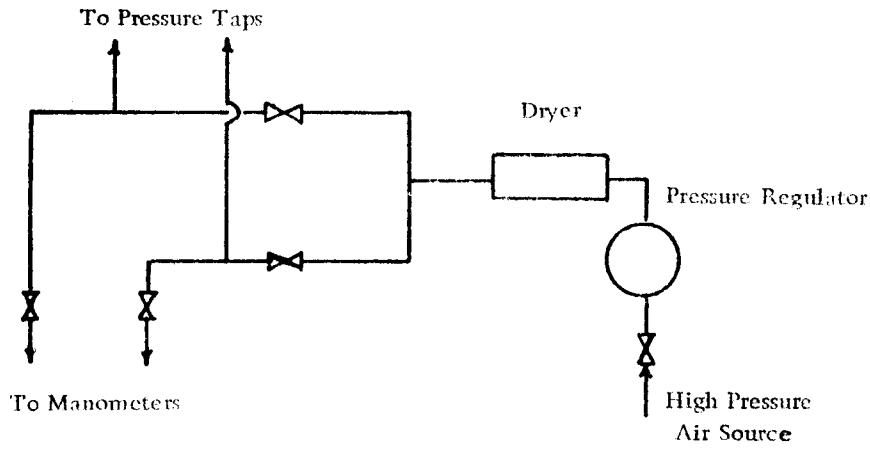

Figure (11) Pressure Measurement System

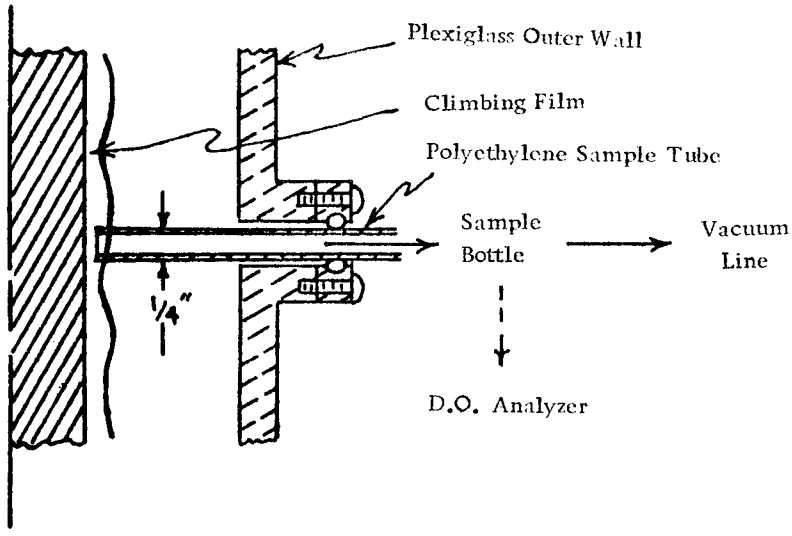

Figure (12) Measurement of Dissolved Oxygen of the Climbing Film

Measurement of Dissolved Oxygen

Pipeflow

The oxygen analyzer was used to establish suitable operating limits for the electrochemical measurement of mass transfer coefficients in the presence of dissolved oxygen. This was done under conditions of single phase turbulent pipe flow and the results are fully described in Appendix D.

Climbing Film Flow

The oxygen analyzer was used to determine the increase in percentage of dissolved oxygen in the redox solution as it flowed upward through the two-phase system. Prior to its injection into the annular test section, the liquid was completely saturated with nitrogen; hence, the solution in the liquid reservoir was maintained at approximately ten percent oxygen saturation. The dissolved oxygen content of the climbing film was measured about six inches above the test electrodes. It was not feasible to directly measure the percent saturation of dissolved oxygen in the film using the electrolytic probe of the oxygen analyzer. The thin climbing film tended to channel around the probe leaving insufficient liquid to be measured. Instead, samples of redox solution were obtained using a simple 1/4-inch diameter polyethylene tube which traversed the annular space and impinged on

the climbing film. The tube was connected to a sample bottle and subsequently to a vacuum line. When sufficient solution was obtained, the percent saturation of dissolved oxygen in solution was measured using the oxygen analyzer. To account for the amount of oxygen absorbed by the sample solution during the measurement procedure, suitable corrections were made on the data.

A schematic diagram of this arrangement is presented in Figure 12. The experimental results are presented in Appendix G.

Measurement of Limiting Current

All experimental mass transfer data were obtained at limiting current which was determined from a plot of average current vs potential similar to the curve in Figure 47 in Appendix H. Limiting current is obtained at the flat portion of the curve. Under these conditions the current was controlled by the rate of mass transfer of ferricyanide ions to the surface of the working electrode at which the concentration of the ferricyanide ions was zero.

A sketch of the electrical circuit used is given in Figure 7. A potential was applied between the anode and the cathode, and the current in the circuit was measured. Adjustment of the rheostat in the circuit permitted the determination of the entire polarization curve. Some time elapsed whenever the circuit variables were changed before steady state was reached. For the wire electrode only a few

seconds were required, whereas, for the one-inch ring electrode which was used in the pipe flow system almost a minute was necessary.

Limiting current data which were obtained as a function of liquid and gas flow rates were used to determine average mass transfer coefficients and fluctuating mass transfer coefficients. If temperature is constant, limiting current data are accurate within ± 1%. Because of temperature variations, the limiting current data of this work were repeatable to within ± 2.5%.

Measurement of Fluctuations of Mass Transfer Rate

The fluctuations in the local rate of mass transfer at the solid-liquid film interface were obtained at limiting current using the wire-type electrode. Unlike a large electrode which tends to average the effects of flow disturbances in the adjacent flow field, a small wire electrode is very sensitive to such disturbances. The fluctuations were recorded as voltage variations across the standard resistors shown in Figure 8. These voltage variations could be recorded on the visicorder or tape recorder and simultaneously monitored by the oscilloscope.

Cleaning of Test Electrodes

Prior to the installation of the electrodes in the two phase

system, they were cleaned with carbon tetrachloride. Each electrode remained in the system for a series of experiments. Before each experimental run, the electrodes were cathodically cleaned in 5% NaOH solution at a current density of 20 ma. for 12-15 minutes to minimize chemical polarization effects (20, 59). The film flow rate of the caustic solution was approximately 0.79 lb/min while the air flow was about 200 cfm. Following each run the cell was inspected to ascertain if adverse corrosion deposits had formed on the electrode surface during the experiment. In general, no such deposits were formed during the experimental runs if the aforementioned cleaning procedure was followed. Failure to properly clean the electrodes causes erroneous mass transfer results as shown in Appendix D.

In the oxygen-free pipe flow system, the electrolyte was continuously recirculated; however, for the two-phase flow system it was discarded after it passed through the annular test section. This procedure was followed to eliminate the decomposition of the electrolyte, and to maintain the electrodes as active as possible. Care was also taken to operate the electrolytic cell no longer than three hours without recleaning the electrodes.

EXPERIMENTAL RESULTS

Mass Transfer Coefficients at the Solid-Liquid Film Interface

Figures 13-16 summarize the experimental data for the 1/8-inch and 1/16-inch electrodes. Figures 13-15 present $\bar{k}_c$ as a function of air flow rate with liquid flow rate as parameter, whereas, Figure 16 presents $\bar{k}_c$ as a function of liquid flow rate with air flow rate as parameter. The data is plotted in this manner in order to examine the relative effects of air and liquid flow rates on the mass transfer process.

The experimental mass transfer results are also presented in Table VII in Appendix H. Mass transfer coefficients were calculated from Equation 6 using limiting current data similar to the curves in Figure 47 in Appendix H. The experimental mass transfer coefficients are reproducible within 2.5% with temperature variation and are considered accurate to $\pm 5\%$ As shown in Appendix G, the effect of dissolved oxygen on $\bar{k}_c$ is less than 2% for the flow rates studied.

Fluctuations in Rate of Mass Transfer to a Wire Electrode

Visicorder traces of the fluctuations in the rate of mass transfer to a small wire electrode are shown for various flow conditions

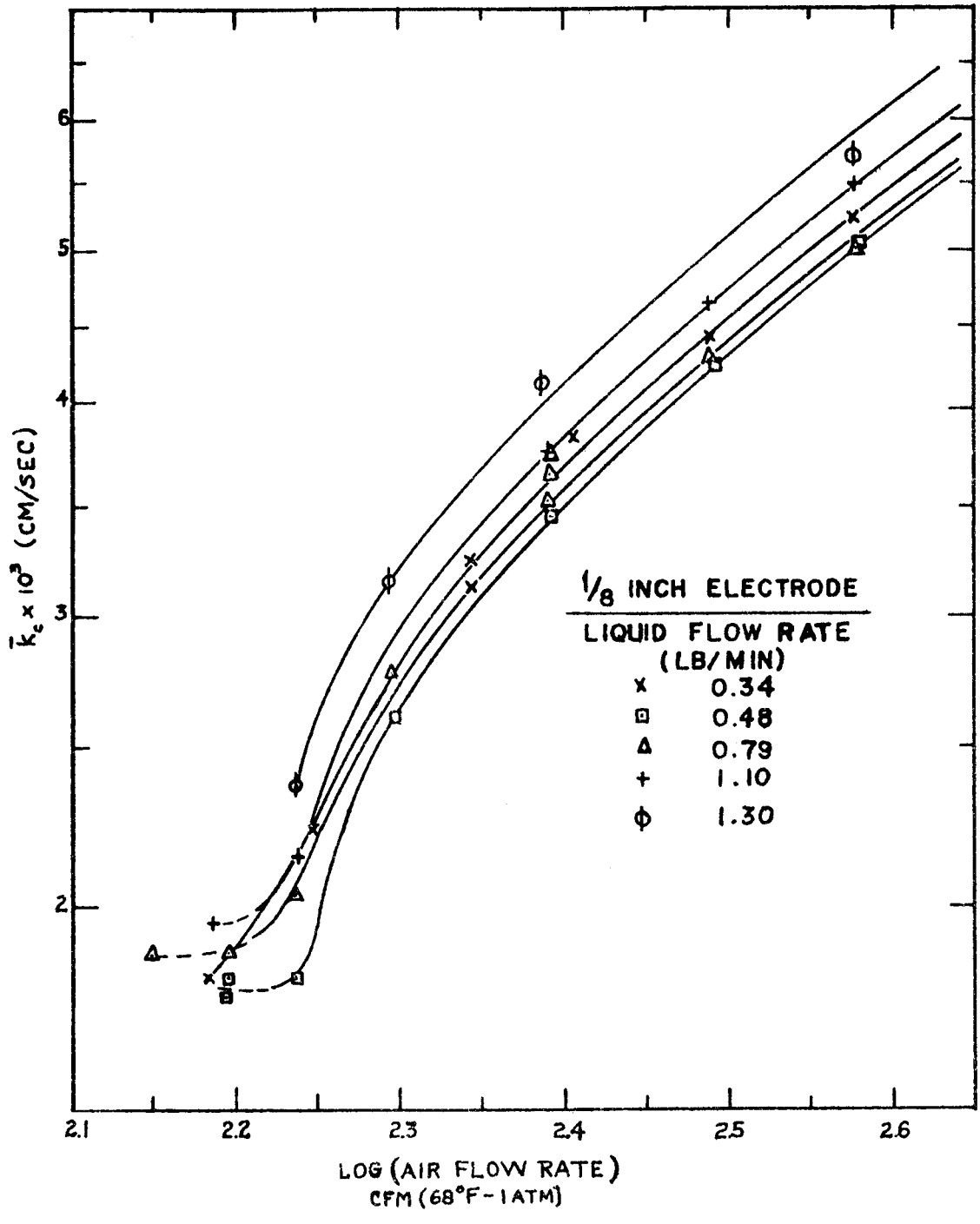

Figure (13) Mass Transfer Coefficient vs. Air Flow Rate

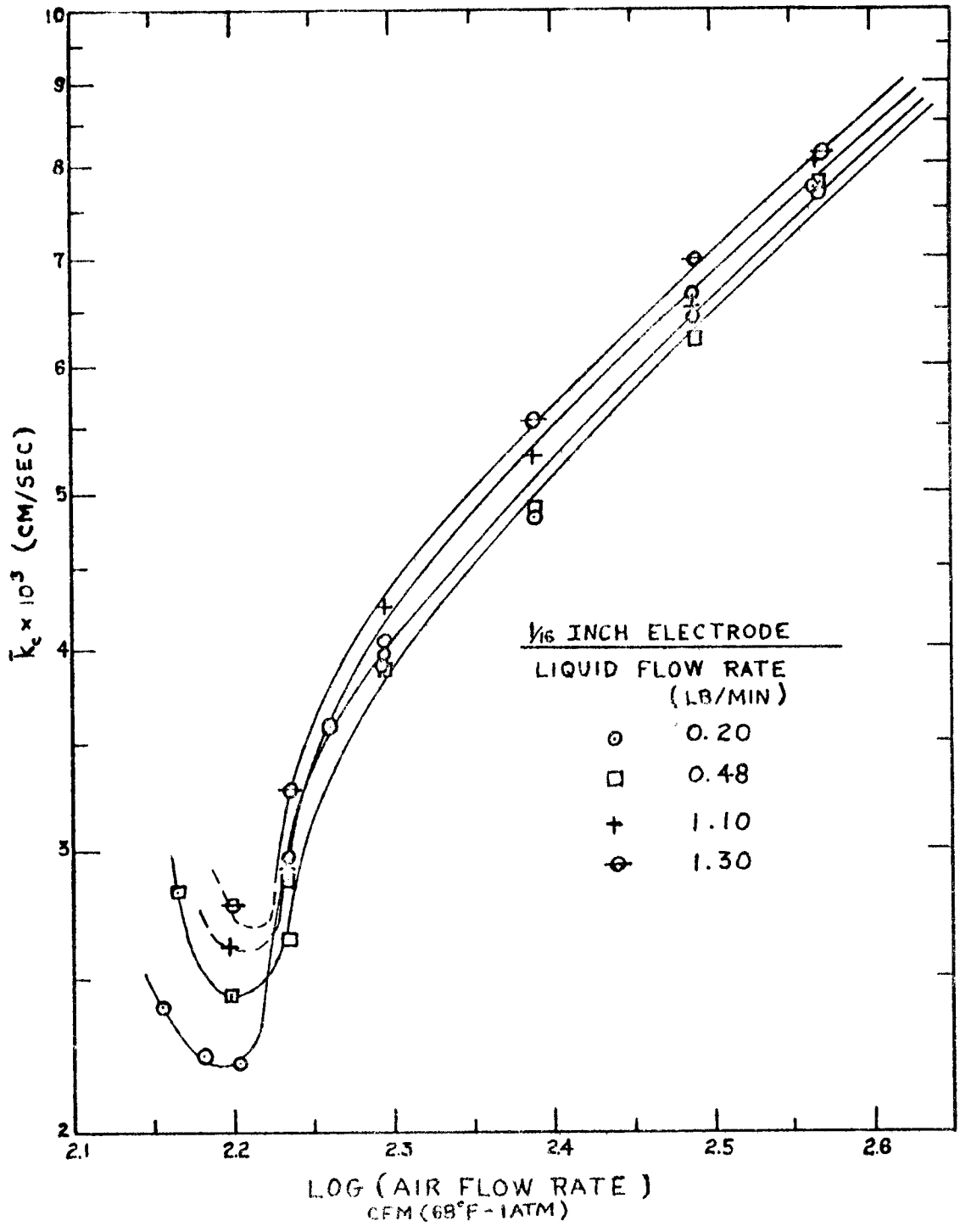

Figure (14) Mass Transfer Coefficient vs. Air Flow Rate

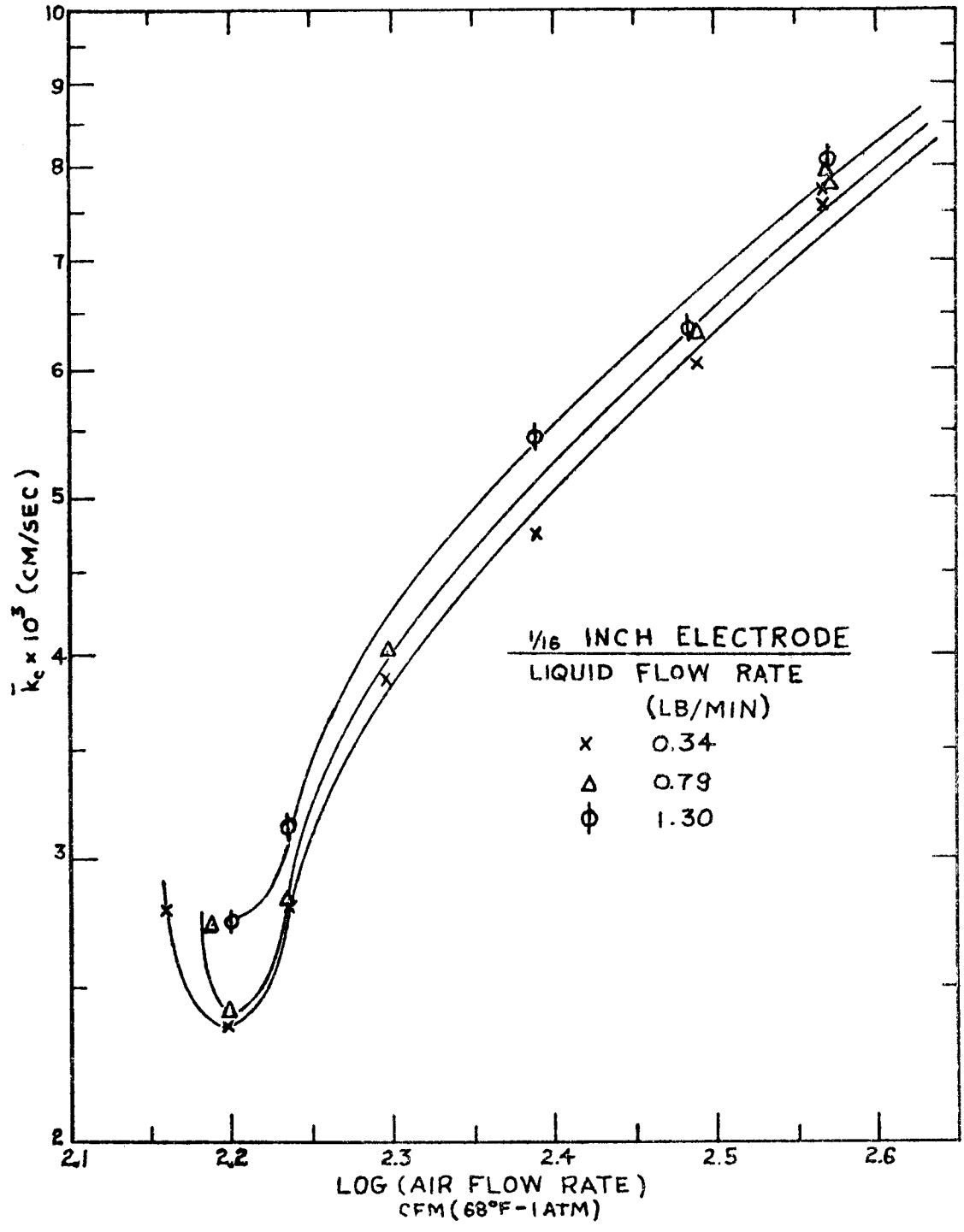

Figure (15) Mass Transfer Coefficient vs. Air Flow Rate

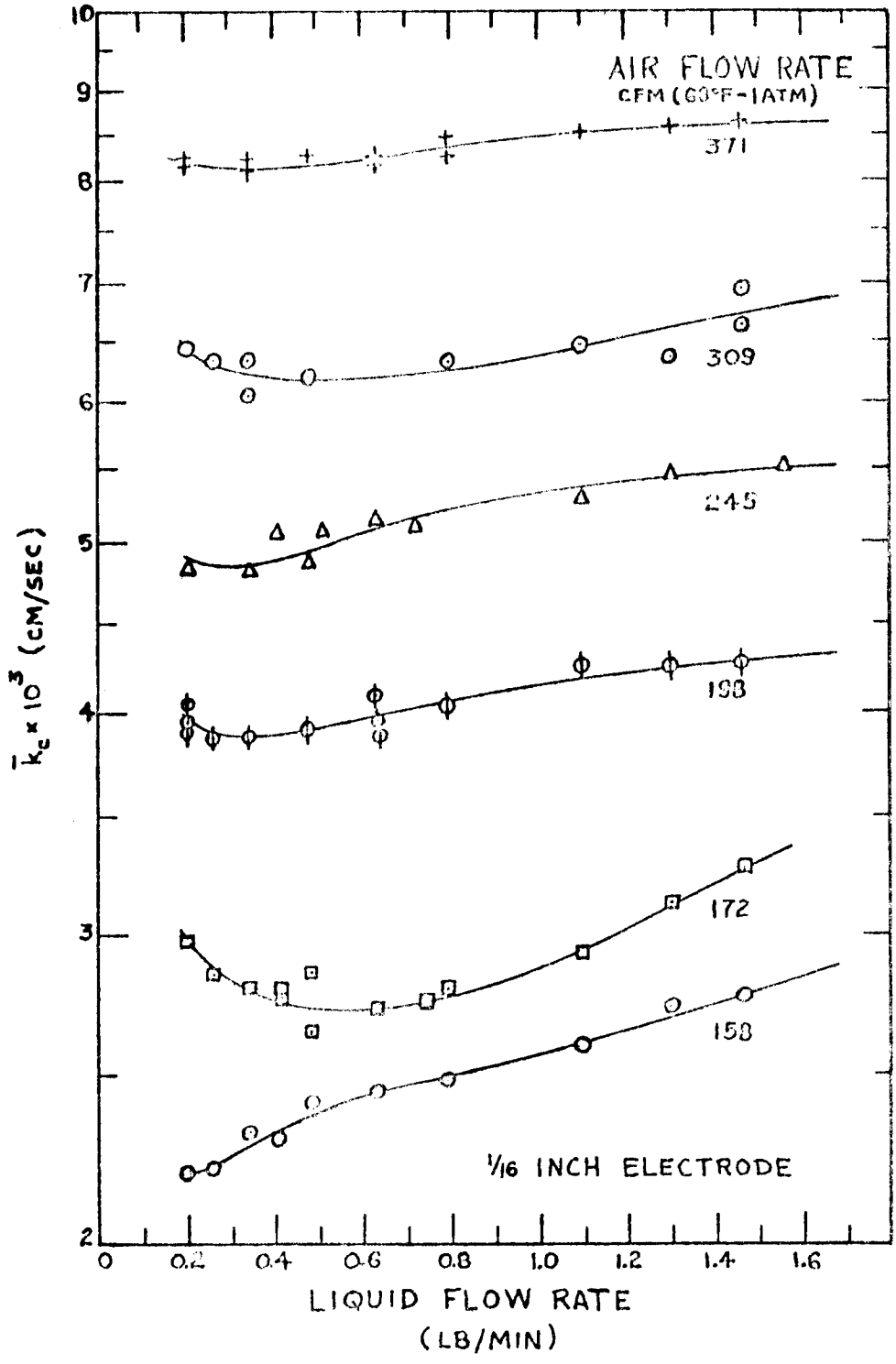

Figure (16) Mass Transfer Coefficient vs. Liquid Flow Rate

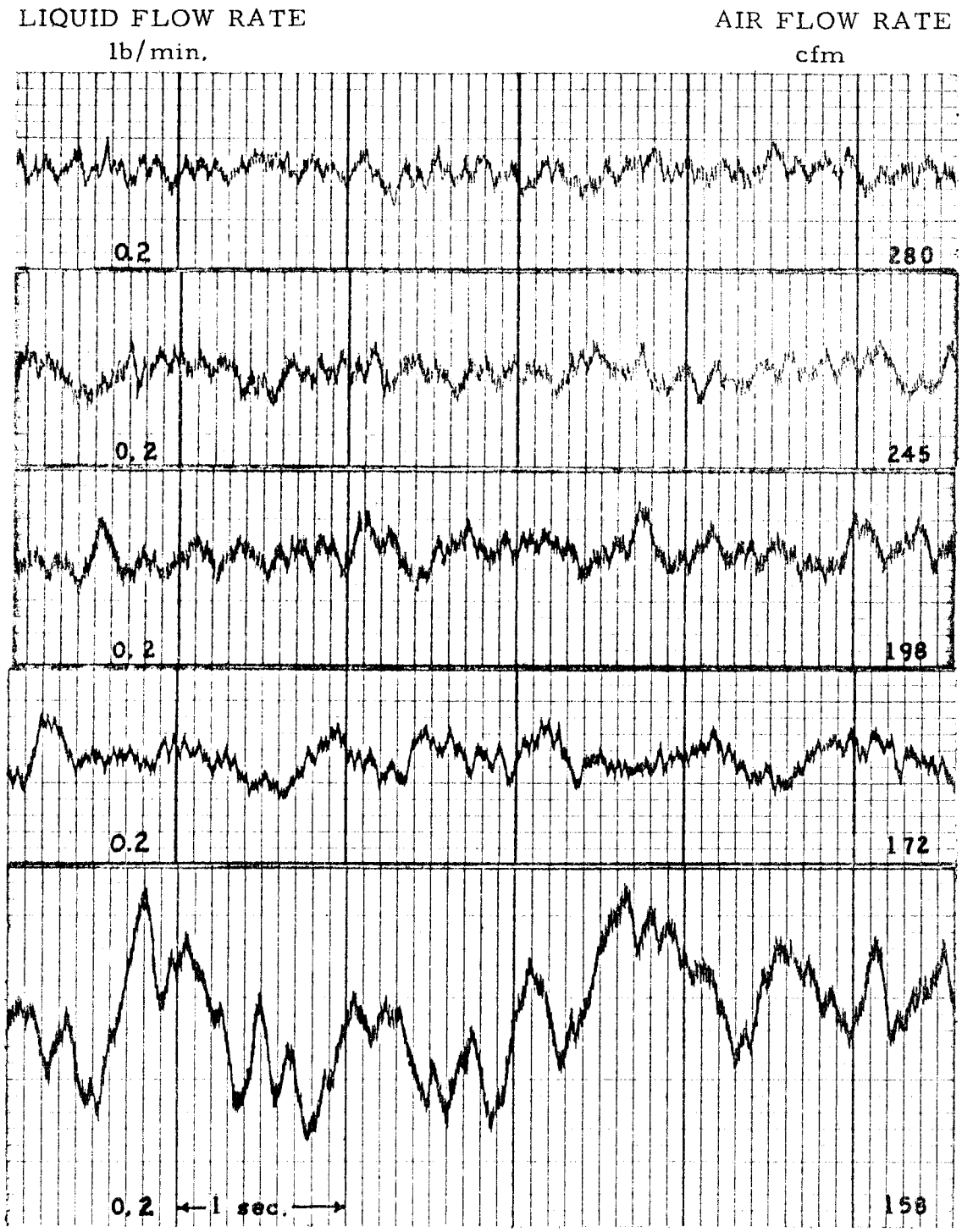

Figure (17) Fluctuations in the Rate of Mass Transfer at the Solid-Liquid Film Interface

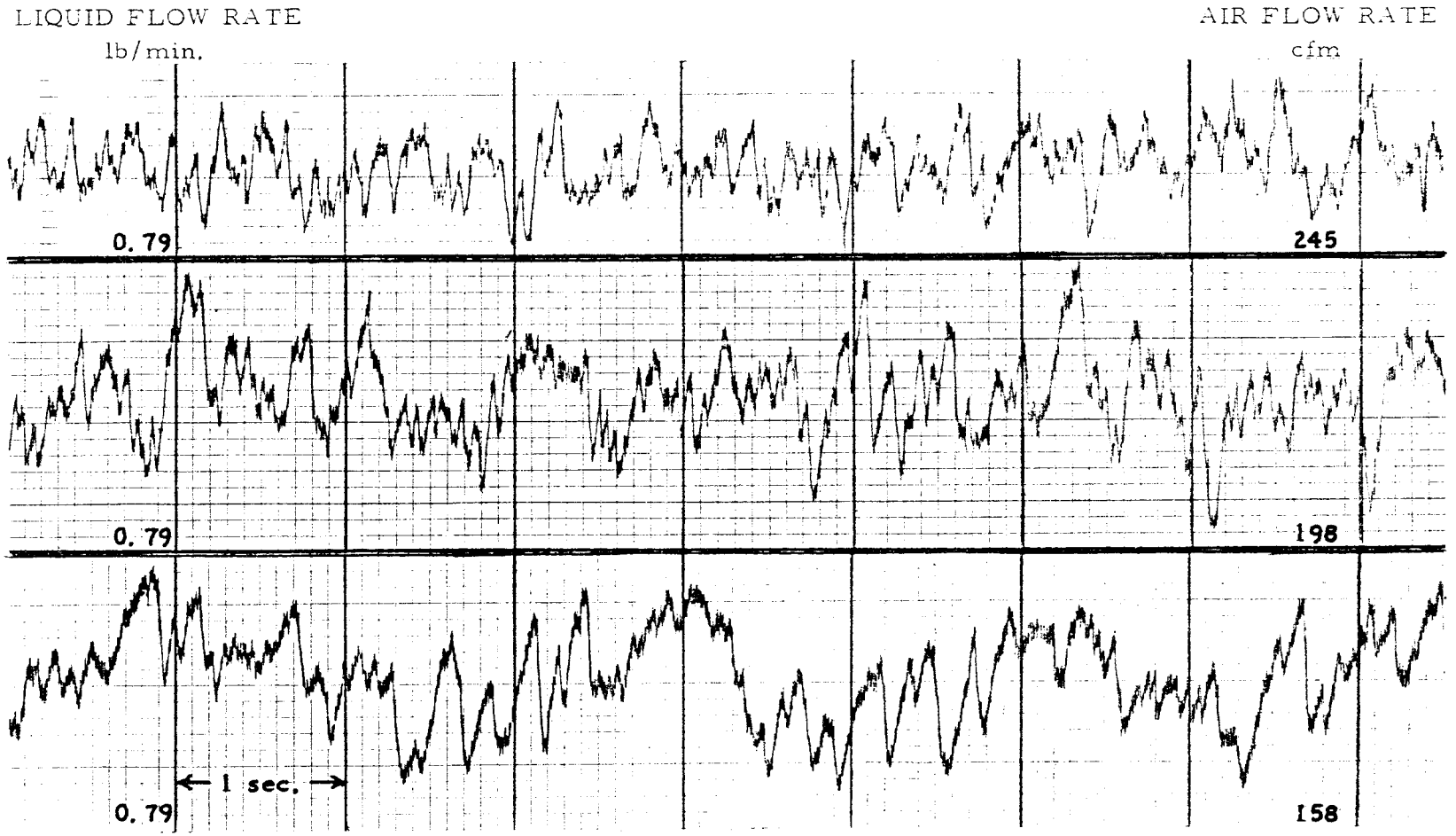

Figure (18) Fluctuations in the Rate of Mass Transfer at the Solid-Liquid Film Interface

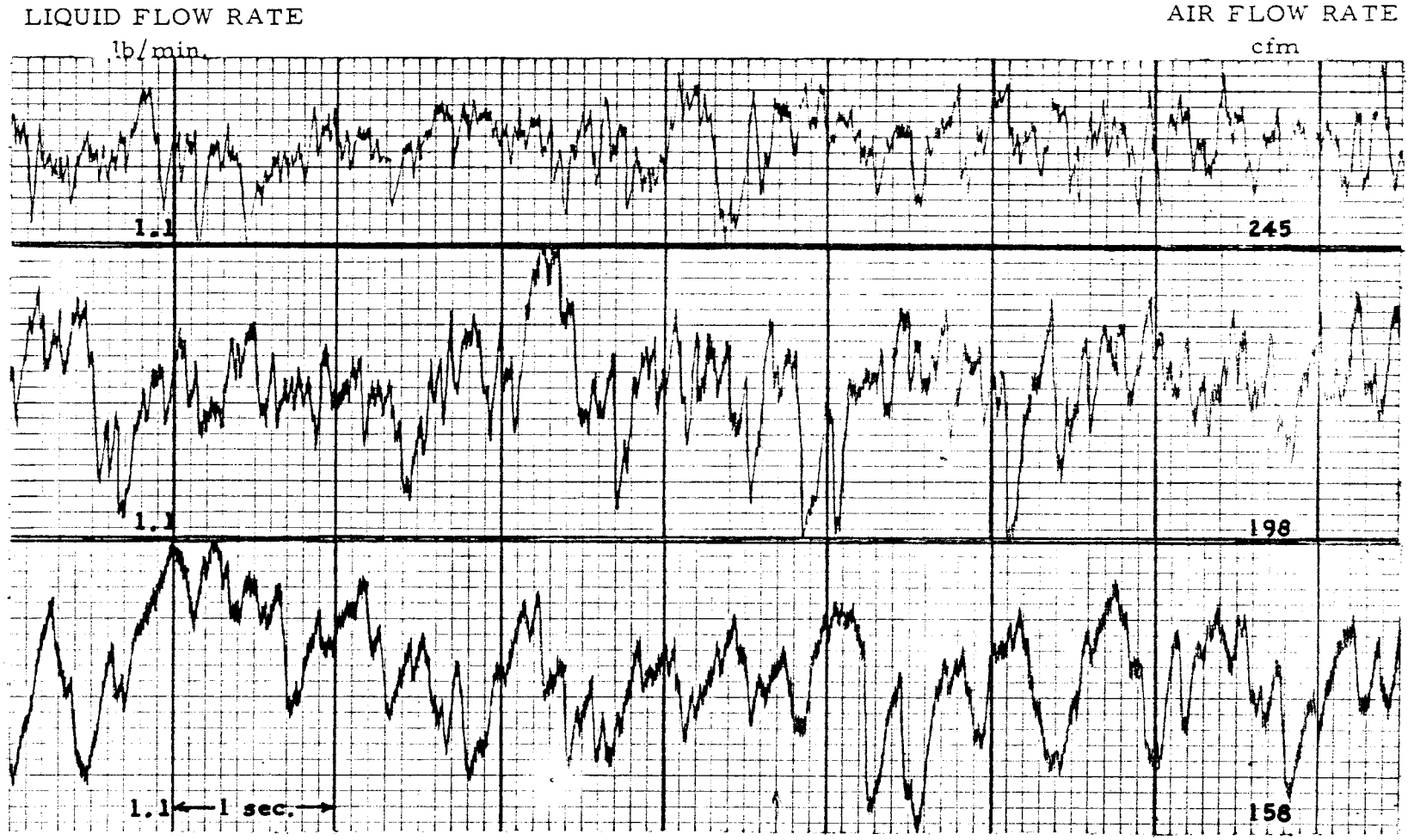

Figure (19) Fluctuations in the Rate of Mass Transfer at the Solid-Liquid Film Interface

in Figures 17-19. The frequencies of the fluctuations are mostly in the 0.2-100 cps range although a power spectrum density analysis is required to describe in detail the frequency domain of the signals. For the liquid flow rates studied, the intensity of the fluctuations increases as the gas flow rate is decreased. At downflow conditions the fluctuations increase considerably indicating a transition in the flow field near the electrode. For the same gas flow rate the film is more stable at low liquid flow rates than at high liquid flow rates. Since more momentum transfer from the air stream is required to maintain high liquid flow films, this result is to be expected.

The present data indicate that mass transfer at the solid-liquid wall may be influenced by the wave structure of the climbing film. The visicorder traces for downflow reflect to a considerable degree the observed pulse-like nature of the climbing film under downflow conditions. Further instantaneous local measurements are required: (1) to study the quantitative effect of the air-liquid interface on the rate of mass transfer to the inner wall, and (2) to classify flow regimes which occur in climbing film flow.

Comparison of Velocity Gradients

A comparison of the velocity gradients at the solid-liquid film interface calculated from experimental mass transfer data of the 1/16-inch and 1/8-inch electrodes for the same air and liquid flow

rates is presented in Table I. As explained in the theory section if the ratio $\bar{c}_1/\bar{c}_2$ is approximately 1.0, all mass transfer measurements are assumed to occur within a laminar region close to the inner wall. The comparison between $\bar{c}_1$ and $\bar{c}_2$ is reasonably good and well within experimental error. Since $\bar{c}_1/\bar{c}_2$ is dependent on $(D_2/D_1)^2 (\bar{k}_{c_1}/\bar{k}_{c_2})^3$ a small error in the values of $\bar{k}_c$ and D could cause a large error in the calculated value of $\bar{c}_1/\bar{c}_2$. To further ensure that all mass transfer does occur within a laminar flow region near the wall, only the experimental data of the 1/16-inch electrode were used to calculate other quantities based on the Leveque model.

Based on the classical film model ($\delta = D/\bar{k}_c$), the concentration boundary layer thickness was determined from mass transfer coefficient data for the 1/16-inch electrode. The estimated concentration boundary layer thickness was 4 to 9% of the experimental liquid film thickness for liquid flows of 0.48 to 0.79 lb/min and gas flows of 198 to 379 cfm.

Table I. Comparison of Velocity Gradients.

Liq. Flow	Air Flow	$\bar{k}_{c_1} \times 10^3$	T_{f_1}	$D_1 \times 10^6$	$\bar{k}_{c_2} \times 10^3$	T_{f_2}	$D_2 \times 10^6$	$\bar{c}_1/\bar{c}_2$
lb/min	cfm	cm/sec	°F	cm^2/sec	cm/sec	°F	cm^2/sec	
0.34	152	2.42	62.9	4.30	1.80	61.8	4.23	1.16
	158	2.36	62.5	4.27	1.87	62.0	4.25	0.99
	172	2.79	62.9	4.30	2.10	62.2	4.25	1.14
	198	3.86	63.3	4.31	2.70	62.6	4.27	1.42
	245	4.74	61.8	4.23	3.66	63.2	4.32	1.12
	309	6.36	66.4	4.52	4.42	65.2	4.45	1.42
	370	7.58	68.9	4.68	5.12	68.0	4.63	1.57
0.48	157	2.44	62.6	4.27	1.80	62.2	4.25	1.22
	172	2.74	63.3	4.32	1.80	61.5	4.21	1.66
	198	3.89	63.4	4.32	2.60	59.7	4.10	1.48
	245	4.84	62.0	4.25	3.43	61.1	4.19	1.36
	309	6.20	63.4	4.32	4.24	61.4	4.21	1.47
	369	7.74	69.9	4.75	4.90	65.0	4.43	1.70
0.79	158	2.41	61.2	4.19	1.87	61.0	4.18	1.06
	172	2.80	61.6	4.22	2.02	61.2	4.19	1.30
	198	4.02	64.0	4.36	2.80	61.5	4.21	1.37
	245	5.20	63.5	4.34	3.52	62.4	4.27	1.54
	309	6.33	63.8	4.35	4.30	61.7	4.22	1.48
	372	7.74	70.6	4.80	4.96	66.0	4.50	1.65
1.10	158	2.60	64.4	4.39	1.98	61.7	4.22	1.04
	172	2.93	62.4	4.27	2.14	62.0	4.25	1.26
	245	5.27	63.6	4.34	3.73	63.2	4.32	1.38
	309	6.49	64.6	4.40	4.63	64.2	4.37	1.34
	370	8.01	70.9	4.83	5.35	67.0	4.56	1.48
1.30	172	3.13	63.0	4.30	2.35	63.0	4.30	1.17
	197	4.29	63.5	4.34	3.01	63.8	4.35	1.44
	245	5.47	64.0	4.36	4.14	63.9	4.35	1.14
	372	8.04	71.2	4.85	5.61	67.7	4.60	1.31

$L_1 = 0.0625$ inch, $L_2 = 0.126$ inch

$$\frac{\bar{c}_1}{\bar{c}_2} = 0.496 \left(\frac{D_2}{D_1} \right)^2 \left(\frac{k_{c_1}}{k_{c_2}} \right)^3$$

Shear Stress at the Inner Wall

The shear stress at the solid-liquid interface (τ_1) was calculated from Equation 29 by means of experimental mass transfer data for the 1/16-inch electrode. In Figure 20, τ_1 is presented as a function of gas flow rate with liquid flow rate as parameter and exhibits a character similar to $\bar{k}_c$ in Figures 14 and 15.

The minimum value of τ_1 in Figure 20 corresponds to incipient downflow within the film even though τ_1 is not zero. Since $\bar{k}_c$ is finite at downflow, the Leveque theory does not predict a zero value for τ_1. Also, since $\bar{k}_c$ is always positive, only positive τ_1 values are predicted. Nevertheless, the minimum value of τ_1 indicates a transition in the velocity gradient at the wall. The limitations of the Leveque theory do not affect the prediction of incipient downflow as far as the liquid and gas flow rates are concerned. For gas flow rates less than 180 cfm, shear stresses were obtained by extrapolation to zero as shown in Figure 21. The accuracy of τ_1 is estimated within ±15%.

Values of τ_1 were also calculated from Equations 19 and 20. Film thicknesses, shear stresses at the outer wall, and radii of maximum air velocity obtained by Kim (45) were used with pressure gradients from the present work. These results are also presented in Figure 20 and compare within 25 to 60% of those obtained

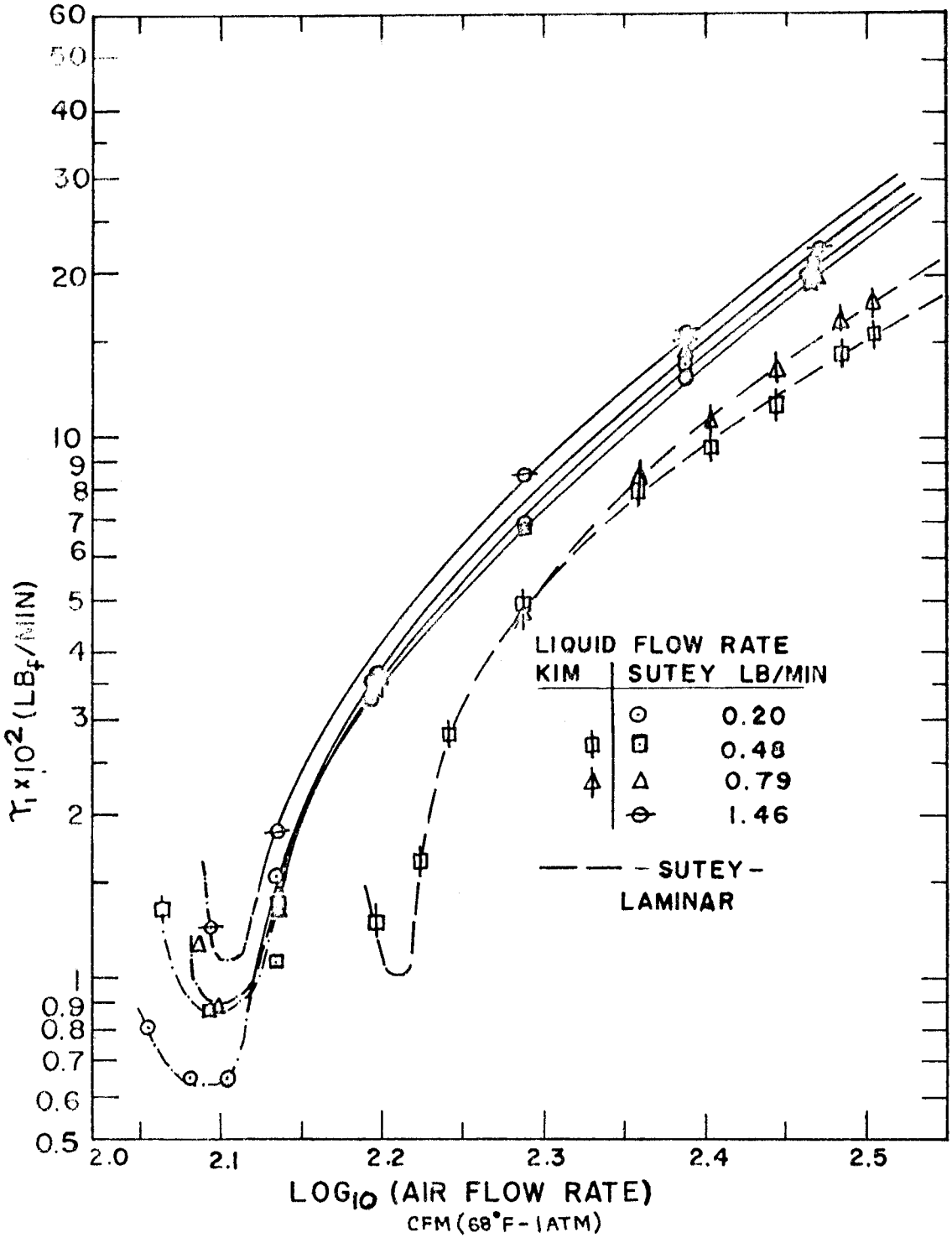

Figure (20) Shear Stress at the Solid-Liquid Film Interface

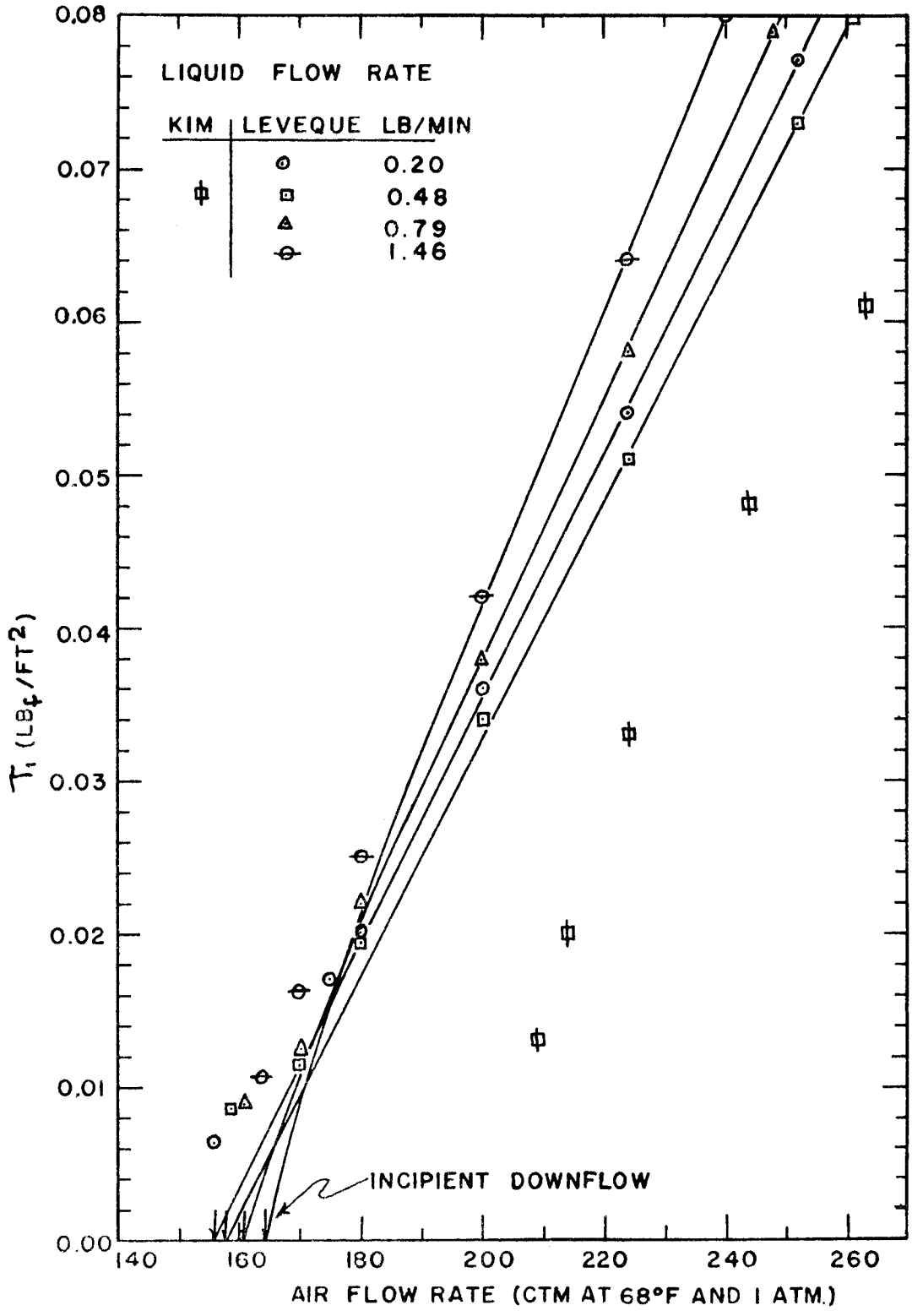

Figure (21) Shear Stress at the Solid-Liquid Film Interface at Downflow

using $\bar{k}_c$ data. Shear stress values calculated from $\bar{k}_c$ data are considered most reliable. Figure 21 shows that values of τ_l obtained from $\bar{k}_c$ data approach the proper downflow limit of zero shear stress, whereas, those obtained using the data of Kim (45) and Equation 19 do not. The discrepancy between τ_l values predicted by the two sets of data is attributed primarily to errors in mean film thickness reported by Kim. Values of τ_l are also presented in Table IX in Appendix J. The experimental data of Kim used in the present work are presented in Appendices J and K.

Pressure Gradient and Entrainment

Pressure gradients are presented in Figures 22 and 23 as a function of air flow rate with liquid flow rate as parameter. Data are presented at equilibrium entrainment conditions in Figure 22 and for minimum entrainment conditions in Figure 23. Additional data is available in Table VIII in Appendix I. Comparison of the data shows that entrainment increases at low air flow rates as downflow and flooding is approached especially at high liquid flow rates. Entrainment reaches a minimum in the moderate gas flow range. Except at very low air flow rates the effect of entrainment on the pressure gradient is negligible for the flow rates studied.

Figures 22 and 23 show that pressure gradient decreases rapidly as the air flow rate decreases at constant liquid flow rate.

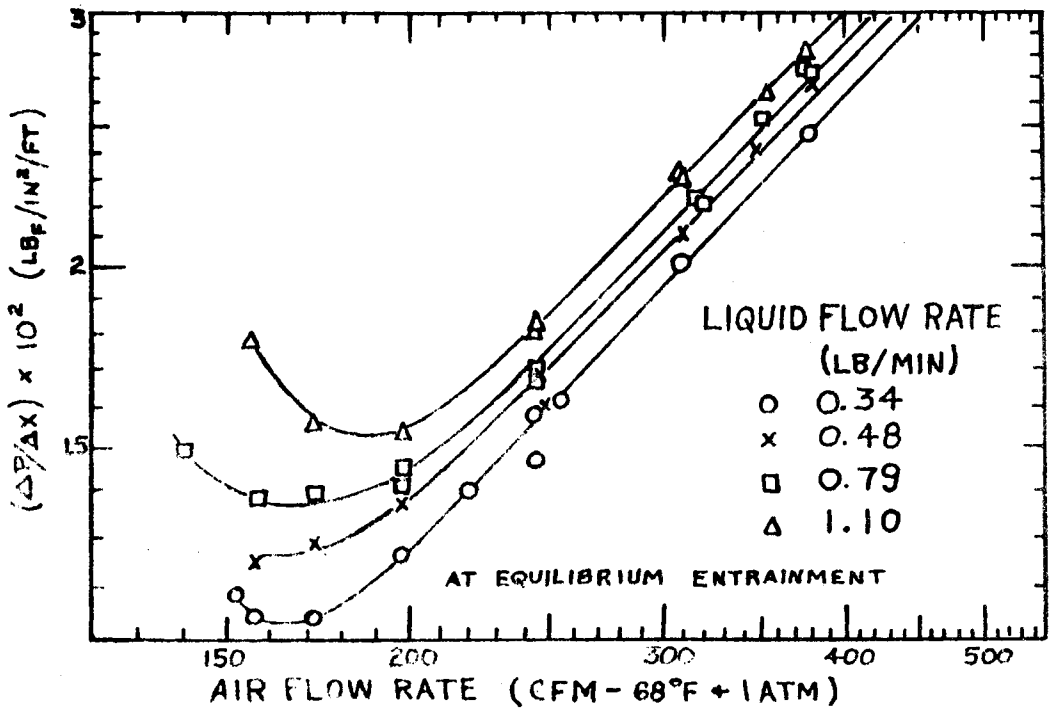

Figure (22) Pressure Gradient vs. Air Flow Rate at Equilibrium Entrainment

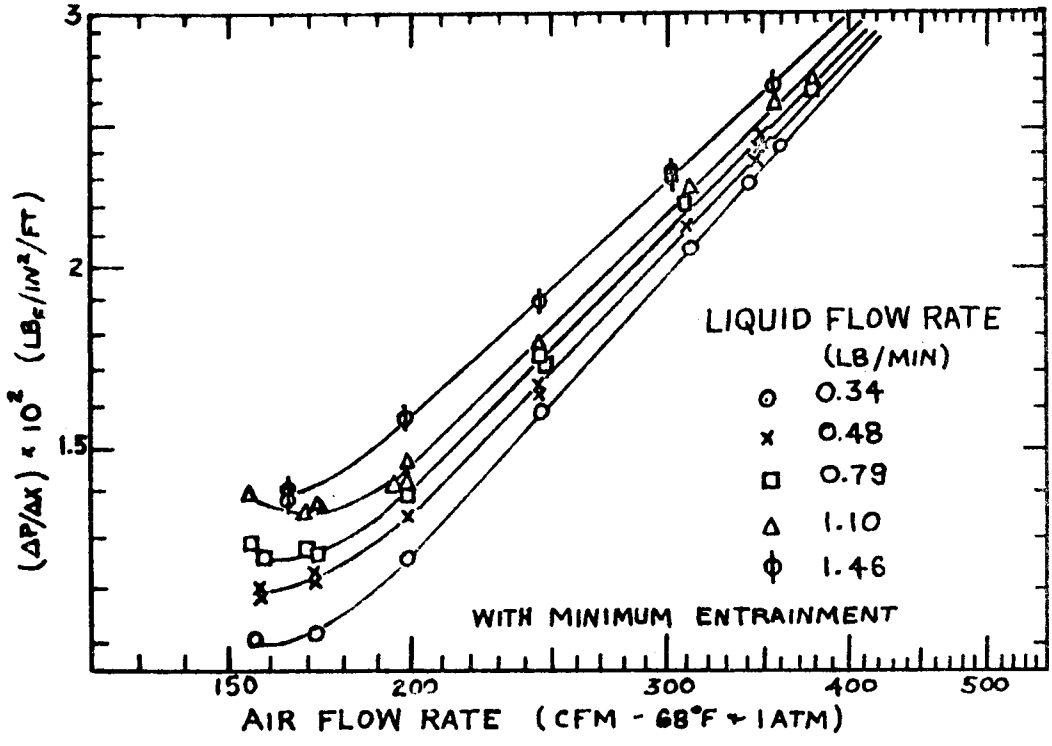

Figure (23) Pressure Gradient vs. Air Flow Rate at Minimum Entrainment

However, at very low air flow rates the pressure gradient reaches a minimum value which closely corresponds in terms of air and liquid flow rates to incipient downflow as shown by $\bar{k}_c$ data in Figures 14 and 15. Under downflow conditions the air-liquid interface is very rough and unstable requiring more energy to be transferred from the air to maintain the climbing film. Thus, the pressure gradient increases as flooding is approached.

Shear Stress at the Air-Liquid Interface

The shear stress (τ_i) at the air-liquid film interface was calculated from Equation 19 using τ_l and α values determined in the present study and mean film thickness data of Kim (45).

In Figure 24 τ_i is presented as a function of gas flow rate with liquid flow rate as parameter. The interfacial shear stress decreases as gas flow rate decreases. For a liquid flow rate of 0.48 lb/min for which film thickness data is available, τ_i exhibits a minimum value at a gas flow rate of 224 cfm, whereas, downflow occurs at 158 cfm based on $\bar{k}_c$ data. This behavior of τ_i may initiate the gradual change of the velocity gradient at the inner wall from positive to negative. Further study in light of additional film thickness data is required to explain the behavior of τ_i.

Values of τ_i were also calculated from Equation 20. Film thicknesses, shear stresses at the outer wall, and radii of maximum

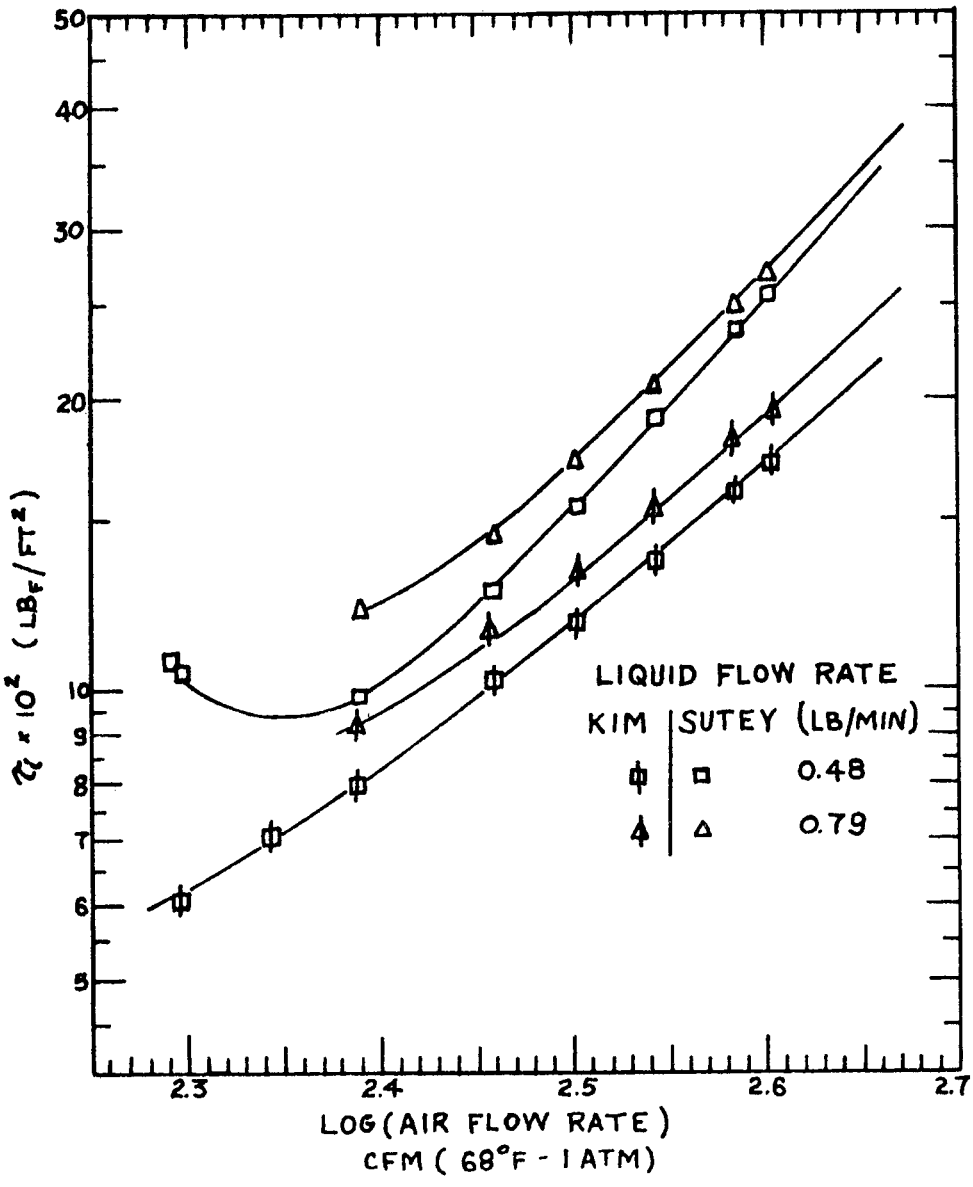

Figure (24) Interfacial Shear Stress vs. Air Flow Rate

air velocity obtained by Kim (45) were used. These results are also presented in Figure 24 and compare within 20 to 40% of those obtained using $\bar{k}_c$ and α data.

DISCUSSION OF RESULTS

Mass Transfer Coefficients at the Solid-Liquid Film Interface

As shown by Figures 13-15 the mass transfer data of the two electrodes are in qualitative agreement. However, the data of the 1/16-inch electrode are more extensive than those of the 1/8-inch electrode; hence, reference will be made primarily to the data of the shorter electrode.

Figures 14 and 15 show the dependence of $\bar{k}_c$ on gas flow rate. The mass transfer coefficient decreases rapidly as the air flow rate is decreased at constant liquid flow rate. As the gas flow rate decreases the film thickness increases, and the film velocity decreases; thus, $\bar{k}_c$ decreases. At very low gas flow rates $\bar{k}_c$ exhibits a minimum value which corresponds to incipient downflow within the film. Although the shear stress at the inner wall is zero at incipient downflow, $\bar{k}_c$ has a finite value. Since the film is very agitated at this point, $\bar{k}_c$ is probably much greater than it would be under stagnant conditions. As flooding is approached $\bar{k}_c$ increases slightly due to increased downflow and agitation within the film.

Figure 16 shows the effect of liquid flow rate on $\bar{k}_c$. Except for the lowest gas flow case, the nature of the relationship between $\bar{k}_c$ and liquid flow is qualitatively the same regardless of gas flow

rate. The mass transfer coefficient decreases slightly as liquid flow rate is decreased. At low liquid flow rates, $\bar{k}_c$ increases sharply just before the minimum wetting rate is reached. The rise in $\bar{k}_c$ just prior to the minimum wetting rate is caused not only by a decrease in film thickness but also by turbulence developed in the film during the groping and reforming periods. A similar rise in heat transfer coefficient near the minimum wetting rate region was measured by Norman and McIntyre (57) for a falling liquid film on a vertical surface.

The lowest gas flow rate in Figure 16 corresponds to the downflow region. In this low film velocity region the film tends to maintain its identity at lower liquid rates and the minimum wetting rate is lowered. Therefore, no rise in $\bar{k}_c$ was noted in the low liquid flow range.

A comparison of Figures 14 and 16 shows the mass transfer coefficient is much more dependent on air flow rate than on liquid flow rate. This is because film velocity, film thickness and film stability are more dependent on the gas flow rate.

The Nature of the Climbing Film Flow

The instantaneous local measurements of mass transfer at the solid-liquid interface are valuable to better understand the nature of climbing film flows. In their studies of electrochemical mass

transfer to a small electrode on a pipe wall, Reiss and Hanratty (62) recorded no fluctuations in the rate of mass transfer to the electrode in the laminar flow regime. At a Reynolds number of 2,140 a slight wavy disturbance was noted. These disturbances increased in the transition region and were observed to greatly increase in frequency and intensity as the Reynolds number further increased to fully developed turbulent flow conditions. Based on these observations of Reiss and Hanratty and the visicorder traces in Figures 17-19, the climbing film flow is considered turbulent for the gas and liquid flows studied. The climbing film is relatively stable at high gas flow rates but becomes increasingly turbulent as the gas flow rate is decreased at a constant liquid flow rate. Turbulence is more characteristic of climbing films formed from high liquid flow rates than those formed from low liquid flow rates.

Laminar Film Model

Results of the shear stress at the inner wall predicted by the laminar film model are presented in Figure 20. The results of this model are the same as those predicted by Equations 19 and 20 using film thicknesses, shear stresses at the outer wall, and radii of maximum air velocity obtained by Kim (45) and pressure gradients from the present work. These results compare within 25 to 60% of those obtained using $\bar{k}_c$ data.

The good agreement between shear stresses calculated from experimental data and those predicted by the laminar film model does not imply that climbing film flow is laminar. On the contrary, instantaneous measurements of the rate of mass transfer to a wire electrode, Figures 17-19, show climbing film flow has a fluctuating character. Since the intensity of the fluctuations decreases at high gas rates, the laminar film model is most applicable in this region for obtaining velocity distributions. Since the shear stress relationship derived from the laminar film model reduces to a force balance on the system, the merit of this model is that it reduces to the proper limits when considering shear stress distribution. This is more than can be said for more complex models. Additional film thickness data is required over a wider range of liquid and gas flow rates to further test the laminar-film model.

Downflow

Under downflow conditions flow adjacent to the inner wall is downward even though the net flow of the film may be upward. At incipient downflow the shear stress at the inner wall is zero. The air and liquid flow conditions at incipient downflow are estimated at the minimum values of the mass transfer coefficient and pressure gradient. These values are presented in Table II and show excellent agreement with each other. Table II shows that incipient downflow

occurs at progressively higher air flow rates as the liquid flow rate increases since more momentum transfer from the air is required to maintain the higher liquid film flows. Predictions of incipient downflow by means of local mass transfer coefficient data are considered the most reliable and do not depend on subjective visual observations of the film.

Downflow may also be measured by the occurrence of high intensity fluctuations in the local instantaneous rate of mass transfer to a wire electrode as shown in Figures 17-19. However, insufficient data is presently available over a wide range of liquid flows to use this method.

As shown in Table II the laminar-film model predicts the air flow at which downflow occurs within 21% of that measured for a liquid flow rate of 0.48 lb/min. Since the laminar-film model reduces to a momentum balance equation (Equation 19) its prediction of incipient downflow is the same as that of Kim (45) as shown in Figure 20.

Downflow was also observed by Willis (72) and Hewitt, et al. (39) in upward annular air-water flow in a vertical tube. Curves of pressure gradient versus gas flow rate at constant liquid flow exhibited minimum values which corresponded to zero wall shear stress. Fair agreement was obtained between measured minimum pressure gradients and those predicted using laminar film flow theory.

Table II. Downflow Conditions.

Liquid Flow Rate lb/min	$\bar{k}_c$	$\Delta P/\Delta x$ Minimum Entrainment	$\Delta P/\Delta x$ Equilibrium Entrainment	τ_1 Levegue Theory	τ_1 Laminar Film Kim-Knudsen
	Air Flow Rate (cfm) - at 68°F and 1 atm				
0.20	156			156	
0.34	157	158	165	157	
0.48	158	158	160	158	202
0.79	161	164	168	161	
1.10	163	172	185	163	
1.30	164	170		164	
1.46	164			164	

Shear Distribution Within the Climbing Film

The shear distribution within the film is described by Figure 25 in which the ratio of the interfacial shear to the shear stress at the inner wall is presented. At very low gas rates τ_i/τ_1, approaches infinity as downflow is approached. At high gas rates this ratio becomes independent of liquid flow rate and approaches unity; i.e. the shear stress is constant across the film. Shearer and Nedderman (67) have also reported $\tau_w = \tau_i$ (to a 1% accuracy) for the small ripple wave regime in annular climbing-film flow. Additional film structure data is required to study the shear stress distribution over a wide range of liquid and gas flow conditions.

The variation of τ_i/τ_1 with flow conditions, Figure 25, is closely related to that of mean film thickness with flow conditions

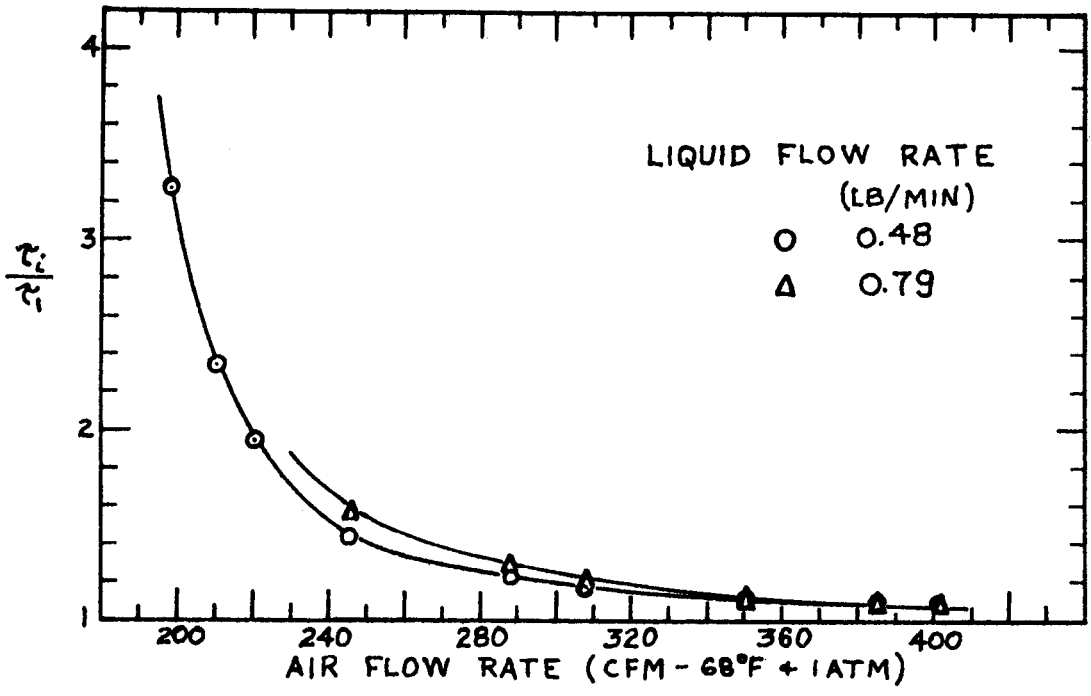

Figure (25) Shear Stress Distribution vs. Air Flow Rate

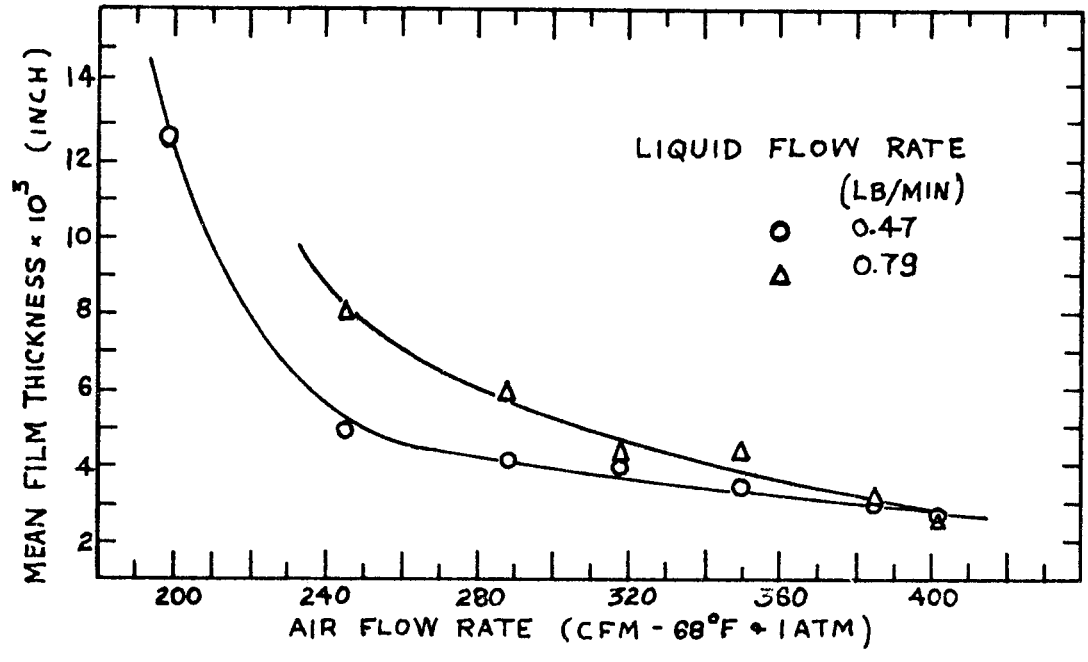

Figure (26) Film Thickness vs. Air Flow Rate

as shown in Figure 26. At very low gas rates the film thickness approaches infinity as downflow and flooding is approached. As the gas flow rate increases the film thickness decreases rapidly up to a flow rate of 240 cfm after which it decreases more slowly becoming nearly independent of liquid flow rate at the highest air flow studied. The similar behavior of τ_i/τ_1 and film thickness with flow conditions demonstrates the dependence of the velocity profile on film thickness.

The results of this study indicate the variation in the velocity profile of the climbing film as a function of air and liquid flow rates. The possible velocity profiles in the liquid film are shown in Figure 27 in the order of increasing gas flow rate.

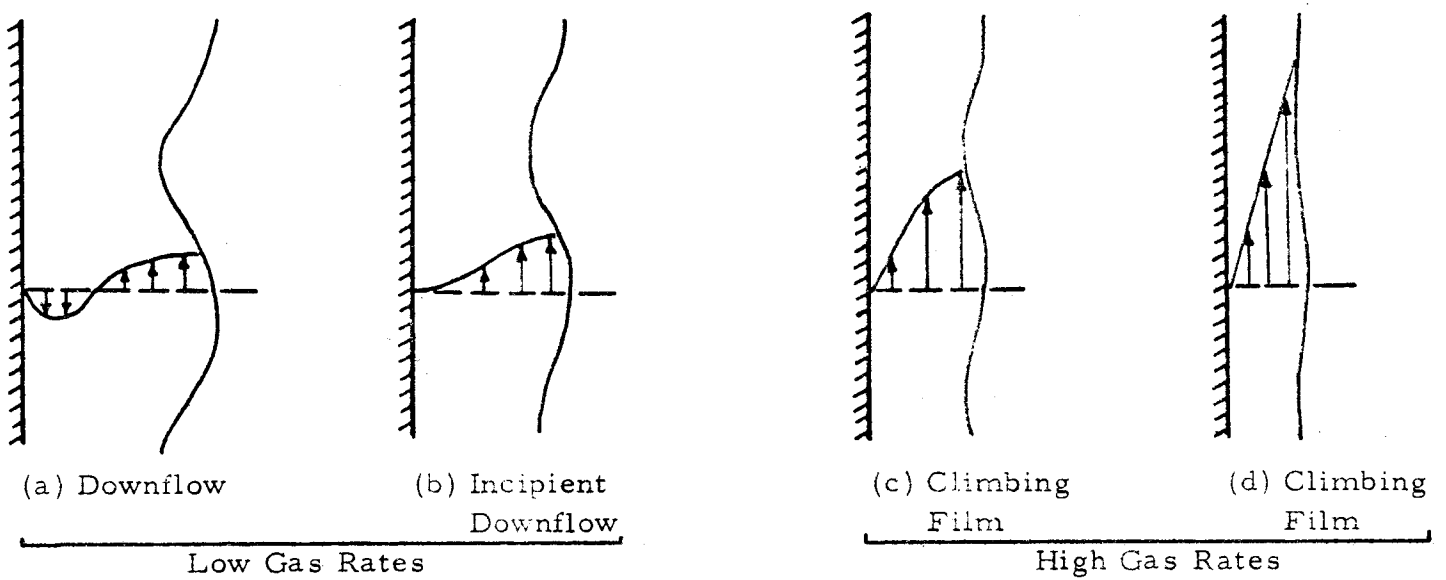

Figure (27) Possible Velocity Profiles of the Climbing Film

CONCLUSIONS

1. Mass transfer coefficients at the solid-liquid film interface in climbing film flow were obtained using a diffusion controlled electrochemical reaction. Experimental results are estimated to be accurate within ± 5%.

2. At constant liquid flow rate the mass transfer coefficient decreases rapidly as air flow rate decreases. As the gas flow decreases the film thickness increases, and the film velocity decreases; thus, $\bar{k}_c$ decreases. At very low gas flow rates $\bar{k}_c$ exhibits a minimum value which corresponds to incipient downflow within the climbing film.

3. At constant gas flow rate the mass transfer coefficient decreases slightly as liquid flow rate is decreased. At very low liquid flow rates, $\bar{k}_c$ increases sharply just prior to the minimum wetting rate. The increase is caused not only by a decrease in film thickness but also by turbulence developed in the film during the groping and reforming periods.

4. Based on the measurements of fluctuations in the rate of mass transfer to a pipe wall by Reiss and Hanratty (62) and the measurements obtained in this work, the climbing film flow is considered turbulent for the gas and liquid flows studied. The climbing film is relatively stable at high gas flow rates but becomes increasingly turbulent as downflow is approached. Turbulence is more

characteristic of climbing films formed from high liquid flow rates than those formed from low liquid flow rates.

5. The shear stress at the inner wall was calculated from the Leveque Theory for climbing film flow using experimental mass transfer data of a short electrode. Results compare well (25 to 60%) with values calculated from film thicknesses, shear stresses at the outer wall and radii of maximum air velocity obtained by Kim (45). Shear stress values calculated from $\bar{k}_c$ values approach the proper downflow limit of zero.

6. The pressure gradient decreases rapidly as the air flow rate decreases at constant liquid flow rate. At very low air flow rates the pressure gradient reaches a minimum value which closely corresponds in terms of air and liquid flow rates to incipient downflow as indicated by the mass transfer coefficient data. Except for very low air flow rates the effect of entrainment on the pressure gradient was negligible for the flow rates studied.

7. Interfacial shear stresses were calculated from two separate relationships each using independent experimental data. The results agree to within 20 to 40%. For a liquid flow rate of 0.48 lb/min for which film thickness data are available, τ_i exhibits a minimum value at a gas flow rate of 224 cfm, whereas, downflow occurs at 158 cfm. This behavior of τ_i may initiate the gradual change of the velocity gradient at the inner wall from positive to

negative. Further study in light of additional film thickness data is required to explain the nature of τ_i.

8. The laminar-film model predicts shear stresses at the inner wall within 25 to 60% and flow conditions at downflow within 21% of those obtained using $\bar{k}_c$ data. However, the good agreement of these results does not imply that climbing film flow is laminar. Since the shear stress relationship derived from the laminar-film model reduces to a force balance on the system, these results indicate that the laminar film model reduces to the proper limits.

9. At very low gas rates the shear stress ratio τ_i/τ_l approaches infinity as downflow is approached. At high gas rates this ratio becomes independent of liquid flow rate and approaches unity; i.e. the shear stress is constant across the film. The similar behavior of τ_i/τ_l and film thickness as affected by flow conditions demonstrates the dependence of the velocity profile on film thickness.

RECOMMENDATIONS FOR FURTHER STUDY

1. Of primary importance is the need for accurate instantaneous film thickness and wave structure data over a wide range of liquid and gas flow rates in climbing film flow. Analysis of the film by means of high speed photography should provide insight to better understand the nature of wave motion and entrainment. Such data is necessary to test the validity of proposed theoretical models, and to predict shear stresses at the various interfaces and at various liquid film flow rates.

2. Further instantaneous local measurements of mass transfer to a wire electrode mounted flush to the inner core wall are required: (1) to study (using high speed photography) the effect of the air-liquid interface on the rate of mass transfer to the inner wall, and (2) to classify flow regimes which occur in climbing film flow. A power density spectrum analysis is required to describe in detail the frequency domain of the fluctuating signals representing the instantaneous mass transfer coefficient. Such a distribution may be compared with similar results in pipe flow. The electrochemical mass transfer method may also be extended to measure turbulence in the flow field near the inner wall.

3. Both average and instantaneous mass transfer coefficients in climbing film flow should be studied as a function of distance from

the liquid entrance. Such a study would describe the film stability and flow transitions of the film as it flows upward in the column.

4. A study of convective heat transfer from the inner wall to the climbing film is required. Results of such a study may be compared with the mass transfer results of the present work. This should eventually be extended to boiling heat transfer in climbing film flow.

5. On the basis of fluctuating mass transfer data of the present study, the surface renewal models (13, 30, 42, 70) are considered as possible explanations of the exchange of heat, mass, and momentum transfer from the climbing film to the inner wall. Surface renewal parameters may be determined from the mass transfer results of this work and used to predict preferably heat transfer results for the climbing film system.

6. Further work is desirable on liquid entrainment--deposition of spray and re-entrainment--with particular attention paid to the equilibrium effects. Entrainment data is highly essential to predict the average density of the gas core and to explain the momentum, mass, and heat transfer processes occurring in climbing film flow. Liquid entrainment should be studied in the light of film stability and interfacial film structure.

7. To extend the results of the present work to two-phase gas-liquid systems in general, the effects of viscosity, density, and

surface tension on the momentum and mass transfer processes within the climbing film must be studied. Mass transfer coefficients, shear stresses, pressure gradients, film thicknesses, and gas velocity profiles should be obtained for various fluids.

BIBLIOGRAPHY

1. Anderson, G. H. and B. F. Mantzouranis. Two-phase (gas-liquid) flow phenomena. Part I. Pressure drop and hold-up for two-phase flow in vertical tubes. Chemical Engineering Science 12:109-126. 1960.

2. _____ Two-phase (gas-liquid) flow phenomena. Part II. Liquid entrainment. Chemical Engineering Science 12:233-242. 1960.

3. Bazan, J. C. and A. J. Arvia. Ionic mass transfer in flowing solutions. Electrochemical reactions under ionic mass-transfer rate control on cylindrical electrodes. Electrochimica Acta 9:667-684. 1964.

4. _____ The diffusion of ferro-ferricyanide ions in aqueous solutions of sodium hydroxide. Electrochimica Acta 10:1025-1032. 1965.

5. Bennett, J. A. and J. D. Thornton. Data on the vertical flow of air-water mixtures in the annular and dispersed flow regimes. Part I. Preliminary study. Transactions of the Institute of Chemical Engineers, London 39:101-112. 1961.

6. Bomben, J. L. and C. W. Tobias. Current distribution in a porous electrode. Berkeley, 1963. 78p. (California. University. Space Science Laboratory. National Aeronautics and Space Administration Research Grant 150-61)

7. Calvert, S. and B. Williams. Upward co-current annular flow of air and water in smooth tubes. Journal of the American Institute of Chemical Engineers 1:78-86. 1955.

8. Chand, R. and H. F. Rosson. Local heat flux to a water film flowing down a vertical surface. Industrial and Engineering Chemistry Fundamentals 4:356-359. 1965.

9. Charlot, G., J. Badoz-Lambling and B. Tremillion. Electrochemical reactions. New York, Elsevier, 1962. 376p.

10. Chenoweth, J. M. and M. W. Martin. Turbulent two-phase flow. Petroleum Refiner 34:151-155. 1955.

11. Collier, J. G. Burnout in liquid cooled reactors. Nuclear Power 6:61-66. 1961.

12. Collier, J. G. and G. F. Hewitt. Data on the vertical flow of air-water mixtures in the annular and dispersed flow regions. Part II. Film thickness and entrainment data and analysis of pressure drop measurements. Transactions of the Institution of Chemical Engineers, London 39:127-136. 1961.

13. Danckwerts, P. V. Significance of liquid-film coefficients in gas absorption. Industrial and Engineering Chemistry 43: 1460-1466. 1951.

14. Deissler, R. G. Analysis of turbulent heat transfer and flow in the entrance of smooth passages. Washington, D. C. 1953. 88p. (U. S. National Advisory Committee for Aeronautics. Technical note 3016)

15. Dukler, A. E. Fluid mechanics and heat transfer in vertical falling film systems. In: Heat transfer by [ ] Storrs. New York, 1960. p. 1-10. (American Institute of Chemical Engineers. Chemical Engineering Progress Symposium series no. 30)

16. Dukler, A. E. and O. P. Bergelin. Characteristics of flow in falling liquid films. Chemical Engineering Progress 48:557-563. 1952.

17. Dukler, A. E. and M. G. Hubbard. The characterization of flow regimes for horizontal two-phase flow: I. Statistical analysis of wall pressure fluctuations. In: Proceedings of the 1966 Heat Transfer and Fluid Mechanics Institute, University of Santa Clara, June, 1966. Stanford, Stanford University Press, 1966. p.100-121.

18. Dukler, A. E., M. Wicks and R. G. Cleveland. Frictional pressure drop in two-phase flow: A. A comparison of existing correlations for pressure drop and holdup. Journal of the American Institute of Chemical Engineers 10:38-43. 1964.

19. _____ Frictional pressure drop in two-phase flow: B. An approach through similarity analysis. Journal of the American Institute of Chemical Engineers 10:44-51. 1964.

20. Eisenberg, M., C. W. Tobias and C. R. Wilke. Ionic mass

transfer and concentration polarization at rotating electrodes. Transactions of the Electrochemical Society 101:306-320. 1954.

21. Fage, A. and H. C. H. Townend. Examination of turbulent flow. Proceedings of the Royal Society London, Ser. A, 135: 656-677. 1932.

22. Faruqui, A. A. and J. G. Knudsen. Rates of heat transfer from short sections of an isothermal pipe. Corvallis, Oregon. 1959. 8p. (Oregon. State University. Engineering Experiment Station. Reprint no. 62)

23. Gill, L. E. and G. F. Hewitt. Further data on the annular flow of air-water mixtures in a 1 1/4-inch bore perspex tube. Harwell, Berkshire, England, 1963. 20p. (United Kingdom Atomic Energy Authority. AERE-R-3935)

24. Gill, L. E., G. F. Hewitt and P. M. C. Lacey. Sampling probe studies of the gas core in annular two-phase flow. Part II. Studies of the effect of phase flow rates on phase and velocity distribution. Harwell, Berkshire, England, 1963. 51p. (United Kingdom Atomic Energy Authority. AERE-R-3955)

25. Glasstone, S. Introduction to electrochemistry. New York, Van Nostrand, 1942. 557p.

26. Govier, G. W., B. A. Radford and J. S. C. Dunn. The upwards vertical flow of air-water mixtures. Part I. Effect of air and water rates on flow pattern, hold-up and pressure drop. Canadian Journal of Chemical Engineering 35: 58-70. 1957.

27. Govier, G. W., and W. L. Short. The upward vertical flow of air-water mixtures. Part II. Effect of tubing diameter on flow pattern, hold-up, and pressure drop. Canadian Journal of Chemical Engineering 36:105-202. 1958.

28. Grassman, P. Electrochemische Messung von Stoffubergangszahlen. Chemie Ingenieur Tecknik 8: 529-533. 1961.

29. Hall-Taylor, N. and G. F. Hewitt. The motion and frequency of large disturbance waves in annular two-phase flow of air-water mixtures. Harwell, Berkshire, England, 1962. 36p. (United Kingdom Atomic Engergy Authority. AERE-R-3952)

30. Hanratty, T. J. Turbulent exchange of mass and momentum with a boundary. Journal of the American Institute of Chemical Engineers 2:359-362. 1956.

31. Hanratty, T. J. and A. Hershman. Initiation of roll waves. Journal of the Institute of Chemical Engineers 7:488-497. 1961.

32. Hewitt, G. F. Analysis of annular two-phase flow: Application of the Dukler analysis to vertical upward flow in a tube. Harwell, Berkshire, England, 1961. 39p. (United Kingdom Atomic Energy Authority. AERE-R-3680)

33. _____ Photographic and entrainment studies in two-phase flow systems. Harwell, Berkshire, England, 1964. 45p. (United Kingdom Atomic Energy Authority. AERE-R-4683)

34. Hewitt, G. F. and J. G. Collier. Film thickness measurements. Harwell, Berkshire, England, 1964. 35p. (United Kingdom Atomic Energy Authority. AERE-R-4684)

35. Hewitt, G. F., K. D. Cooper and B. Pinchin. Photography of two-phase flow. Harwell, Berkshire, England, 1963. 23p. (United Kingdom Atomic Energy Authority. AERE-R-4301)

36. Hewitt, G. F., H. A. Kearsey, P. M. C. Lacey and D. J. Pulling. Burnout and nucleation in climbing film flow. International Journal of Heat and Mass Transfer 8:793-814. 1965.

37. Hewitt, G. F., R. D. King and P. C. Lovegrove. Techniques for liquid film and pressure drop studies in annular two-phase flow. Harwell, Berkshire, England, 1962. 39p. (United Kingdom Atomic Energy Authority. AERE-R-3921)

38. Hewitt, G. F. and P. M. Lacey. The breakdown of the liquid film in annular two-phase flow. International Journal of Heat and Mass Transfer 8:781-791. 1965.

39. Hewitt, G. F., P. M. C. Lacey and B. Nicholls. Transitions in film flow in a vertical tube. Harwell, Berkshire, England, 1965. 35p. (United Kingdom Atomic Energy Authority. AERE-R-4614)

40. Hewitt, G. F. and P. C. Lovegrove. The application of the light absorption technique to continuous film thickness recording in annular two-phase flow. Harwell, Berkshire, England, 1962. 14p. (United Kingdom Atomic Energy Authority. AERE-R-3953)

41. Hewitt, G. F., P. C. Lovegrove and B. Nicholls. Film thickness measurement using a fluorescence technique. Part I. Description of the method. Harwell, Berkshire, England, 1964. 15p. (United Kingdom Atomic Energy Authority. AERE-R-4478)

42. Higbie, R. The rate of absorption of a pure gas into a still liquid during short periods of exposure. Transactions of the American Institute of Chemical Engineers 31: 365-389. 1935.

43. Isbin H. S., C. Sher and K. C. Eddy. Void fractions in two-phase steam-water flow. Journal of the American Institute of Chemical Engineers 3: 136-142. 1957.

44. Kapitza, P. L. Wave flow of thin layers of a viscous liquid. Zhurnal Eksperimentalnov I Teoreticheoskoi Fiziki (Russian) 18: 3-18. 1948.

45. Kim, D. H. Momentum transfer in climbing film flow in an annular duct. Ph.D. thesis. Corvallis, Oregon State University, 1965. 148 numb. leaves.

46. Knudsen, J. G. and D. L. Katz. Fluid dynamics and heat transfer. New York, McGraw-Hill, 1958. 576p.

47. Kolthoff, I. M. and E. A. Pearson. Stability of potassium ferrocyanide solutions. Industrial and Engineering Chemistry, Analytical Edition 3: 381-382. 1931.

48. Lacey, P. M. C., G. F. Hewitt and J. G. Collier. Climbing film flow. In: Symposium on Two-Phase Flow, arranged by the Institution of Mechanical Engineers, London, 1962. Harwell, Berkshire, England, 1962. 22p. (United Kingdom Atomic Energy Authority. AERE-R-3962)

49. Laird, A. D. K. Stability of gas flow in a tube as related to vertical annular gas-liquid flow. Transactions of the American Society of Mechanical Engineers 76: 1005-1010. 1954.

50. Laufer, J. Investigation of turbulent flow in a two-dimensional channel. Washington, D. C., 1951. 30p. (U. S. National Advisory Committee for Aeronautics. Technical report 1053)

51. Lee, J. Turbulent velocity profile of a vertical film flow. Chemical Engineering Science 20: 533-536. 1965.

52. Levich, V. G. Physicochemical hydrodynamics. Englewood Cliffs, N. J., Prentice-Hall, 1962. 700p. (Translated from the Russian)

53. Levy, S. Prediction of two-phase annular flow with liquid entrainment. International Journal of Heat and Mass Transfer 9: 171-188. 1966.

54. Lin, C. S., E. B. Denton, N. S. Gaskill and G. L. Putnam. Diffusion controlled electrode reactions. Industrial and Engineering Chemistry 43: 2136-2143. 1951.

55. Lockhart, R. W. and R. C. Martinelli. Proposed correlation of data for isothermal two-phase, two component flow in pipes. Chemical Engineering Progress 45: 39-48. 1949.

56. Mitchell, J. E. and T. J. Hanratty. A study of turbulence at a wall using an electrochemical wall shear-stress meter. Journal of Fluid Mechanics 26: 199-221. 1966.

57. Norman, W. S. and V. McIntyre. Heat transfer to a liquid film on a vertical surface. Transactions of the Institution of Chemical Engineers, London 38: 301-307. 1960.

58. Ostrach, S. and A. Koestel. Film instabilities in two-phase flows. In: Proceedings of the Sixth National Heat Transfer Conference, American Institute of Chemical Engineers, American Society of Mechanical Engineers, Boston, Massachusetts, Aug. 11-14, 1963. 56p. (American Institute of Chemical Engineers. Preprint no. 45)

59. Petrocelli, J. V. and A. A. Paolucci. Overvoltage at oxidation-reduction electrodes. Journal of the Electrochemical Society 98: 291-295. 1951.

60. Preston, J. H. The determination of turbulent skin friction by means of pitot tubes. Journal of the Royal Aeronautical Society 58: 109-121. 1954.

61. Quandt, E. R. Measurement of some basic parameters in two-phase annular flow. Pittsburg, Pennsylvania, Bettis Atomic Power Laboratory, Westinghouse Electric Corporation, 1962. 35p. (WAPD-T-1502 C AT-11-1 Gen 14)

62. Reiss, L. P. and T. J. Hanratty. Measurement of instantaneous rates of mass transfer to a small sink on a wall. Journal of the American Institute of Chemical Engineers 8:245-247. 1962.

63. _____ An experimental study of the unsteady nature of the viscous sublayer. Journal of the American Institute of Chemical Engineers 9:154-160. 1963.

64. Ruckenstein, E. and C. Berbente. Mass transfer in wave flow. Chemical Engineering Science 20:795-801. 1965.

65. Shaw, P. V. and T. J. Hanratty. Fluctuations in the local rate of turbulent mass transfer to a pipe wall. Journal of the American Institute of Chemical Engineers 10:475-482. 1964.

66. Shaw, P. V., L. P. Reiss and T. J. Hanratty. Rates of turbulent transfer to a pipe wall in the mass transfer region. Journal of the American Institute of Chemical Engineers 9: 362-364. 1963.

67. Shearer, C. J. and R. M. Nedderman. Pressure gradient and liquid film thickness in co-current upwards flow of gas-liquid mixtures. Application to film cooler design. Chemical Engineering Science 20:671-683. 1965.

68. Sleicher, C. A. Experimental velocity and temperature profiles for air in turbulent pipe flow. Transactions of the American Society of Mechanical Engineers 80:693-704. 1958.

69. Sternberg, J. Theory for the viscous sublayer. Journal of Fluid Mechanics 13:241-271. 1962.

70. Toor, H. L. and J. M. Marchello. Film-penetration for mass and heat transfer. Journal of the American Institute of Chemical Engineers 4:97-101. 1958.

71. Whitaker, S. and I. O. Jones. Stability of falling liquid films. Effect of interface and interfacial mass transport. Journal of the American Institute of Chemical Engineers 12:421-431. 1966.

72. Willis, I. J. Upwards annular two-phase air-water flow in vertical tubes. Chemical Engineering Science 20: 895-902. 1965.

APPENDICES

APPENDIX A

CALIBRATION OF THE AIR FLOW ORIFICE

CALIBRATION OF THE AIR FLOW ORIFICE

Since the orifice was calibrated for air at $68^{\circ}F$ and one atm, compensation was made for air flows at temperatures other than $68^{\circ}F$. The following correction was applied to all air flows.

$$\Delta P_1 = (T_1/T_2)\ \Delta P_2$$

where

T_1 = temperature of calibration ($528^{\circ}R$).

T_2 = temperature of air under operating conditions ($^{\circ}R$).

ΔP_1 = pressure reading corresponding to air flow at $68^{\circ}F$.

ΔP_2 = pressure reading corresponding to air flow at T_2.

In this manner ΔP_1 was used to determine the actual air flow in the system by means of Figure 28.

The temperature of the air was measured by a calibrated thermometer located just prior to the entrance to the annular test section. Air temperature control was obtained by regulation of the flow of cooling water through the heat exchanger as shown in Figure 3.

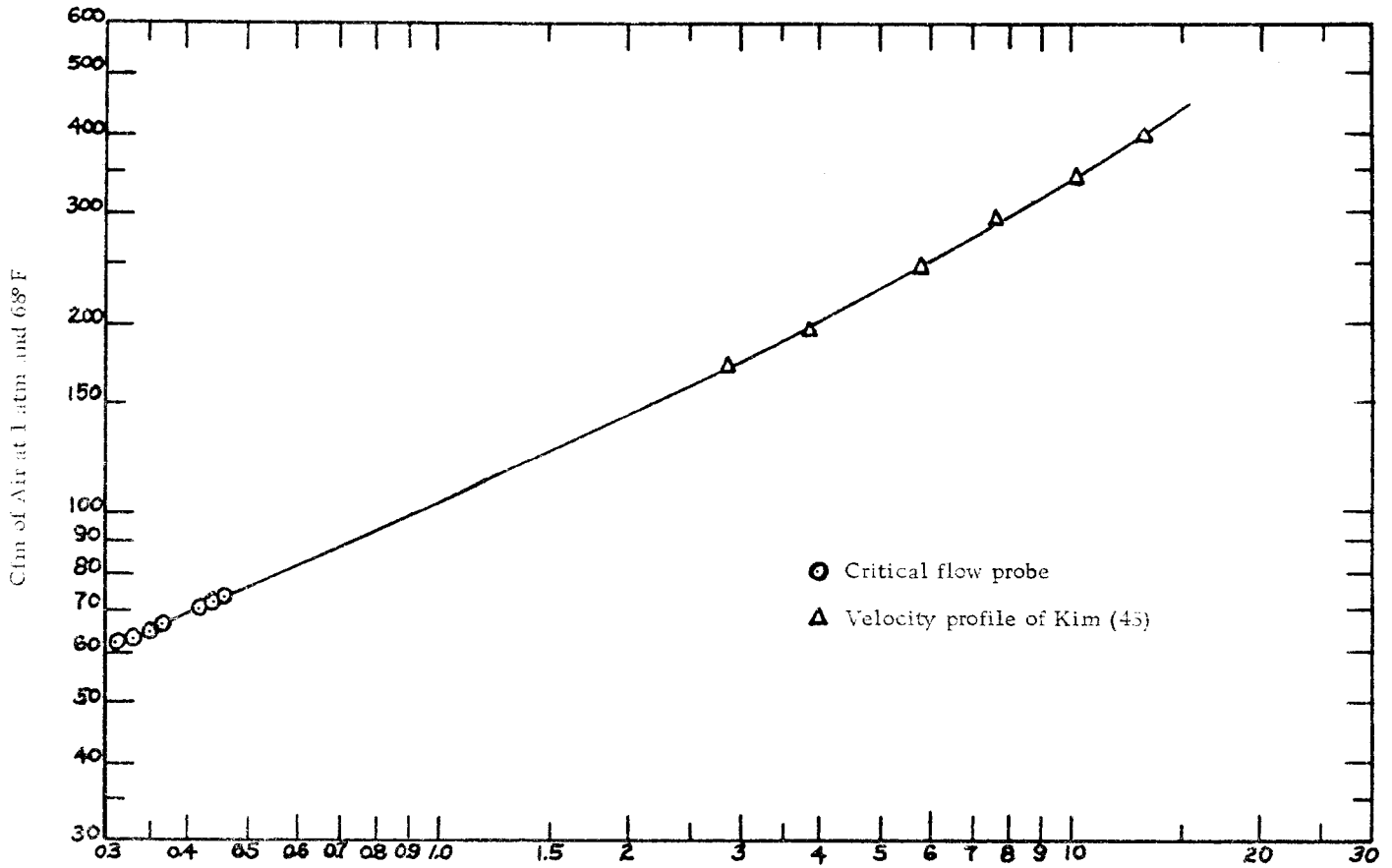

Figure (28) Calibration of Air Flow Orifice

APPENDIX B

PHYSICAL PROPERTIES OF THE ELECTROLYTE

PHYSICAL PROPERTIES OF THE ELECTROLYTE

Specific Gravity

Specific gravities of redox solutions used in this work were measured by means of a "Cenco 16752" hydrometer set. Specific gravity of a 0.025 equimolar solution of potassium ferricyanide and potassium ferrocyanide in 2N sodium hydroxide is presented as a function of temperature in Figure 29. All measurements are estimated to be accurate within ±0.3% and reproducible within ±0.1%.

Viscosity

Viscosities of redox solutions used in this work were measured by means of a calibrated "Cannon-Fenske" (no. 25-J413) viscometer. Viscosity of a 0.025 equimolar solution of potassium ferricyanide and potassium ferrocyande in 2N sodium hydroxide is presented as a function of temperature in Figure 30. All measurements are estimated to be accurate within ±0.5% and reproducible within ±0.2%.

Diffusivity

Diffusivities of ferri- and ferrocyanide ions were obtained from data reported by Bazan and Arvia (4). They studied the diffusion of

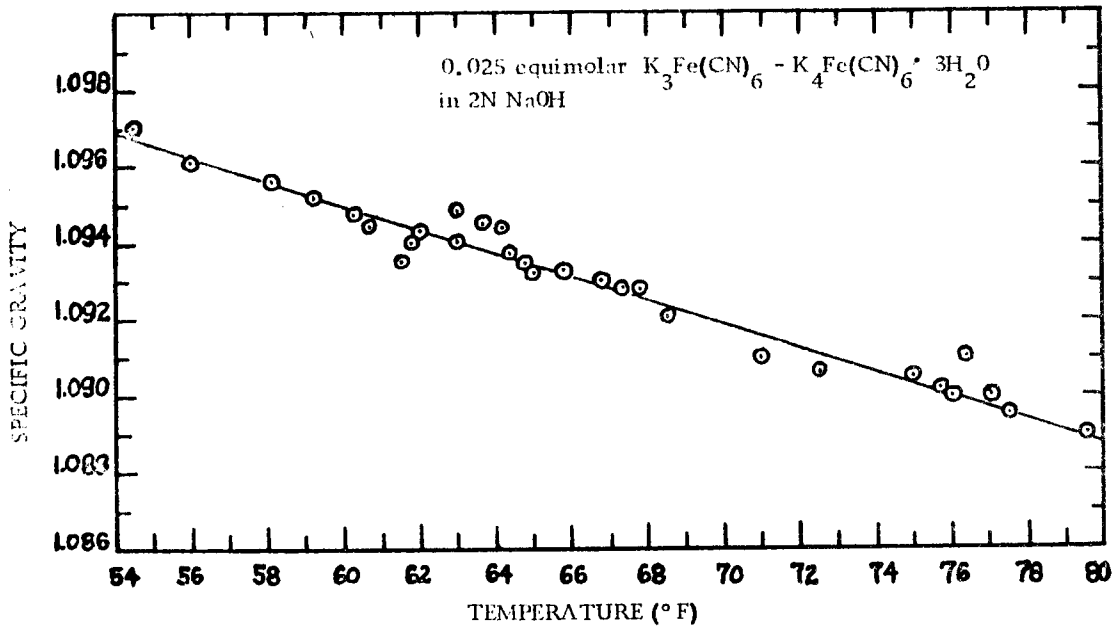

Figure (29) Specific Gravity of Electrolyte

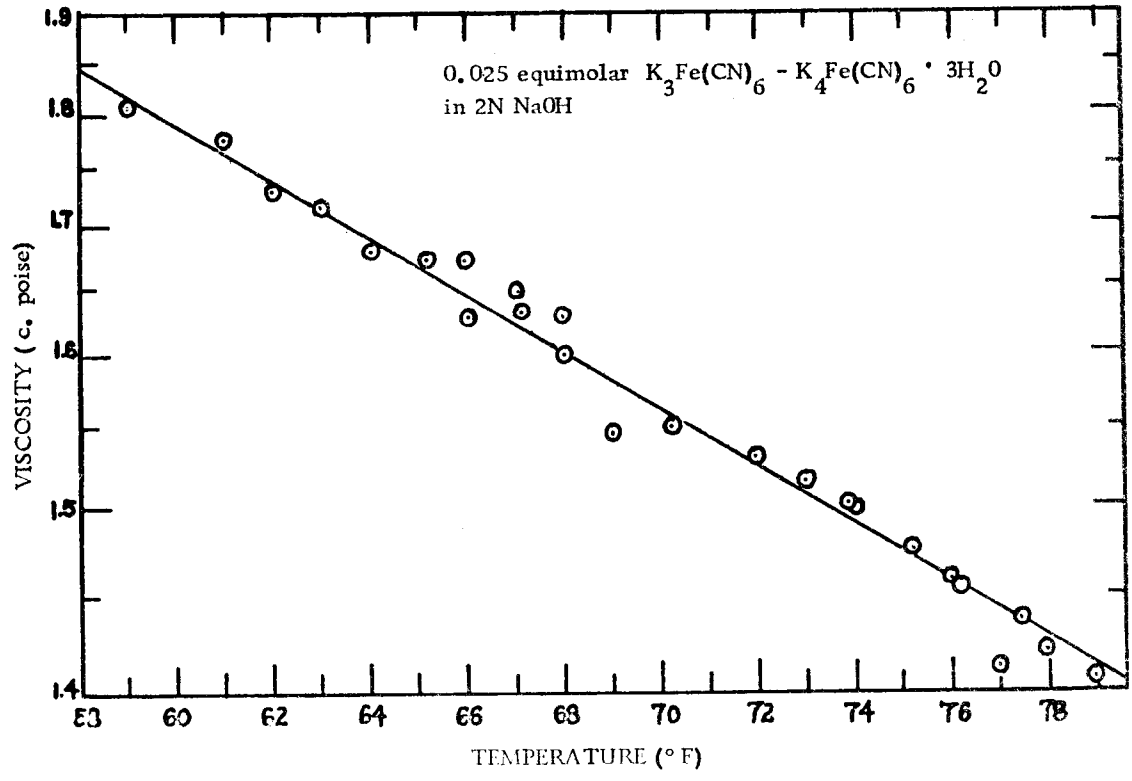

Figure (30) Viscosity of Electrolyte

ferri- and ferrocyanide ions in sodium hydroxide solutions by means of a platinum rotating disk electrode. Results were obtained at variable concentrations in the range of temperature between 24 and 40°C. They presented the following relations for a 0.025 equimolar solution of potassium ferri- and potassium ferrocyanide in 2N sodium hydroxide.

$$\frac{D_{3^\mu}}{T} = (2.54 \pm 0.13)\,x10^{-10}\ \frac{cm^2}{s}\ \frac{poise}{^oK} \qquad \text{(Ferri)}$$

$$\frac{D_{4^\mu}}{T} = (2.09 \pm 0.11)\,x10^{-10}\ \frac{cm^2}{s}\ \frac{poise}{^oK} \qquad \text{(Ferro)}$$

The maximum experimental error affecting the reported diffusivities is approximately 3%. The diffusivity of ferricyanide ion in the solution used in this work is presented in Figure 31.

Comparison of Physical Properties of Water and Electrolyte

In this study the film thickness for 0.025 equimolar potassium ferri-ferrocyanide in 2N NaOH was assumed to be the same as that for water as measured by Kim (45). The physical properties of these fluids are very similar, and thus, no significant error is anticipated. Table III gives a comparison of the physical properties of the two fluids.

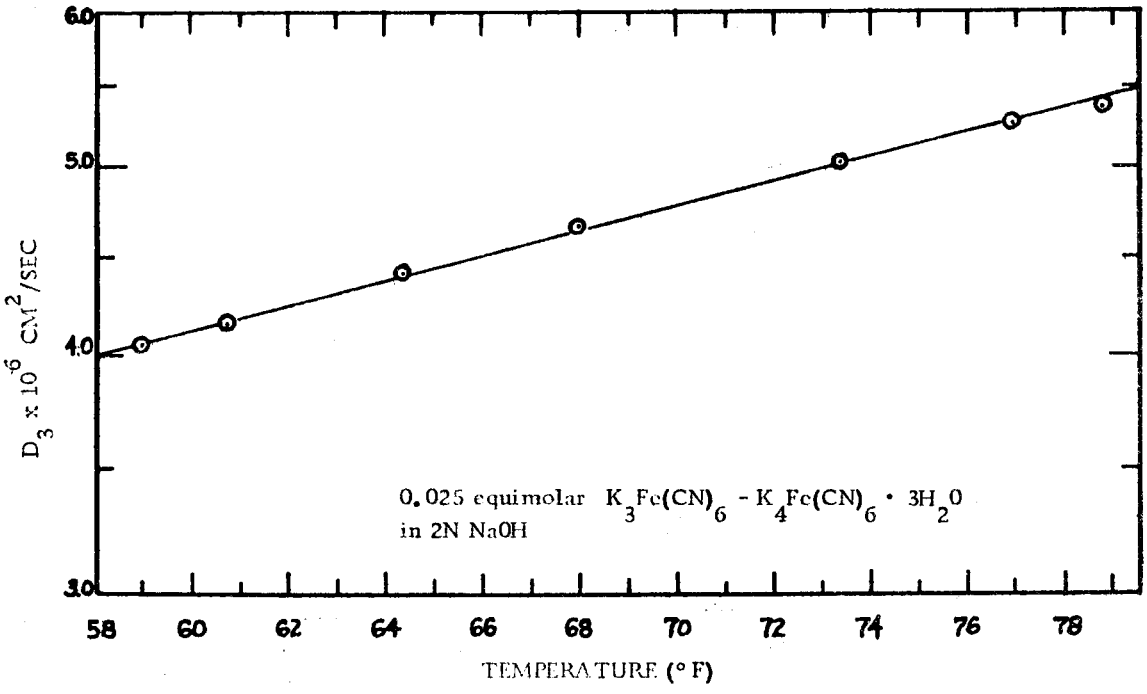

Figure (31) Diffusivity of Ferricyanide Ion

Table (III) Comparison of Physical Properties of Water and Electrolyte

	Water	Electrolyte
Specific Gravity (66.2° F)	0.9984	1.093
Viscosity c.p. (66.2° F)	1.03	1.64
Surface Tension * dynes/cm (64.4° F)	73.05	77.0 (2N NaOH)

* Liquid against air

APPENDIX C

TEMPERATURE OF THE CLIMBING FILM

TEMPERATURE OF THE CLIMBING FILM

In Figures 32-35 the film temperature is presented versus humidity with liquid flow as parameter. The liquid film temperatures for any run may be obtained by merely noting the operating variables. As one would expect, the two phase climbing film flow system involves simultaneous heat and mass transfer. Evaporation of the film accounts for the substantial decrease in the liquid temperature as it flows through the two-phase system. The following energy and mass balances on the liquid film may be used to approximately describe the film temperature results:

$$\vec{Q}_r = \vec{W}_{L_r} \Delta H_v - h_c(T_A - T_f)A_i \cong 0$$

$$\vec{W}_{L_r} = k_i(p_f - p_A)A_i/(1 - x_f)$$

As shown in a plot of film temperature versus humidity, the temperature of the film decreases as the humidity decreases. As the film flows upward, its temperature approaches the equilibrium wet bulb temperature. The wet bulb temperature is the temperature attained by a small reservoir of water in contact with a large amount of air flowing past it.

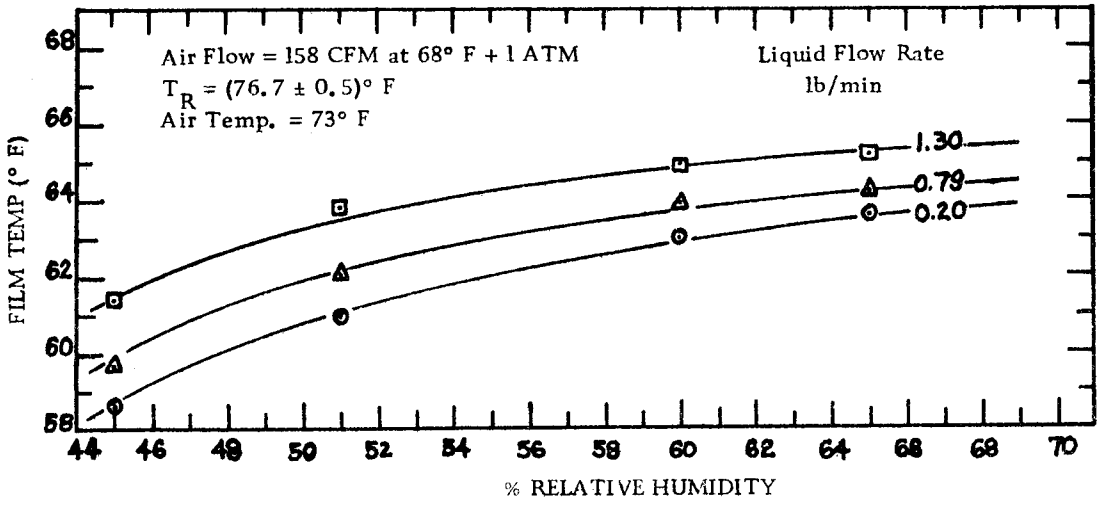

Figure (32) Temperature of Climbing Film

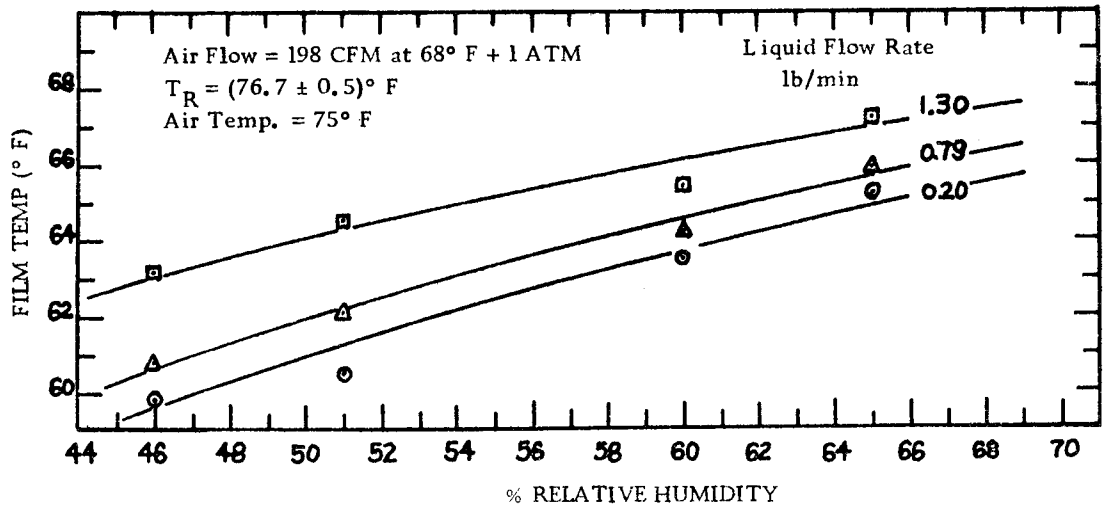

Figure (33) Temperature of Climbing Film

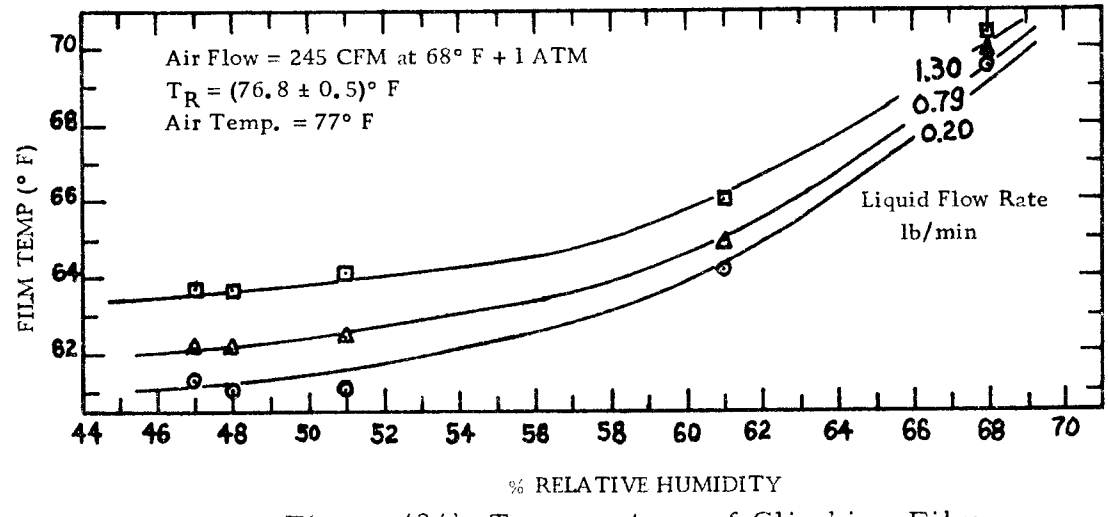

Figure (34) Temperature of Climbing Film

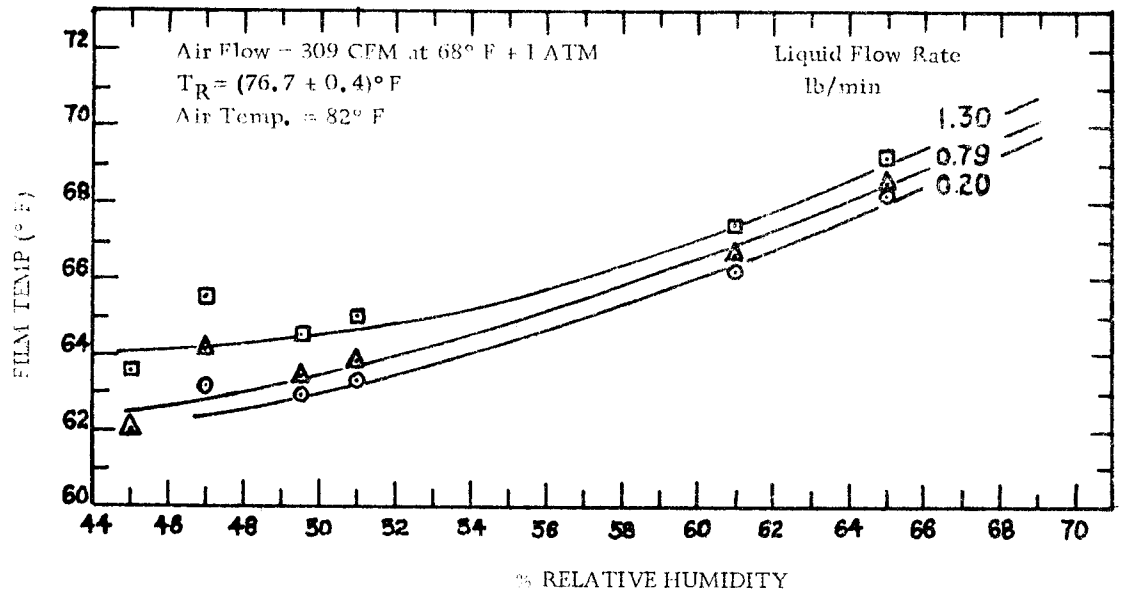

Figure (35) Temperature of Climbing Film

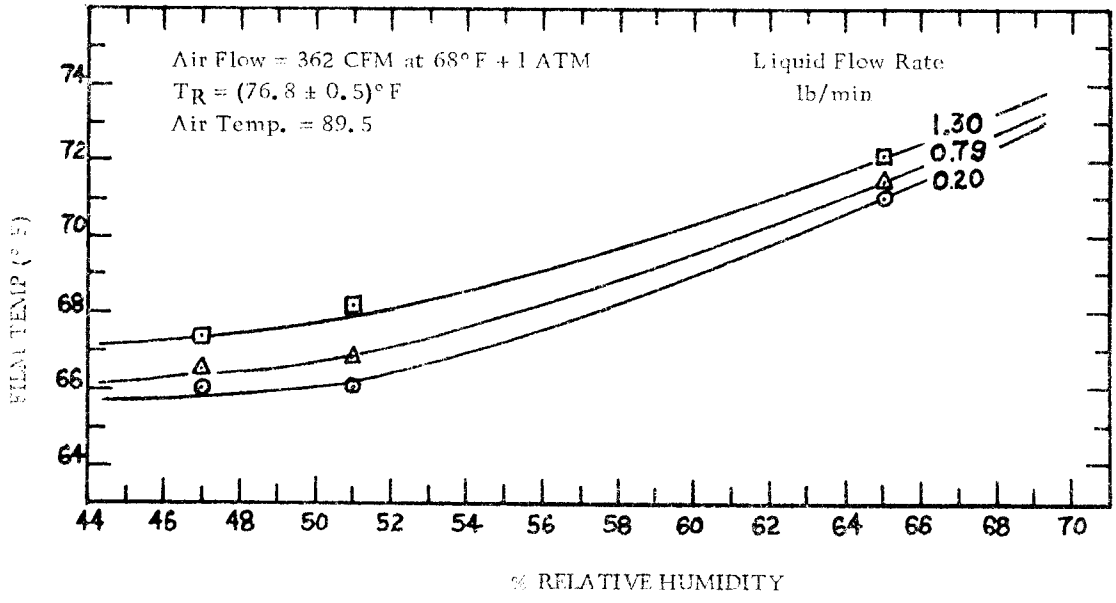

Figure (36) Temperature of Climbing Film

APPENDIX D

EFFECT OF DISSOLVED OXYGEN ON THE REDOX METHOD FOR THE MEASUREMENT OF MASS TRANSFER COEFFICIENTS

EFFECT OF DISSOLVED OXYGEN ON THE REDOX METHOD FOR THE MEASUREMENT OF MASS TRANSFER COEFFICIENTS

Introduction

An electrochemical technique utilizing a ferro-ferricyanide redox couple for measuring mass transfer coefficients has been applied in varied geometrical systems by many investigators (3, 4, 6, 20, 28, 54, 56, 62, 63, 65, 66), but the method has been restricted to oxygen-free systems. Except for a few studies (20), little has been done to determine the actual effect of presence of dissolved oxygen on the measurements, which is important in situations where the presence of air is unavoidable as in two phase (air-water) flow systems. Since the effects of air in contamination of the test solution and the test electrodes are complex, much uncertainty exists concerning the real effect of air on the measurements. Since oxygen activation polarization on most electrodes is very high, it is improbable that actual electrochemical reaction involving oxygen occurs in the voltage range required in this experimentation.

Other factors, such as mixed potentials (9) and oxide films on electrodes, are possible.

However, absorption of air by any solution and contamination

of electrodes are time-dependent. Therefore, suitable electrochemical measurements may be obtained before adverse effects become controlling. With these ideas in mind a study was designed to explore more fully the limitations of the electrochemical technique with respect to the effects of dissolved oxygen in the solution.

Theory

The electrochemical theory required to use the redox method to determine mass transfer coefficients in pipeflow is the same as that discussed in the Theory section.

Thickness of Laminar Sublayer and Concentration Boundary Layer. As turbulent flow takes place past a solid surface a thin layer of fluid adjacent to the surface is generally considered to be in laminar flow. For flow through circular tubes, this laminar sublayer is considered to extend up to $y^+ = 5$ and the velocity distribution is given as

$$u^+ = y^+ \tag{37}$$

Using the Blasius friction factor relation for circular tubes

$$f = 0.079\,(Re)^{-0.25} \tag{38}$$

the thickness δ_m of the laminar sublayer is

$$\delta_m = 25.2d(Re)^{-7/8} \tag{39}$$

Furthermore, the average concentration boundary layer thickness may be approximated by the Nernst diffusion layer equation

$$\delta_c = D_{AB} / \bar{k}_c \tag{40}$$

Thus, the ratio of δ_c to δ_m may be written

$$\delta_c/\delta_m = 0.0397 \frac{D_{AB}}{\bar{k}_c d} (Re)^{7/8} \tag{41}$$

For the length to diameter ratios and Reynolds number range covered in the preliminary study, the quantity δ_c/δ_m did not exceed 0.2. Therefore, the Leveque solution for prediction of mass transfer coefficients may be used to determine the reliability of the experimental results in turbulent pipe flow.

The Leveque Solution for Turbulent Flow in Tubes. Equation 25 is also the Leveque solution for the mass transfer coefficient in circular tubes;

$$k_{c_x} = \frac{D_{AB}}{0.893} \left(\frac{\bar{c}}{9D_{AB}x} \right)^{1/3} \tag{25}$$

where $\bar{c}$ is the value of the velocity gradient at the wall. The constant $\bar{c}$ may be determined using the Blasius friction factor relation (Equation 38), giving

$$k_{c_x} = \frac{0.183\, D_{AB}}{x} (Re)^{0.583} (Sc)^{1/3} (x/d)^{2/3} \quad (42)$$

Therefore, the average mass transfer coefficient $\bar{k}_c$ is given as

$$\bar{k}_c = \frac{0.275\, D_{AB}}{L} (Re)^{0.583} (Sc)^{1/3} (L/d)^{2/3} \quad (43)$$

where the Reynolds number (Re) is based on pipe diameter.

Similarly, it follows that

$$\bar{k}_c = \frac{0.275 D_{AB}}{L} (Re_L)^{0.583} (Sc)^{1/3} (L/d)^{0.084} \quad (44)$$

where the Reynolds number (Re_L) is based on electrode length.

Apparatus and Experimental Procedure

In the preliminary study the redox system used was 0.05 equimolar solution of potassium ferricyanide and potassium ferrocyanide in 2N NaOH. The sodium hydroxide acted as an indifferent electrolyte to eliminate any migration due to ionic transference effects. For the determination of actual mass transfer coefficients, the solutions were prepared just prior to the runs using specially

treated distilled water. Nitrogen had been bubbled through the distilled water to eliminate any dissolved oxygen. Also, a positive nitrogen pressure was maintained on the flow system, Figure 37, during the course of the experiments. Furthermore, precautions were taken to keep the test solution away from light. Potassium ferrocyanide slowly decomposes in light to form hydrogen cyanide which would poison the electrodes. However, decomposition of the ferrocyanide complex can be practically eliminated in alkaline solutions which are kept in darkness (47).

The electrolytic reaction at the cathode (working electrode) was the reduction of ferricyanide ion to ferrocyanide ion

$$Fe(CN)_6^{-3} + e^- \rightarrow Fe(CN)_6^{-4}$$

This redox couple was suitable in the present study since in alkaline solutions it was relatively stable, its reaction was rapid, and the critical flow rate (54) was not reached in these experiments. The system has been extensively studied by other investigators, and as a result physical property data are available in the literature.

The test electrodes were of two types--wire electrodes and ring electrodes. For the wire electrode, Figure 38A, the electrochemical reaction was carried out between a large stainless steel ring (anode) and the small nickel wire (cathode) mounted flush to the

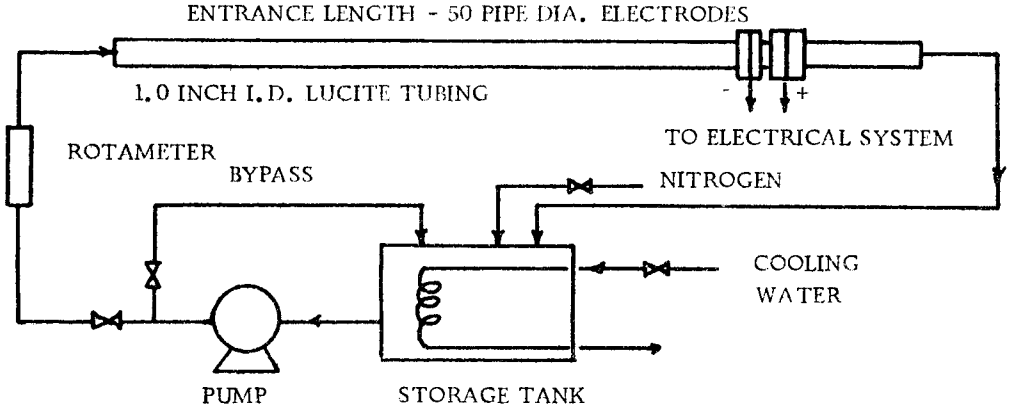

Figure (37) Pipe Flow System

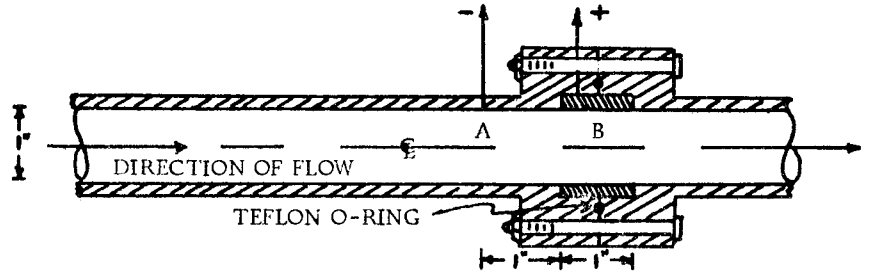

A - NICKEL WIRE ELECTRODE (CATHODE)

B - STAINLESS STEEL ELECTRODE (ANODE)

Figure (38A) Wire-Electrode Assembly for Pipe Flow Study

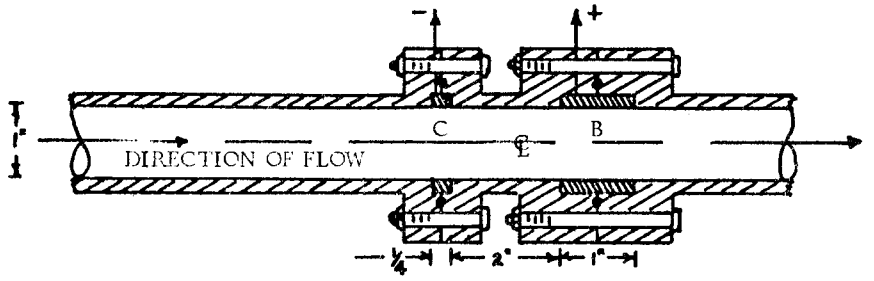

B - STAINLESS STEEL ELECTRODE (ANODE)

C - NICKEL ELECTRODE (CATHODE)

Figure (38B) Ring-Electrode Assembly for Pipe Flow Study

lucite pipe wall. The 0.064-inch diameter wire electrode was inserted into the pipe wall and held in place with epoxy cement. The wire was then made flush with the pipe wall using fine abrasive. The 1-inch long anode was large enough to not limit the electrical current in any way. Thus, all concentration polarization effects were due only to the reaction at the wire electrode, although at limiting current this is usually true (9). This simple type of electrode arrangement was used to provide information concerning the practical measurement of mass transfer rates at solid-liquid interfaces, and the possible application of the mass transfer rate fluctuation data obtainable (56, 62, 63, 65).

In the second electrode arrangement, Figure 38B, both the anode and the cathode were ring electrodes forming the pipe wall. The cathodes consisted of short sections of nickel pipe of various lengths with length to diameter ratios varying approximately from 1/8 to 1.0. Each electrode was carefully machined and polished to eliminate any roughness or discontinuities at the flanges which held the electrodes within the test section. The anode consisted of the 1-inch long stainless steel ring electrode used in the previous case. The primary purpose of the ring electrode was to measure mass transfer coefficients as a function of flow rate and L/d ratios.

The electrodes were cleaned before each run with carbon tetrachloride and buffed with rouge paper. They were also cathodically

cleaned in 5 percent NaOH solution at a current density of 20 ma. for approximately 12 minutes to ensure elimination of chemical polarization for this redox system. Following each run the cell was immediately disassembled and inspected to ascertain if adverse corrosion deposits had formed on the electrode surface during the experiment.

All experimental mass transfer data were obtained at limiting current which was determined from a plot of average current vs. potential similar to the curve in Figure 39. Limiting current is obtained at the flat portion of the curve. Under these conditions the current was controlled by the rate of mass transfer of ferricyanide ions to the surface of the working electrode at which the concentration of the ferricyanide ions were zero.

A sketch of the electrical circuit used is given in Figure 7. A potential was applied between the anode and the cathode, and the current in the circuit was measured. Adjustment of the rheostat in the circuit permitted the determination of the entire polarization curve. Some time elapsed whenever the circuit variables were changed before steady state was reached. For the wire electrode only a few seconds were required, whereas, for the largest ring electrode almost a minute was necessary.

The temperature at which all experimentations were accomplished was 25°C. It was carefully maintained since the physical

variables, and, thus, the mass transfer coefficient are all temperature dependent.

Additional experiments involved studying the effect of dissolved oxygen on the mass transfer data. The importance of such information is easily seen in the possible application of the electrochemical technique in situations where the presence of air is unavoidable such as in two-phase air-water flow systems. In these tests the same procedure as previously outlined was followed except once the nitrogen saturated data was obtained the test solution was exposed to air. Experimental measurements continued until air saturated conditions were obtained. The dissolved oxygen content was continuously observed by means of a Beckman oxygen analyzer Model 777. This procedure was followed to compare the results of the mass transfer data taken in the presence of air with those obtained for the nitrogen saturated conditions.

The oxygen analyzer is a direct readout instrument based on the polarographic principle for the analysis of gaseous and dissolved oxygen. The device was calibrated at the sample temperature to read percent saturation of dissolved oxygen in solution, 100% O_2 saturation corresponding to 160 mm of Hg partial pressure under atmospheric conditions. If the temperature is constant the accuracy of this instrument is within ±1% full scale.

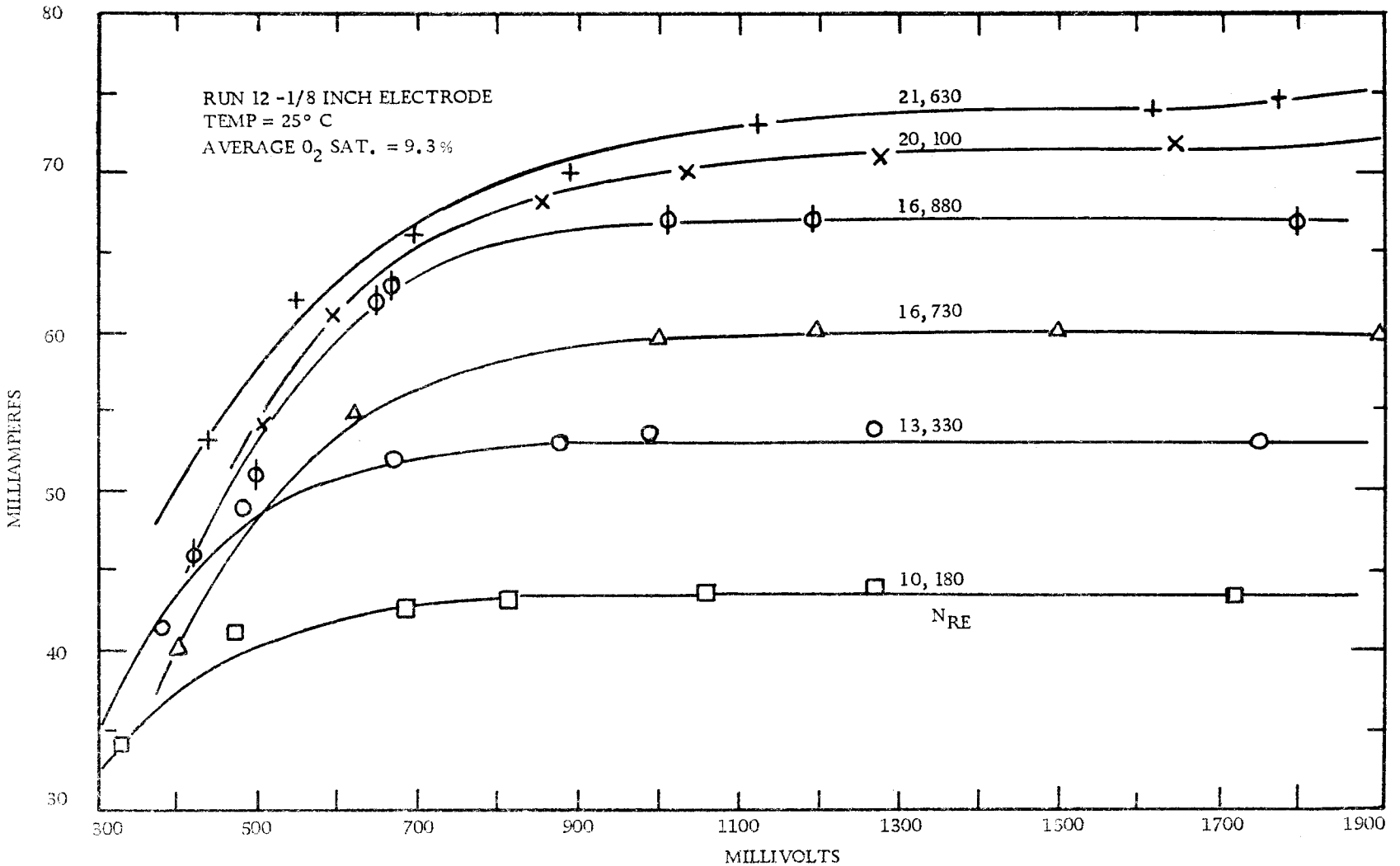

Figure (39) Curves Showing Limiting Current

Experimental Results

Wire Electrode. Figure 40 summarizes the mass transfer data as a function of tube Reynolds number for the wire electrode. All mass transfer coefficients were calculated from Equation 6 using limiting current data. Based on the accuracy of the measured quantities in Equation 6, the exactness of the method lies within ± 3%. All data approaches that of Run 7 (O_2-free) which was considered to be free from all adverse effects. These data were obtained for a cathodically cleaned electrode in a nitrogen saturated solution with positive nitrogen pressure on the system. There is good agreement with the results of Reiss and Hanratty (63). However, failure to cathodically clean the electrodes and to remove dissolved oxygen from the solution is seen by the change in the $\bar{k}_c$ versus N_{Re} curve. Under these contaminated conditions the slope of the curve is 0.95 whereas under ideal conditions it is about 0.59 in the N_{Re} range considered.

If the reaction is diffusion controlled, then the contaminated surface may affect only the current by blocking the surface available for reaction. However, chemical polarization arises from the kinetics at the electrode surface. The reactions involved proceed very rapidly with a minimum of chemical polarization on "clean" nickel electrodes (20). This fact is also demonstrated by the occurrence of a "limiting current" which indicates a "diffusion controlled

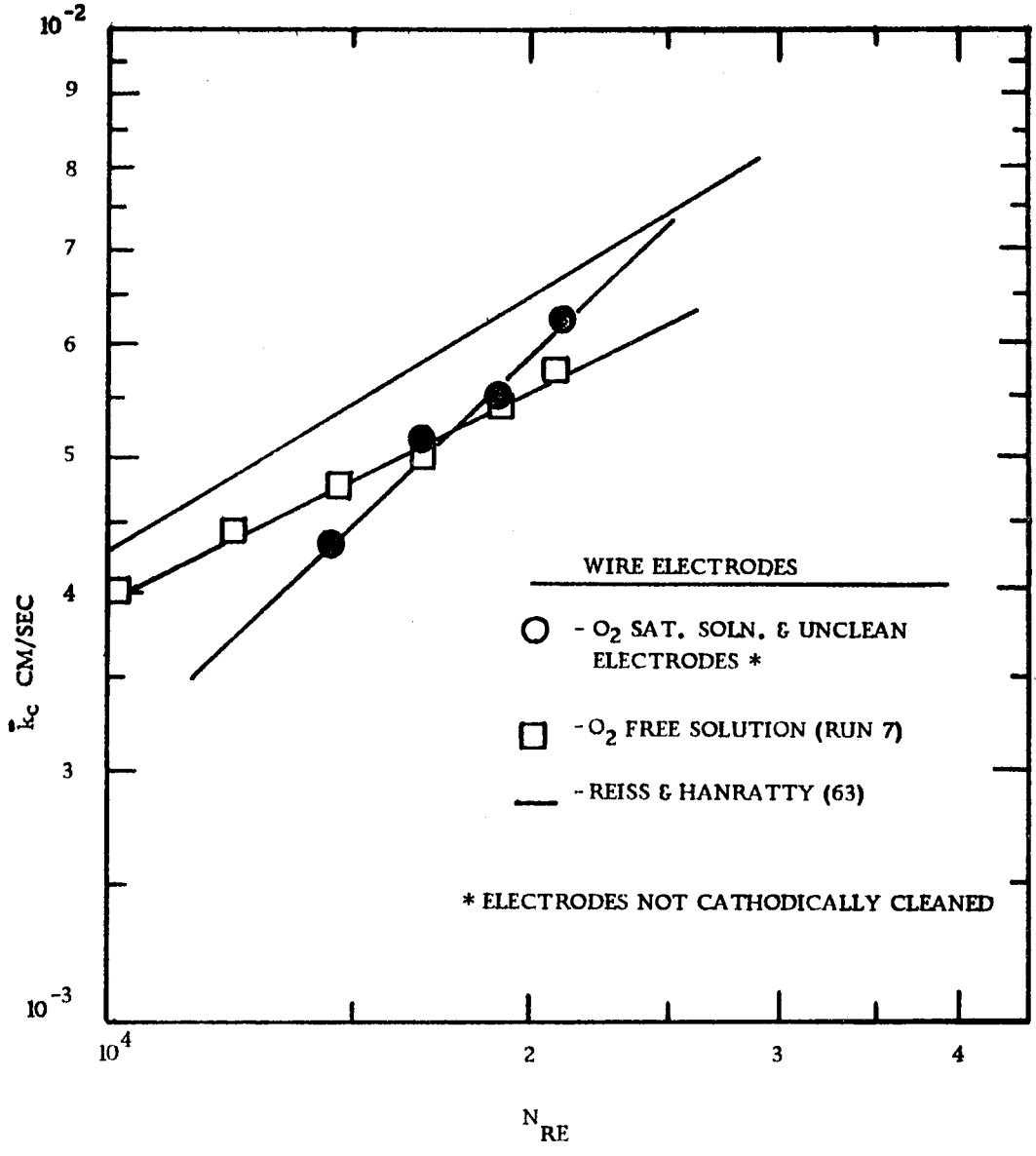

Figure (40) Effect of Dissolved Oxygen and Dirty Electrodes on Mass Transfer Coefficient

chemical reaction".

Under contaminated conditions chemical polarization is important and must be considered in the determination of the mass transfer coefficient. Under these conditions, the concentration at the wall is not zero, and Equation 6 is slightly in error. These effects are known qualitatively. The purpose of the work is to measure the extent of deviation from ideal conditions caused by contamination.

For the wire electrode all limiting current data fluctuated as previously shown by Reiss and Hanratty (62). The fluctuations increased in intensity as limiting current was approached. This seems reasonable, since any sudden transfer of material from the bulk stream would greatly affect the instantaneous rate of transfer and would become more noticeable as the wall concentration approached zero. This phenomenon is explainable if the laminar sublayer is an unsteady region which is continuously destroyed and reformed as postulated in surface renewal theories (13, 30, 42, 70).

Since edge effects predominate, the wire electrode will not give accurate measurements of the mass transfer coefficient unless it is preceded by the proper entrance length of active electrode to develop the concentration boundary layer (65). The prime importance of the isolated wire electrode is its application in studying velocity fluctuation data in the region of the so-called laminar sublayer (62).

Ring Electrodes. Results of the ring electrodes are shown in Figure 41, where $\bar{k}_c$ is plotted as a function of the tube Reynolds number. Data obtained in a typical experiment are given in Table IV. For the flow range and length to diameter ratios considered, the data of Figure 41 are in good agreement with the Leveque solution Equation 44. The average deviation from Equation 44 is ±8%. The results for the 1-inch electrode ($L/d = 1.006$) are seen in Figure 42 to be in excellent agreement with electrochemical mass transfer data of Shaw and Hanratty (66). These results also compare well with heat transfer data of Deissler (14). Figure 43 shows the data of the 1/2-inch electrode ($L/d = 0.505$) to agree well with the data of Shaw and Hanratty (66). For further comparison Sleicher's (68) heat transfer results (for $L/d = 0.4$) are included. Inspection of Figures 42 and 43 shows the heat transfer data of Faruqui and Knudsen (22) to be high. These results indicate that the electrochemical technique is in general more accurate in predicting coefficients than most heat transfer techniques. Conversion from heat to mass transfer data was fulfilled by means of the Chilton-Colburn (j-factor) analogy.

Figures 44 and 45 show the effect of air on the mass transfer measurements for the 1/8-inch and 1-inch electrodes. Because of roughness the experimental values of the 1/8-inch electrode are known to be high; however, the qualitative effect of dissolved O_2

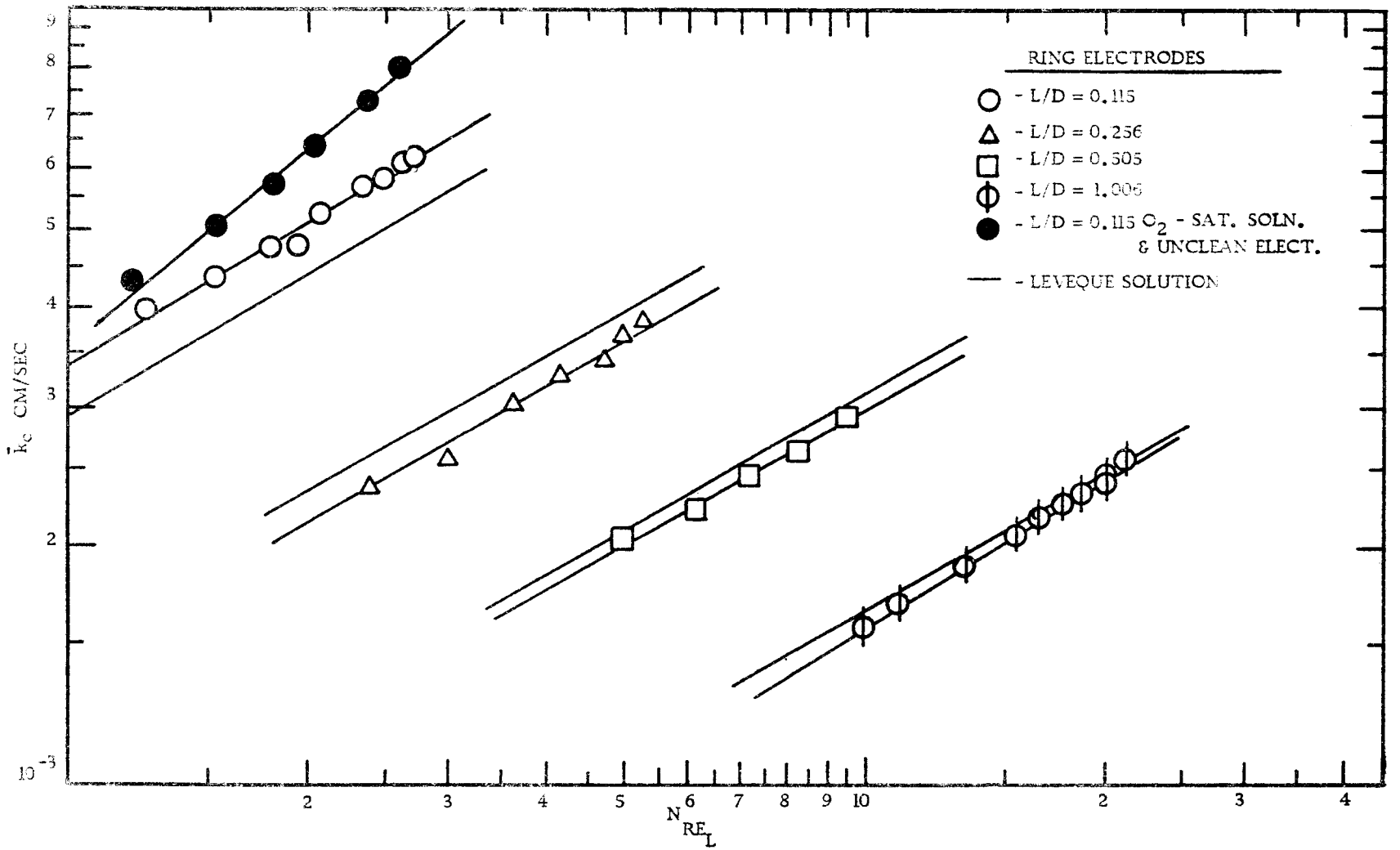

Figure (41) Mass Transfer Coefficients for Ring Electrodes

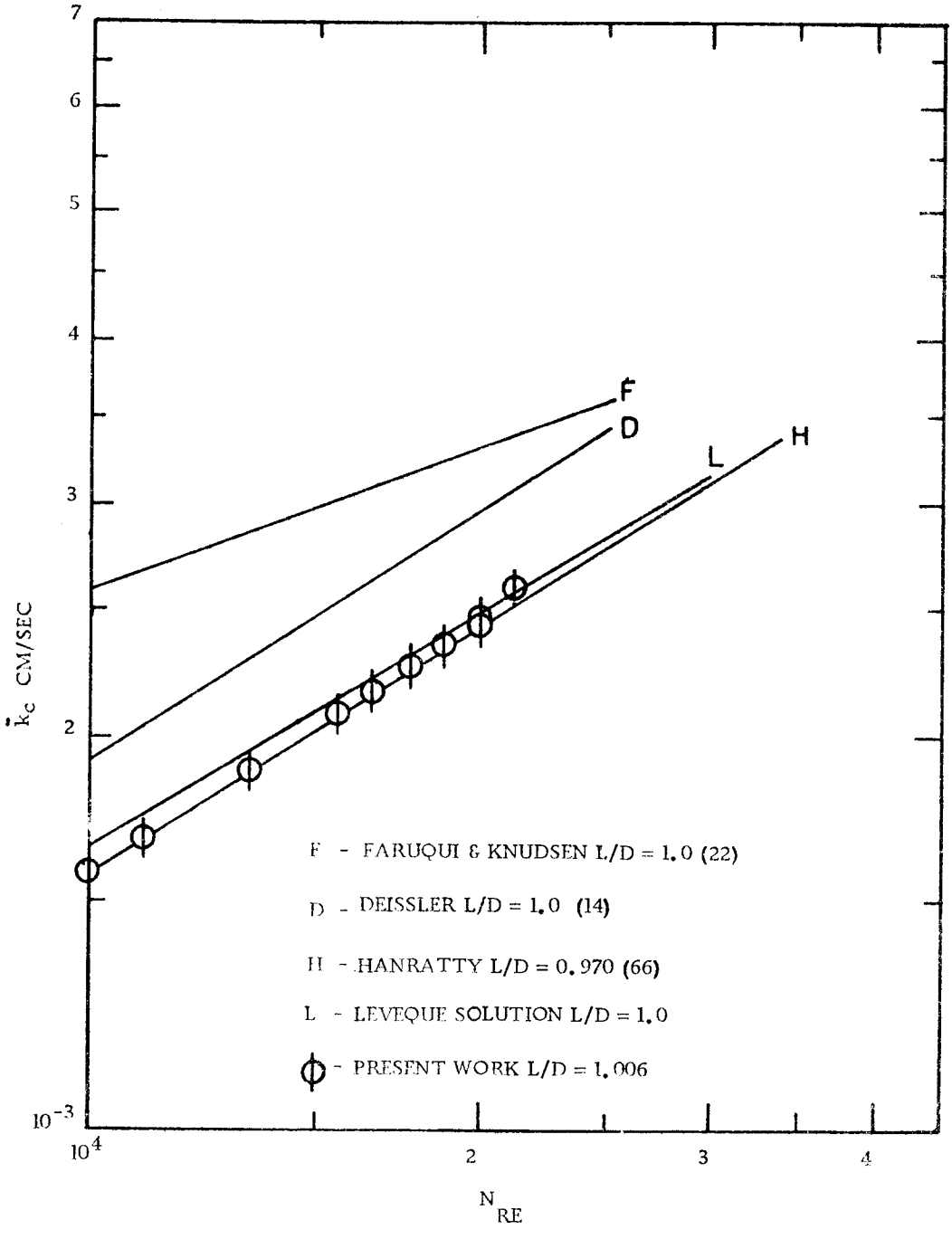

Figure (42) Comparison of 1-inch Electrode Data with Other Workers

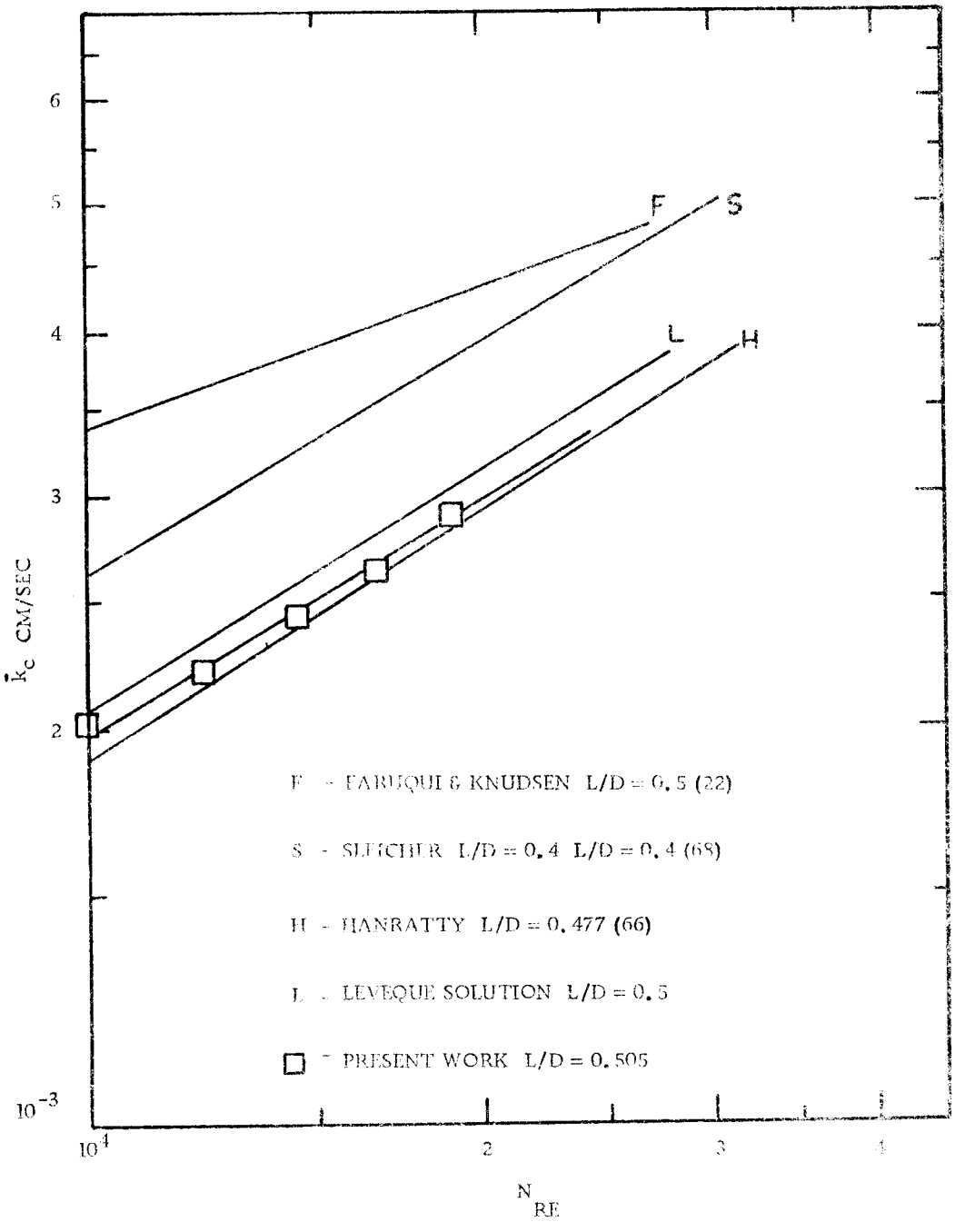

Figure (43) Comparison of 1/2-inch Electrode Data with Other Workers

on the transfer coefficient is correct and for this reason these values are included. The mass transfer coefficient is plotted versus percent O_2 saturation in solution with Reynolds number as a parameter. The time of operation of the cell is recorded for each point. The data for nitrogen saturated conditions and clean electrodes are represented by the horizontal lines, and are considered to be correct values of the mass transfer coefficients. All comparisons with the Leveque theory and with data of other investigators were made with experimental data obtained in this nitrogen saturated range. In this study mass transfer coefficients were determined using limiting current data such as that in Figure 46.

From Figures 44 and 45 it is seen that as the oxygen saturation in solution increases, the mass transfer coefficient decreases. However, the mass transfer is affected not only by the dissolved oxygen but also by the time of operation of the cell since the electrodes become less active with time of use. Data obtained with the 1/8-inch electrode below 50% O_2 saturation are within 3% of the correct coefficients for a total operating time of 170 minutes, while measurements with the 1-inch electrode below 50% O_2 saturation are within 1.6 percent of the correct coefficients for an operating time of 175 minutes. Under the present flow conditions one could apply this electrochemical technique up to 70% O_2 saturation within an operating time of 275 minutes and still obtain coefficients within

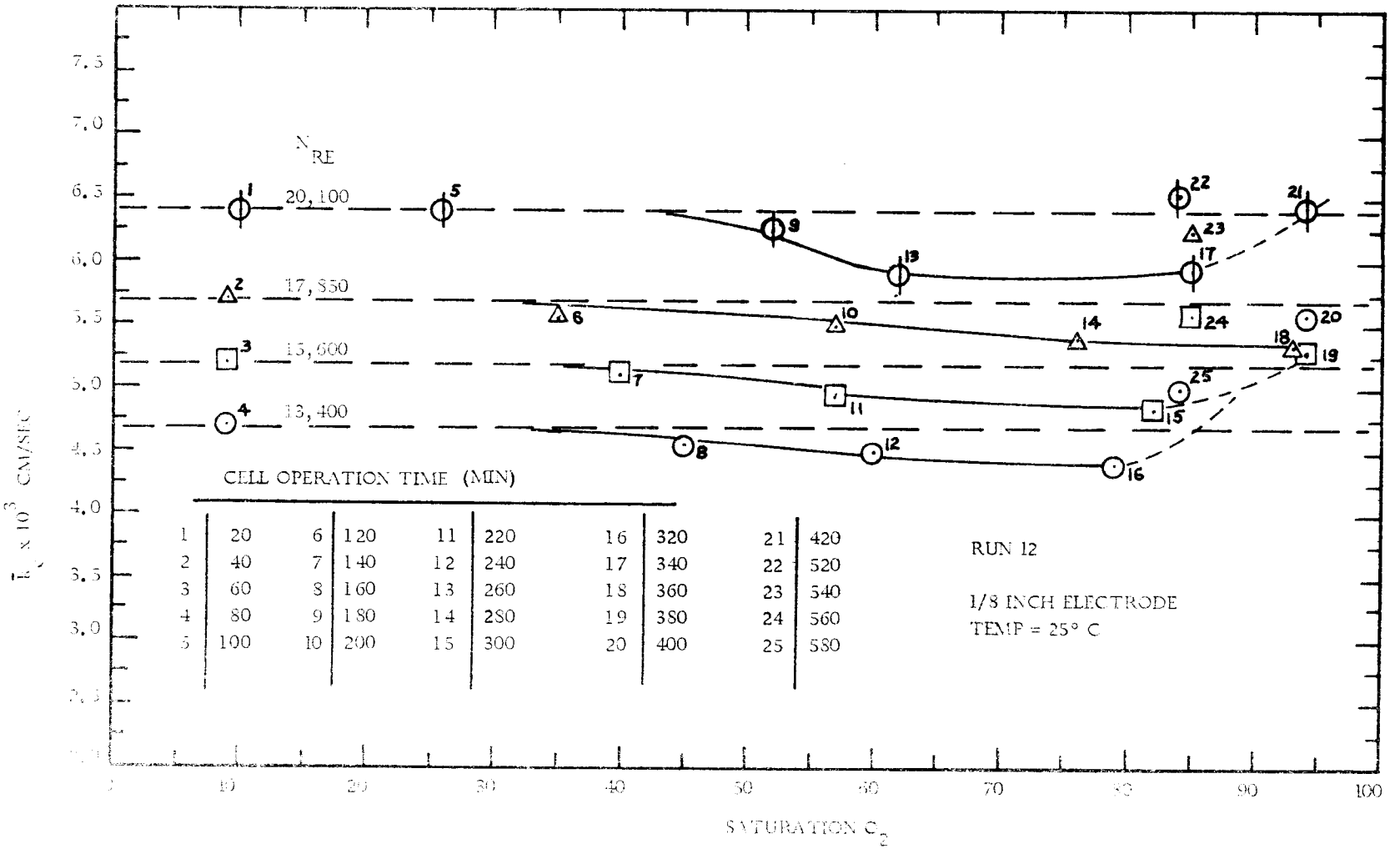

Figure (44) Effect of Dissolved Oxygen on Mass Transfer Coefficients

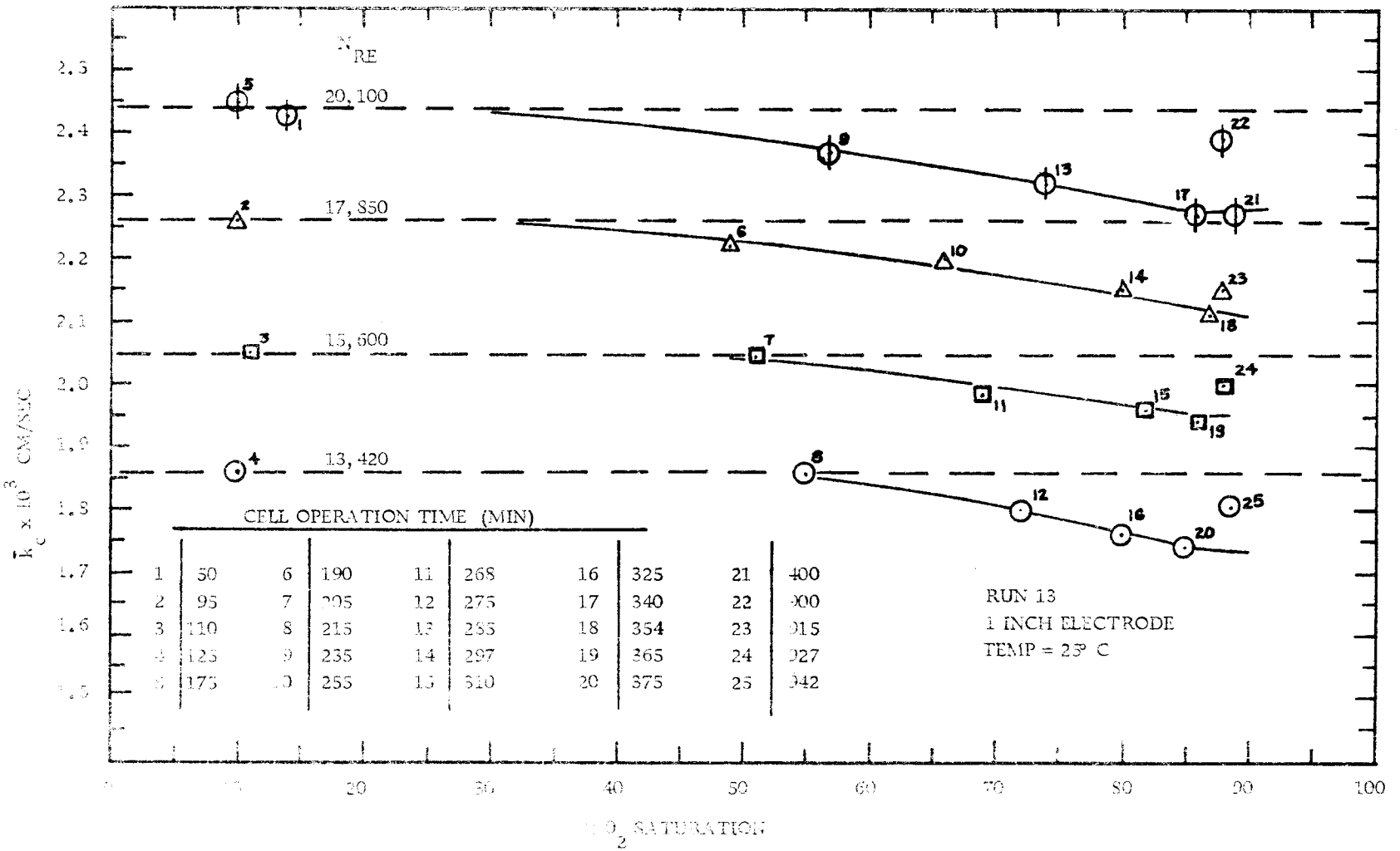

Figure (45) Effect of Dissolved Oxygen on Mass Transfer Coefficients

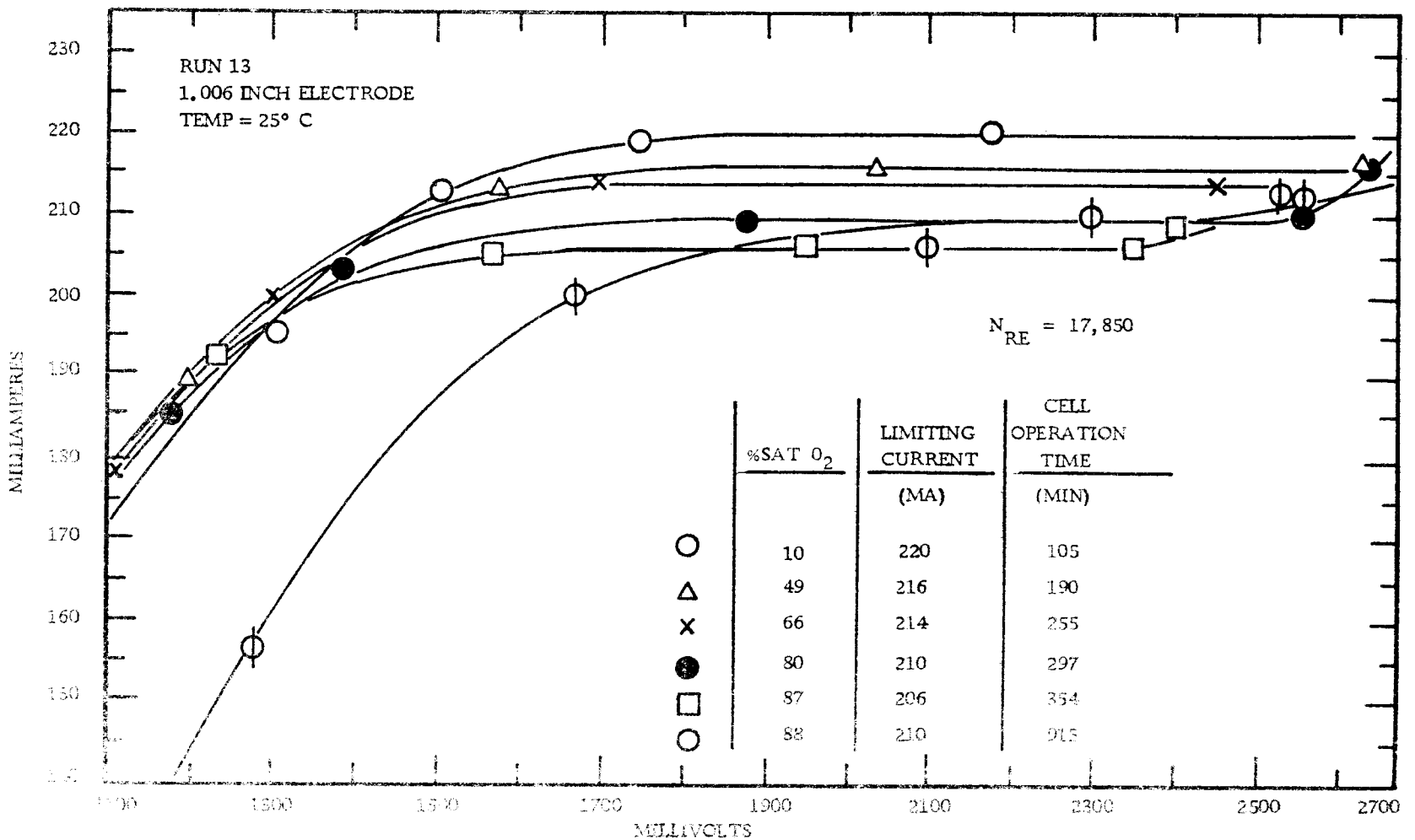

Figure (46) Effect of Dissolved Oxygen and Operating Time on Limiting Current

5% of the correct values. It appears advisable not to use this technique in the high O_2 saturation range after the cell has been operated for a considerable length of time. At these conditions the electrodes are completely contaminated, and other adverse reactions may be occurring both within solution and at the electrodes.

Data taken after a very long time of operation at the high O_2 saturation level (85%) agree well with data previously taken for saturated solutions with electrodes which were not cathodically cleaned. Under these contaminated conditions the slope of the $\bar{k}_c$ versus N_{Re} curve approached a value of 0.95 as previously observed in Figures 40 and 41. The slope of this curve served in this study as a good indicator of whether the test solution and test electrodes were contaminated.

The complex interrelation of dissolved O_2, contamination of electrodes and time of operation is not fully known. It has been the purpose of this study not necessarily to explain these phenomena but instead to explore the limits of the practical application of this method. This study has shown that with certain precautions electrochemical mass transfer measurements can be obtained in the presence of air.

Conclusions

1. The electrochemical method of obtaining mass transfer

data is very reliable if all adverse effects are eliminated. For the ferro- ferricyanide system elimination of dissolved oxygen and light, and the proper cleaning of the electrodes are the most important factors in the successful use of the technique. The adverse effect of "unclean" electrodes and air saturated solutions on the electrochemical data is reflected by a change in the slope of the $\bar{k}_c$ vs. Reynolds number plot.

2. Mass transfer to the electrodes is of a fluctuating nature as seen from experimental limiting current data of a wire electrode. This indicates the possible unsteady nature of the laminar sublayer as demonstrated by other investigators (21, 50, 62, 63, 65, 69).

3. Over the limited Reynolds number range (<22,000) and for the L/d ratios ($L/d < 1.0$) studied, the Leveque solution is within $\pm 8\%$ of the experimental data.

4. The electrochemical technique can be applied in the presence of air if certain precautions are taken. This study has shown, if the test solution is first saturated with nitrogen, future exposure to air for a short period of time does not greatly affect the mass transfer data. Under the present flow conditions one could apply the technique up to 70% O_2 saturation within an operating time of 275 minutes and still obtain coefficients within 5% of the correct values.

APPENDIX E

ESTIMATION OF THE MIGRATION CURRENT

ESTIMATION OF THE MIGRATION CURRENT

Ions may be transferred from the bulk of the solution to the surface of the working electrode by convection, diffusion and migration. The total flux of particles of the i^{th} species in a moving medium is

$$\vec{N}_i = \frac{\vec{I}}{n_i F} = \cancel{c_i v}^{0} - D_i \frac{\partial c_i}{\partial y} - \frac{D_i n_i F c_i}{RT} \frac{\partial \phi}{\partial y} \qquad (45)$$

for the case where the bulk motion term vanishes. If we consider a solution of potassium ferricyanide, pottassium ferrocyanide, and sodium hydroxide where sodium hydroxide is a supporting electrolyte, the equation of transfer takes the following form at the cathode.

For ferricyanide ion ($Fe(CN)_6^{-3}$)

$$\overleftarrow{I} = -3D_1 F \frac{\partial c_1}{\partial y} + \frac{9D_1 F^2 c_1}{RT} \frac{\partial \phi}{\partial y} \qquad (46)$$

For ferrocyanide ion ($Fe(CN)_6^{-4}$)

$$O = \frac{\partial c_2}{\partial y} - \frac{4Fc_2}{RT} \frac{\partial \phi}{\partial y} \qquad (47)$$

For hydroxide ion (OH^-)

$$O = \frac{\partial c_3}{\partial y} - \frac{Fc_3}{RT} \frac{\partial \phi}{\partial y} \qquad (48)$$

For sodium ion (Na^+)

$$O = \frac{\partial c_4}{\partial y} + \frac{Fc_4}{RT}\frac{\partial \phi}{\partial y} \tag{49}$$

For potassium ion (K^+)

$$O = \frac{\partial c_5}{\partial y} + \frac{Fc_5}{RT}\frac{\partial \phi}{\partial y} \tag{50}$$

The condition of electrical neutrality is

$$\sum_i n_i c_i = 0$$

and for the aforementioned electrolyte

$$-3c_1 - 4c_2 - c_3 + c_4 + c_5 = 0$$

The migration current density is given by

$$I_m = \frac{9D_1F^2c_1}{RT}\frac{\partial \phi}{\partial y} \tag{51}$$

Solution of Equations 46-51 gives an estimate of the migration current.

The migration current can also be estimated from Equation 4 if the transference number t_i is available. In the present study and in other investigations (54, 63) the limiting current is directly proportional to the bulk composition of ferricyanide in the range

from 0.001 to 0.1 molar. Therefore, the sodium hydroxide present as an indifferent electrolyte has a high enough concentration to eliminate electrical transference effects. The transference number for a typical electrolyte, for example, 0.01 molar potassium ferricyanide, 0.01 molar potassium ferrocyanide and 2.1 molar sodium hydroxide is 0.0018 as reported by Reiss and Hanratty (63). Consequently, ionic migration may be neglected and one can assume that the flow of current carrying ions in the solution in the presence of a foreign electrolyte is equal to the diffusional flux. In the present study the migration current was estimated to be less than 1% of the total current.

APPENDIX F

CURRENT-VOLTAGE PARAMETERS FOR ELECTROCHEMICAL MASS TRANSFER MEASUREMENTS

Table V. Current-Voltage Parameters for Electrochemical Mass Transfer Measurements.

Electrode length in.	Electrode Dia. in.	Electrolyte Concentration moles/liter	R_1 ohms	R_2 megohms	Voltage Source volts	Limiting Current milliamps	Cleaning Current milliamps	Time to Reach Steady State sec.
			Climbing Film Flow					
0.0625	0.993	0.025	20	0.5	15	6-25	25	15
0.126	0.991	"	"	"	"	10-35	50	30
wire*	0.064	"	12,000	1.0	6	0.1-0.4	0.42	10
			Single Phase (Pipe) Flow					
0.115	1.0	0.05	20	0.5	6	40-80	50	30
0.256	"	"	"	"	"	50-100	100	45
0.505	"	"	"	"	12	100-180	200	60
1.0	"	"	"	"	17	150-250	400	"
wire*	0.064	"	8,000	1.0	6	0.3-0.65	0.42	10

*Gauge no. 14 wire.

Note: the electrical circuit is described in Figure 7.

APPENDIX G

DISSOLVED OXYGEN CONTENT OF THE CLIMBING FILM

DISSOLVED OXYGEN CONTENT OF THE CLIMBING FILM

The percent saturation of dissolved oxygen of the climbing film at the position of the test electrodes in the two-phase flow system is presented in Table VI for various gas and liquid flows. The manner in which the results were obtained is presented in the Experimental Procedure. To account for the amount of oxygen absorbed by the sample solution during the measurement procedure, suitable corrections were made on the data. For the liquid and gas flow rates studied, the corrected percent saturation of dissolved oxygen varied between 30-50%.

The effect of dissolved oxygen on the mass transfer coefficient in climbing film flow may be estimated by considering Table VI in conjunction with Figures 44 and 45 in Appendix D. These figures show the effect of air on the measured mass transfer coefficient in a pipe. The mass transfer coefficients obtained for climbing film flow in the presence of air are estimated to be accurate within 2% if temperature is constant.

Table VI. Dissolved Oxygen Content of the Climbing Film.

Air Flow cfm*	Liq. Flow lb/min	T_{film} °F	D.O.$_{in}$ % sat.	D.O.$_{film}$ % sat.	Time$_{meas.}$ min.	D.O.$_{corrected}$ % sat.
157	0.48	62	10	40	4	32
"	0.79	63	10	40	4	32
164	0.27	62	10	53	5	44
173	0.20	61	14	51	5	42
"	0.48	"	15	47	5	38
"	0.79	62	20	45	4	37
"	1.10	63	11	43	4	35
223	0.48	62	10	50	5	41
"	0.97	61	10	46	4	38
244	0.79	65	10	50	5	41
309	0.48	62	13	59	6	49
"	0.79	63	14	56	6	46
"	1.10	"	10	55	5	46
362	1.10	66	10	55	5	46
"	1.30	"	10	54	6	44

*at 68°F and 1 atm.

Percent of O_2 Absorbed by Sample Solution During Measurement Procedure

D.O. initial % sat.	Time of D.O. Measurement min.	D.O. final % sat.
40	4	48
37	3	45
43	6	55
32	3	41

The manner in which the results were obtained in explained in the Experimental Procedure section.

APPENDIX H

MASS TRANSFER DATA AT THE SOLID-LIQUID FILM INTERFACE

Table VII: Mass Transfer Data at the Solid-Liquid Film Interface.

Liq. Flow lb/min	Air Flow cfm*	T_f °F	i_L m. a.	$\bar{k}_c \times 10^3$ cm/sec	Liq. Flow lb/min	Air Flow cfm*	T_f °F	i_L m. a.	$\bar{k}_c \times 10^3$ cm/sec
0.20	143	63	7.3	2.40		198	63.4	11.8	3.89
	152	63	6.8	2.24		245	62	14.7	4.84
	160	62.2	6.7	2.21		309	63.4	18.8	6.20
	172	62.6	9.0	2.97		369	69.9	23.5	7.74
	183	64	10.8	3.56	0.64	157	64	7.7	2.53
	197	64.4	11.85	3.90		172	63.8	8.25	2.72
	198	64.1	12.3	4.05		197	65	11.7	3.86
	198	63	12.0	3.95		198	63.6	11.95	3.94
	245	61.5	14.6	4.81		198	64.7	12.5	4.12
	309	67.1	19.5	6.42		245	65	15.7	5.17
	368	69.7	23.4	7.71		369	70.2	23.5	7.74
	370	68.8	23.3	7.68		370	70.4	23.2	7.64
0.27	145	63.2	8.0	2.64	0.79	154	64.2	8.3	2.74
	159	62.4	6.7	2.21		158	61.2	7.3	2.41
	172	64	8.65	2.85		172	61.6	8.5	2.80
	198	63.2	11.7	3.86		198	64	12.2	4.02
	309	66.5	19.2	6.33		309	63.8	19.2	6.33
0.34	145	63.4	8.45	2.78		370	70.3	24.1	7.94
	158	62.5	7.15	2.36		372	70.6	23.6	7.76
	172	62.9	8.46	2.79	1.10	158	64.4	7.9	2.60
	198	63.3	11.7	3.86		172	62.4	8.9	2.93
	245	61.8	14.4	4.74		198	65	12.9	4.25
	309	63.3	18.3	6.03		245	63.6	16.0	5.27
	309	66.4	19.3	6.36		309	64.6	19.7	6.49
	369	69.8	23.4	7.71		370	70.9	24.3	8.01
	370	68.9	23.0	7.58	1.3	158	64.6	8.3	2.74
0.41	152	63.1	7.95	2.62		172	63	9.5	3.13
	159	63	6.9	2.27		245	64	16.6	5.47
	172	63.8	8.4	2.77		309	67.7	19.2	6.33
	172	62.8	8.5	2.80		372	71.2	24.4	8.04
	197	64.7	11.7	3.86	1.46	158	63	8.4	2.77
	246	64.7	15.4	5.07		172	65	9.9	3.26
0.48	147	63	8.6	2.83		245	66.5	16.8	5.54
	157	62.6	7.4	2.44		309	68.8	21.2	6.99
	172	63	8.7	2.87		309	65.4	20.1	6.62
	172	63.6	8.0	2.64		372	71.6	24.6	8.11

Electrode Dimensions: L = 0.0625 inch, O.D. = 0.993 inch.

c_b = 0.025 moles/liter.

* at 68°F and 1 atm.

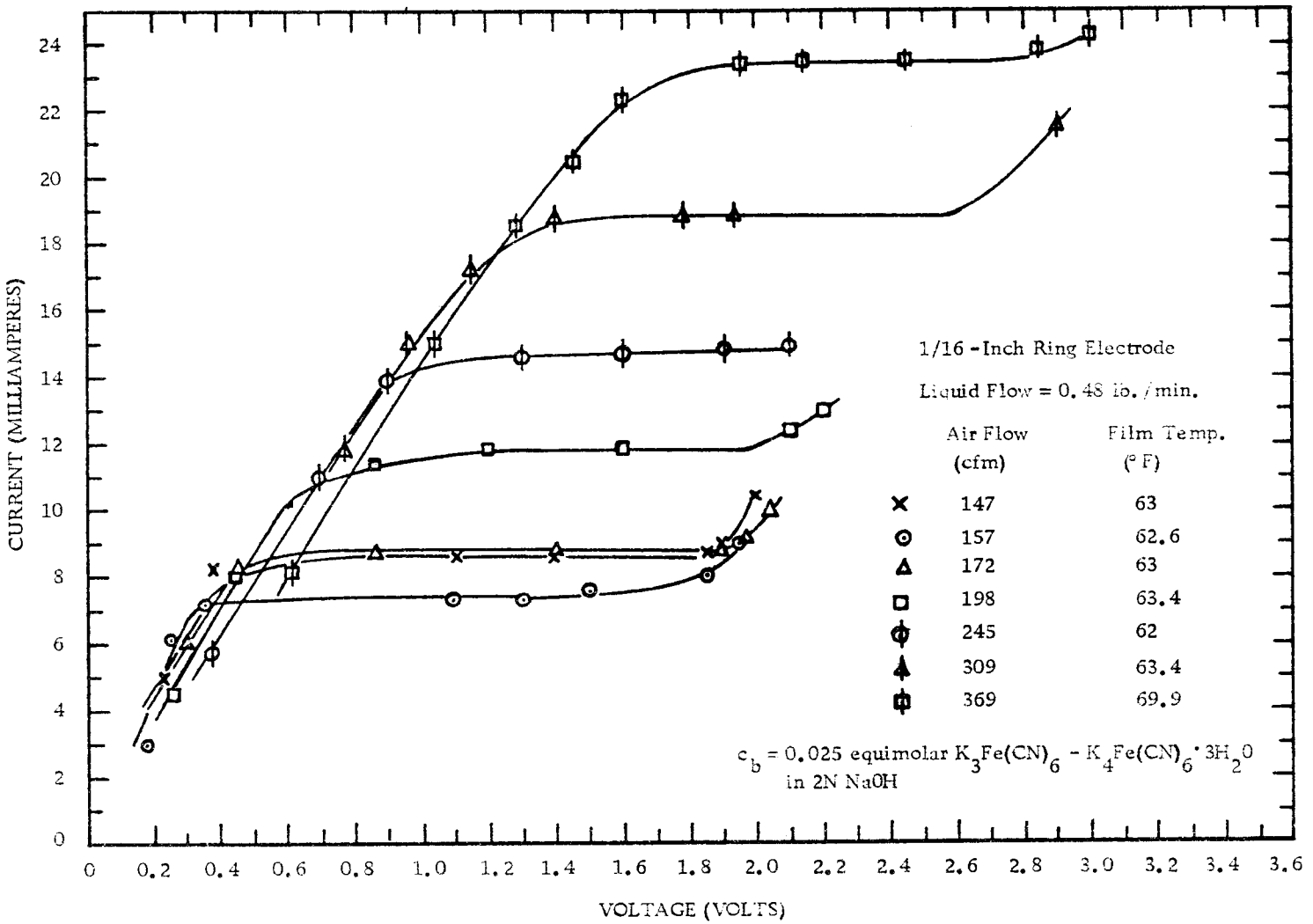

Figure (47) Limiting Current Curves in Climbing Film Flow

APPENDIX I

PRESSURE GRADIENTS IN CLIMBING FILM FLOW

Table VIII. Experimental Pressure Gradients in Climbing Film Flow.

Liquid Flow = 0.20			Liquid Flow = 0.48			Liquid Flow = 1.10			Liquid Flow = 1.46	
Air Flow	ΔP/ ΔX		Air Flow	ΔP/ ΔX		Air Flow	ΔP/ ΔX		Air Flow	ΔP/ ΔX
		*			*			*		*
163	1.55	1.50	154		1.70	154	2.41	2.00		
172		1.58	158	1.80	1.71	158	2.30	1.98	158	2.07
198		1.78	172	1.85	1.77	172	2.17	1.96	172	2.03
245	2.16	2.18	198	1.99	1.94	198	2.21	2.08	198	2.03
309		2.84	245	2.37	2.35	245	2.59	2.53	245	2.26
371		3.49	309	3.02	3.03	309	3.24	3.22	309	2.71
400		3.79	371	3.75	3.74	371	3.97	3.92	371	3.39
			400	4.12	4.09	400	4.38	4.26		4.06

Liquid Flow = 0.34			Liquid Flow = 0.79			Liquid Flow = 1.30		
Air Flow	ΔP/ ΔX		Air Flow	ΔP/ ΔX		Air Flow	ΔP/ ΔX	
152	1.72	*	141	2.14	*			*
154	1.67	1.59	154	2.00	1.83	154		2.04
158	1.64	1.60	158	1.99	1.83	158	2.39	2.00
172	1.66	1.63	172	2.00	1.84	172	2.20	1.97
198	1.84	1.82	198	2.07	2.01	198	2.28	2.15
245	2.22	2.25	245	2.43	2.44	245	2.66	2.59
309	2.84	2.92	309	3.10	3.13	309	3.31	3.28
371	3.53	3.59	371	3.85	3.82	371	4.03	3.97
			400	4.23	4.17	400	4.39	4.31

Units: Liquid Flow (lb/min). Air Flow (cfm at 68°F and 1 atm), ΔP/ ΔX (lb_f/ft^3).

* - Minimum Entrainment Conditions

APPENDIX J

WALL SHEAR STRESSES FOR CLIMBING FILM FLOW IN AN ANNULAR DUCT

WALL SHEAR STRESSES FOR CLIMBING FILM FLOW IN AN ANNULAR DUCT

Shear Stress at the Outer Wall

The shear stress at the outer (dry) wall was measured by Kim (45) by means of a Preston (60) tube. These measurements were obtained at two locations in the annular duct. The present mass transfer measurements were obtained at a position about 52 inches above the bottom location and 32 inches below the top location. Therefore, shear stresses at the outer wall for the present work were obtained by interpolation of the values at the two locations. The values used in this study are presented in Table IX.

Table IX. Experimental Shear Stresses for Climbing Film Flow in an Annular Duct.

Liq. Flow (lb/min)	Air Flow (cfm) 156	158	172	172	198	245	309	371	400
		[1] Shear Stress at the Inner Wall: $\tau_1 \times 10^2$ (lb_f/ft^2)							
0.20	0	0.10	1.30*	1.55	3.59	7.01	13.2	20.6	24.3
0.34		0	1.12*	1.22	3.22	6.67	13.1	19.9	
0.48		0	1.10*	1.19	3.20	6.83	12.5	19.5	23.7
0.79			1.28*	1.33	3.70	7.80	13.4	20.3	25.0
1.10			1.25*	1.52	4.07	8.50	14.9	21.4	25.5
1.30			1.20*	1.75	4.22	8.80	15.0	21.8	
1.46			1.10*	1.98	4.30	8.95	15.4	22.0	26.0

Liq. Flow (lb/min)	Air Flow (cfm) 198	210	220	245	288	318	350	385	402
		[2] Shear Stress at the Inner Wall: $\tau_1 \times 10^2$ (lb_f/ft^2)							
0.48	-1.26	1.64	2.81	4.93	7.88	9.52	11.6	14.3	15.4
0.79				4.67	8.35	10.6	13.3	16.3	17.7

Liq. Flow (lb/min)	Air Flow (cfm) 198	210	220	245	288	318	350	385	402
		[3] Shear Stress at the Outer Wall: $\tau_2 \times 10^2$ (lb_f/ft^2)							
0.48	4.38	4.81	5.21	6.19	8.23	9.48	11.2	13.1	14.0
0.79				6.41	8.35	9.79	11.4	13.4	14.4

*Extrapolated values: Refer to Figure 21 in the Results Section.

1 Calculated from Equation 29.

2 Calculated from Equation 19 and 20.

3 Calculated from Preston tube measurements of Kim (45).

APPENDIX K

CLIMBING FILM CHARACTERISTICS AND RADII OF MAXIMUM AIR VELOCITY

CLIMBING FILM CHARACTERISTICS AND RADII OF MAXIMUM AIR VELOCITY

Film Characteristics

Film thicknesses and wave amplitudes of the climbing film as measured by Kim (45) are shown in Table X. These data were determined by a photographic technique which is described by Kim. The method employed was to focus in the plane normal both to the inner core and to two hypodermic needles which were inserted through the outer core wall as a reference scale. Light from a stroboscope was arranged to come from behind the inner core. The resultant image was a sharp outline of the air-water interface or the inner tube wall interface. An analysis of this procedure indicates the possibility of a maximum error of ±0.002 inches which indicates a maximum percent error up to 100% for some of the film thicknesses shown especially in the high air flow rate regions.

The reported wave amplitude values may also be questionable since the shapes of waves as shown by photographs were too irregular to determine precisely the amplitude and length of waves.

It should be noted that the photographic technique may cause errors if waves are in focus either in front or behind the plane normal both to the inner core and the reference hypodermic needles. In this case the measured average film thicknesses would be greater

than the true values, and wave amplitudes and wave lengths would also be in error. As recommended by Kim some other method such as fluorescence or conductance (34, 41) should be used for further study of film thickness especially at high air flow rates. With these limitations in mind, the reported film characteristics were used in this study for lack of other data.

Radii of Maximum Air Velocity

Radii of maximum air velocity in the climbing film system were obtained by Kim (45). Air velocity profiles were measured at two locations in the annular duct. The present mass transfer measurements were obtained at a position approximately 52 inches above the bottom location and 32 inches below the top location. Therefore, radii of maximum air velocity for the present work were obtained by interpolation of the values at the two locations. The values used in this study are presented in Table X.

Table X. Film Thickness and Point of Maximum Velocity Data of Kirp (45).

Liq. Flow Rate lb/min	Air Flow Rate cmf*	h_0 Film Thickness in.	Wave Amplitude in.	r_i $(r_1 + h_0)$ in.	d_m in.	r_m $(r_i + d)$ in.	R_1 $\left(\frac{r_m^2 - r_i^2}{r_2^2 - r_1^2}\right)$	R_2 $\left(\frac{r_2^2 - r_m^2}{r_2^2 - r_1^2}\right)$
0.48	198	0.0127	0.012	0.5092	0.460	0.9565	0.3274	0.6664
	210	0.0087	0.0087	0.5052	0.452	0.9485	0.3214	0.6736
	220	0.0072	0.0072	0.5037	0.448	0.9445	0.3187	0.6772
	245	0.0052	0.0052	0.5017	0.434	0.9305	0.3065	0.6909
	288	0.0041	0.0040	0.5006	0.428	0.9245	0.3015	0.6959
	318	0.0037	0.0037	0.5002	0.423	0.9195	0.2972	0.7009
	350	0.0033	0.0031	0.4998	0.422	0.9185	0.2964	0.7017
	385	0.0031	"	0.4996	"	"	0.2965	"
	402	0.0029	0.0029	0.4994	"	"	0.2966	"
0.79	245	0.0082	0.0082	0.5047	0.464	0.9605	0.3334	0.6621
	288	0.0055	0.0055	0.5020	0.451	0.9475	0.3224	0.6743
	318	0.0045	0.0042	0.5010	0.446	0.9425	0.3181	0.6794
	350	0.0038	0.0037	0.5003	"	"	0.3185	"
	385	0.0032	0.0031	0.4997	0.445	0.9415	0.3188	"
	402	0.0030	0.0030	0.4995	"	"	"	"

* at 68°F and 1 atm.

d_m = distance from inner core wall to point of maximum air velocity.

r_1 = 0.4965 in., r_2 = 3.00 in.

NOMENCLATURE

Symbol	Definition	Dimensions
a	activity	dimensionless
a	anode (used as subscript)	
A	surface area of working electrode	cm^2
A_i	surface area of air-liquid interface	ft^2
c_b , c_3^b	bulk concentration of ferricyanide ions	moles/cc
c_i	concentration of species i; c_1 (ferricyanide), c_2 (ferrocyande) and c_3 (sodium hydroxide)	moles/cc
c_w	interfacial (solid-liquid) concentration	moles/cc
$\bar{c}$	velocity gradient at the electrode wall	1/sec
c	cathode (used as subscript)	
d	inside pipe diameter	inch
D, D_{AB}	diffusivity of ferricyanide ions	cm^2/sec
E	potential	volts
f	friction factor	dimensionless
F	Faraday (96,500)	$\frac{\text{coulomb}}{\text{equivalent}}$
g	acceleration of gravity	ft/sec^2
g_c	force-mass conversion factor (32.17)	$\frac{lb_m\ ft}{lb_f\ sec^2}$

Symbol	Definition	Dimensions
h_c	heat transfer coefficient at the air-liquid interface	Btu/hr ft^2 ^oF
h_o	average film thickness	inch
$h_o\phi$	deviation of the film from average thickness	inch
h	instantaneous film thickness	inch
ΔH_v	heat of vaporization	Btu/lb_m
i	current	amperes
i_L	limiting current	amperes
i_m	migration current	amperes
I	current density	$amperes/cm^2$
k_{c_x}	local mass transfer coefficient	cm/sec
$\bar{k}_c$	average mass transfer coefficient	cm/sec
k_i	mass transfer coefficient at air-liquid interface	$lb_m/hr\ lb_f$
L	length of electrode	inch
n	number of electrons involved in electrode reaction	
$\vec{N}$	flux of ferricyanide ions to the working electrode surface	$moles/sec\text{-}cm^2$
N_{Re}	Reynolds number ($d\rho U/\mu$)	dimensionless
N_{Re_L}	Reynolds number ($L\rho U/\mu$)	dimensionless

Symbol	Definition	Dimensions
N_{Sc}	Schmidt number $(\mu/\rho D_{AB})$	dimensionless
p	vapor pressure	lb_f/ft^2
P	pressure	lb_f/ft^2
$\Delta P/\Delta X$	pressure gradient	lb_f/ft^3
$\vec{Q}_r$	rate of heat transfer in r direction	Btu/hr
r	direction co-ordinate	inch
r_1	inner core radius	inch
r_2	outer tube radius	inch
r_i	interface (liquid film-air) radius	inch
r_m	radius of maximum air velocity	inch
R	gas constant (8.3147)	joules/mole-^oK
R	resistance	ohms
R_1	$(r_m^2 - r_i^2)/(r_2^2 - r_1^2)$	dimensionless
R_2	$(r_2^2 - r_m^2)/(r_2^2 - r_1^2)$	dimensionless
R_L	$(r_i^2 - r_1^2)/(r_2^2 - r_1^2)$	dimensionless
R_G	$(r_2^2 - r_i^2)/(r_2^2 - r_1^2)$	dimensionless
t_i	transference number of reacting species	dimensionless

Symbol	Definition	Dimensions
T	temperature	^{o}F, ^{o}C
T_A	air temperature	^{o}F
T_R	liquid temperature in the liquid reservoir	^{o}F
u	local velocity in the x direction	ft/sec
u_o	velocity at average stream cross section h_o	ft/sec
$\bar{u}$	average film velocity	ft/sec
u^+	dimensionless velocity = u/u^*	dimensionless
u^*	friction velocity = $U\sqrt{f/2}$	ft/sec
U	average velocity in pipe	ft/sec
v	local velocity in r (or y) direction	ft/sec
$\bar{W}_{L_r}$	rate of mass transfer of liquid phase in r direction	lb_m/hr
x, y	distance co-ordinate	inch
X	Lockhart and Martinelli parameter	dimensionless
y^+	dimensionless distance = yu^*/v	dimensionless
α	$(\Delta P/\Delta x + \rho_L g/g_c)$	lb_f/ft^3
β	$(\Delta P/\Delta x + \rho_L g/g_c$	lb_f/ft^3
γ	activity coefficient	dimensionless
δ_c	concentration boundary layer thickness	inch

Symbol	Definition	Dimensions
δ_m	laminar sublayer thickness	inch
η	concentration polarization	volts
$\bar{\eta}$	chemical (activation) polarization	volts
μ	viscosity	$lb_m/ft\text{-}sec$
ν	kinematic viscosity	ft^2/sec
ρ_L	density of liquid (electrolyte)	lb_m/ft^3
ρ_G	density of gas (air)	lb_m/ft^3
$\bar{\rho}_G$	density of gas core $= \rho_G\chi + (1 - \chi)\rho_L$	lb_m/ft^3
τ	shear stress	lb_f/ft^2
τ_1	shear stress at solid-liquid film interface (at inner core wall)	lb_f/ft^2
τ_2	shear stress at outer tube wall	lb_f/ft^2
τ_i	interfacial (air-liquid film) shear stress	lb_f/ft^2
ϕ	potential	volts
Φ	Lockhart and Martinelli parameter	dimensionless
χ	quality (weight fraction) of the gas phase	dimensionless